General Disclaimer

One or more of the Following Statements may affect this Document

- This document has been reproduced from the best copy furnished by the organizational source. It is being released in the interest of making available as much information as possible.

- This document may contain data, which exceeds the sheet parameters. It was furnished in this condition by the organizational source and is the best copy available.

- This document may contain tone-on-tone or color graphs, charts and/or pictures, which have been reproduced in black and white.

- This document is paginated as submitted by the original source.

- Portions of this document are not fully legible due to the historical nature of some of the material. However, it is the best reproduction available from the original submission.

Produced by the NASA Center for Aerospace Information (CASI)

NASA CR-132693

NUMERICAL SIMULATION OF TURBULENT JET NOISE - PART I

by Ralph W. Metcalfe and Steven A. Orszag

(NASA-CR-132693) NUMERICAL SIMULATION OF TURBULENT JET NOISE, PART 1 (Flow Research, Inc., Kent, Wash.) 75 p HC $4.25 CSCL 20A

N75-28069

Unclas

G3/07 31082

AUG 1975
RECEIVED
NASA STI FACILITY
INPUT BRANCH

Prepared under Contract No. NAS1-12870 by
FLOW RESEARCH, INC.
1819 S. Central Avenue, Kent, WA 98031
1 Broadway, Cambridge, MA 02142
5959 W. Century Boulevard, Los Angeles, CA 90045

for

NATIONAL AERONAUTICS AND SPACE ADMINISTRATION

1. Report No.	2. Government Accession No.	3. Recipient's Catalog No.
NASA CR-132693		

4. Title and Subtitle
"Numerical Simulation of Turbulent Jet Noise - Part I"

5. Report Date

6. Performing Organization Code

7. Author(s)
Ralph W. Metcalfe and Steven A. Orszag

8. Performing Organization Report No.
Flow Research Report No. 53

10. Work Unit No.

9. Performing Organization Name and Address
Flow Research, Inc.
1819 So. Central Ave., Suite 72
Kent, Washington 98031

11. Contract or Grant No.
NAS1-12870

13. Type of Report and Period Covered
Contractor Report

12. Sponsoring Agency Name and Address
National Aeronautics & Space Administration
Washington, DC 20546

14. Sponsoring Agency Code

15. Supplementary Notes

16. Abstract

This report describes the numerical simulation of a low-Mach number turbulent jet using spectral methods with $(32)^3 = 32,768$ Fourier modes. The purpose is to gain insight into the generation of aerodynamic noise by an examination of certain detailed flow characteristics, such as quadrupole moments, which cannot yet be measured in the laboratory. The mean flow quantities are set in accordance with the experimental data of Liu & Maestrello (1974) and the incompressible Navier-Stokes equations are then solved numerically. Due to computer speed and memory constraints, isolated downstream sections of the jet are modelled separately with the mean flow characteristics held constant in time. The flows are allowed to evolve until the fluctuating velocity components reach a statistically steady state. Cross section contour plots of the velocity components and the quadrupole moments at three different downstream positions are presented.

17. Key Words (Suggested by Author(s))
jet noise
numerical simulation
quadrupole moments

18. Distribution Statement
Unclassified - Unlimited

19. Security Classif. (of this report)	20. Security Classif. (of this page)	21. No. of Pages	22. Price*
Unclassified			

*For sale by the National Technical Information Service, Springfield, Virginia 22151

Contents

	Summary	1
1	Introduction	2
2	Flow Model	3
3	Numerical Methods	6
4	Description of the Simulations	9
5	Discussion	13
	References	14

NUMERICAL SIMULATION OF TURBULENT JET NOISE - PART 1

By

Ralph W. Metcalfe and Steven A. Orszag

Flow Research, Inc.
Kent, Washington

Summary

This report describes the numerical simulation of a low-Mach number turbulent jet using spectral methods with $(32)^3 = 32,768$ Fourier modes. The purpose is to gain insight into the generation of aerodynamic noise by an examination of certain detailed flow characteristics, such as quadrupole moments, which cannot yet be measured in the laboratory. The mean flow quantities are set in accordance with the experimental data of Liu & Maestrello[1] and the incompressible Navier-Stokes equations are then solved numerically. Due to computer speed and memory constraints, isolated downstream sections of the jet are modelled separately with the mean flow characteristics held constant in time. The flows are allowed to evolve until the fluctuating velocity components reach a statistically steady state. Cross section contour plots of the velocity components and the quadrupole moments at three different downstream positions are presented.

1. Introduction

Noise production by aerodynamic jets is a basic fluid mechanical problem with important practical consequences in the design of aircraft engines. In this report, numerical simulations of an idealized jet flow are discussed with the the goal of obtaining better understanding of the mechanism of noise production.

Laboratory experiments, such as those reported by Liu & Maestrello[1], can provide relatively complete information on simple flow quantities, like the mean velocity field, but are not yet capable of resolving the quadrupole moments of the flow which govern noise production. On the other hand, numerical simulation permits detailed examination of the flow at any point in time, and the calculation of arbitrary flow parameters, including quadrupole moments, at all space points. However, numerical simulations also have their drawbacks, especially limited resolution which restricts the Reynolds number of the flows that can be accurately simulated. It is preferable to view laboratory and computer experiments as complementary, not mutually exclusive; in the present work, laboratory data are used to fix certain gross features of the jet flow, which are then examined in more detail by numerical simulation.

In Sec. 2, the flow model and the equations of motion are discussed. In Sec. 3, the numerical method is presented, while in Sec. 4 the numerical simulations performed to date are reviewed. Finally, in Sec. 5, a discussion is given of how the present results will be used in the study of noise production.

2. Flow Model

As a first step in the numerical simulation of jets, one can restrict attention to low Mach numbers, so that the Navier-Stokes equations for incompressible flow govern the evolution of the rotational components of the velocity. At low Mach number, the acoustic (compressive) part of the velocity couples weakly with the rotational components[2], so it is possible to determine the weakly excited acoustic field after having solved the dynamic equations for the fluid motion. The source terms in the wave equation for the acoustic component are just the quadrupole moments

$$Q(\vec{x},t) = \frac{\partial v_i}{\partial x_j} \frac{\partial v_j}{\partial x_i} \tag{1}$$

where summation over repeated indices is implied and $\vec{v}$ is the three dimensional velocity field. Lighthill's theory implies that the radiated sound field (perturbation density) is proportional to

$$\rho = \frac{1}{4\pi c^2} \int Q\left(\vec{y}, t - \frac{|\vec{x}-\vec{y}|}{c}\right) \frac{d\vec{y}}{|\vec{x}-\vec{y}|} \tag{2}$$

where c is the sound speed and Q is calculated in the incompressible limit (with an error of order Mach number squared).

The Navier-Stokes equations for incompressible flow are

$$\frac{\partial \vec{v}}{\partial t}(\vec{x},t) + \vec{v}(x,t)\cdot\vec{\nabla}\vec{v}(x;t) = -\vec{\nabla}p(\vec{x},t) + \nu\nabla^2\vec{v}(\vec{x},t) \tag{3}$$

$$\vec{\nabla}\cdot\vec{v}(\vec{x},t) = 0$$

where p is the pressure and ν is the kinematic viscosity. The region of importance for noise production in a jet extends from the nozzle downstream to at least 20 jet diameters, while the lateral flow includes the jet together with the surrounding potential flow. Quite a few difficulties arise in the attempt to simulate this flow numerically. Among the most important are:

1. Limited spatial resolution because of limited computer power. Even using a CDC 7600, it is hardly feasible to consider calculations with more than about 10^5 degrees of freedom to resolve the velocity field. With a three dimensional flow field, this limit implies that no more than about 50 degrees of freedom can be used to resolve each flow direction. This is not sufficient to resolve twenty jet diameters downstream.

2. Boundary conditions for a realistic flow field are difficult, though not impossible, to impose. Some of the problems concern: a) the upstream boundary, where the inflow is not known in all detail; b) the downstream boundary, where outflow boundary conditions may cause numerical instabilities; and c) the lateral boundaries, where fluid must be entrained into the jet at the proper rate in order to maintain the proper jet growth.

Because of these difficulties, the problem was further restricted as will now be described. As discussed above, laboratory experiments have determined the large-scale mean-flow characteristics, so that the goal of numerical experimentation on jet noise should be the resolution of the quadrupole-moment distribution. Since the quadrupole source terms are dominated by small-scale motions and since the small scales of turbulent flows largely decouple from large scales[3], it follows that the distribution may be studied by isolating a local section of the jet. This suggests slicing the jet into several sections in the axial direction, and then, within each section, imposing the experimentally determined mean-flow characteristics on the flow. The mean velocity profile within each section is held fixed in time during the numerical calculations, and the turbulent fluctuations are allowed to approach a statistically steady state. After evolving the flow in this way, the quadrupole moments are obtained and can be used in the Lighthill integral to determine the radiated sound field.

At the present time, the flow is also simplified by neglecting the entrainment of fluid at the lateral boundaries. The flow is assumed to take place in a rectangular box with periodic boundary conditions applied in the downstream direction (x_1) and no-stress boundary conditions applied in the lateral directions (x_2 and x_3).

The velocity field is expressed as

$$\vec{v}(\vec{x},t) = \bar{v}(\vec{x}) + \vec{v}'(\vec{x},t)$$

where $\bar{v}$ is the mean velocity and $\vec{v}'$ is the fluctuating velocity. The mean velocity $\bar{v}$ is held constant in time and is of the form

$$\bar{v}(\vec{x}) = U(r)\hat{x}_1$$

where $\hat{x}_1$ is a unit vector in the x_1-direction, r is the distance from the jet axis (in the center of the computational domain), and $U(r)$ is the experimentally observed profile. At the present level of approximation, there is no mean radial velocity since the downstream variation of mean velocity is self-consistently neglected (conservation of mass $\nabla\cdot\vec{v} = 0$ implies that axial variation of $\bar{v}$ induces mean radial velocity). The procedure for handling the fluctuating velocity is discussed in Sects. 3 and 4.

3. Numerical Methods

The Navier-Stokes equations (3), (4) can also be written in rotation form,

$$\frac{\partial \vec{v}(\vec{x},t)}{\partial t} = \vec{v}(\vec{x},t)\times\vec{\omega}(\vec{x},t) - \vec{\nabla}\pi(\vec{x},t) + \nu\nabla^2\vec{v}(\vec{x},t) \tag{5}$$

where $\vec{v}(\vec{x},t)$ is the velocity vector, $\vec{\omega}(\vec{x},t) = \vec{\nabla}\times\vec{v}(\vec{x},t)$ is the vorticity, $\pi(\vec{x},t) = p(x,t) + 1/2|\vec{v}(\vec{x},t)|^2$ is the pressure head, $p(\vec{x},t)$ is the pressure and ν is the kinematic viscosity. The rotation form (5) is advantageous when using pseudospectral approximations since in this form the equations semiconserve energy[4]. This pointwise energy conservation prevents aliasing errors from inducing nonlinear instability, although it has been shown[5] that the appearance of nonlinear instability due to aliasing errors can indicate insufficient resolution.

Given the structure of the problem as described in Section 2, it is convenient to use the following Fourier series representation for the velocity field $\vec{v}(\vec{x},t) = (v_1(\vec{x},t),\ v_2(\vec{x},t),\ v_3(\vec{x},t))$,

$$v_\alpha(\vec{x},t) = \sum_{|k_1|<K_1} \sum_{k_2=0}^{K_2} \sum_{k_3=0}^{K_3} u_\alpha(\vec{k},t)\exp[2\pi i k_1 x_1/L_1]$$

$$\times \begin{cases} \cos \pi k_2 x_2/L_2 \cos \pi k_3 x_3/L_3 & \alpha = 1 \\ \sin \pi k_2 x_2/L_2 \cos \pi k_3 x_3/L_3 & \alpha = 2 \\ \cos \pi k_2 x_2/L_2 \sin \pi k_3 x_3/L_3 & \alpha = 3 \end{cases} \tag{6}$$

where the summation indices k_i are integral and L_i is the box size in the ith direction. Choosing the summation cutoffs as $K_1 = 16$, $K_2 = K_3 = 32$, permits the representation of each velocity component by $(32)^3 = 32768$ Fourier modes so that the entire velocity field involves about 10^5 independent degrees

of freedom. The boundary conditions are periodic at $x_1 = 0$, and are stress-free at $x_2 = 0,\ L_2$ and $x_3 = 0,\ L_3$:

$$\frac{\partial v_1}{\partial x_2} = \frac{\partial v_3}{\partial x_2} = v_2 = 0 \quad \text{on} \quad x_2 = 0,\ L_2$$

$$\frac{\partial v_1}{\partial x_3} = \frac{\partial v_2}{\partial x_3} = v_3 = 0 \quad \text{on} \quad x_3 = 0,\ L_3$$

$$\vec{v}(x_1 + mL_1, x_2, x_3) = \vec{v}(x_1, x_2, x_3) \quad m \text{ integral} \tag{7}$$

Equations for the Fourier components $\vec{u}(\vec{k})$ are derived by Galerkin's procedure[4]. After applying the incompressibility condition (4) to eliminate the pressure, the equations for $\vec{u}(\vec{k})$ are found to be (in the special case $L_1 = 2\pi$, $L_2 = L_3 = \pi$)

$$\frac{\partial \hat{u}_\alpha(\vec{k},t)}{\partial t} + \nu k^2\, \hat{u}_\alpha(\vec{k},t) = -k_\beta(\delta_{\alpha\gamma} - k_\alpha k_\gamma/k^2) \sum_{\substack{\vec{p}+\vec{q}=\vec{k} \\ |p_i|<K_i \\ |q_i|<K_i}} \hat{u}_\beta(\vec{p},t)\,\hat{u}_\gamma(\vec{q},t) \tag{8}$$

where

$$\hat{u}_\alpha(\vec{k},t) = \begin{cases} \frac{1}{4}u_1(k_1,|k_2|,|k_3|,t) & \alpha = 1 \\ \frac{1}{4i}\mathrm{sgn}(k_2)\,u_2(k_1,|k_2|,|k_3|,t) & \alpha = 2 \\ \frac{1}{4i}\mathrm{sgn}(k_3\,u_3(k_1,|k_2|,|k_3|,t) & \alpha = 3 \end{cases} \tag{9}$$

The system (8) can be solved numerically by using fast Fourier transforms to evaluate the convolution sums, leap-frog time differencing on the nonlinear terms, and Crank-Nicolson (implicit) time differencing on the viscous terms. This method of solution requires the use of 18 Fourier transforms on $(32)^3$ points per time step.

With the representation of the velocity field requiring about 10^5 computer storage locations, the current code requires the buffering of data between small core memory, large core memory and disks. Small core memory on the CDC 7600 has 65K words and large core has 250K words. The code has been sped up by about a factor of 2 over the original Fortran version by programming many of the critical internal loops in assembly language, and now requires about 6 seconds of computer time per time step. The runs discussed later required from 300 to about 1000 time steps to achieve a statistically steady state.

4. Description of the Simulations

The initial mean velocity profile in the numerical experiments was chosen to correspond to the experimentally measured mean velocity profile of an axisymmetric subsonic cold jet [1,6]. The experimental apparatus consisted of a long pipe with a nozzle diameter of $d_0 = .0625$ meters. The mean exit velocity was 213m/sec corresponding to a Mach number of 0.62. The cylindrical coordinate system $(\bar{X}_1, r)$ is used, where $\bar{X}_1$ is the distance (expressed in units of the jet diameter) along the jet axis from the virtual origin of the jet and r corresponds to the radial distance from the jet axis. The jet spreads downstream, its boundary making an angle of $\theta_e = 11°$ with the $\bar{X}_1$ axis. In this flow, the virtual origin of the jet corresponds to a distance $\bar{X}_0 = -2.57$ upstream of the mouth of the nozzle, located at $\bar{X}_1 = \bar{X}_0$.

The mean velocity profiles have been characterized in two self-similar regions: a mixing region, just downstream of the jet nozzle, corresponding to $0 \leq D \leq 5$, and a fully turbulent region for $D > 5$, where $D = \bar{X}_1 - \bar{X}_0$. In particular, for $0 \leq D \leq 5$,

$$\frac{\bar{U}(\bar{X}_1, r)}{\bar{U}_c(\bar{X}_1)} = \begin{cases} 1, & r \leq .5 - .102(1+D) \\ \exp(-61.53(\mu_2 + .102)^2), & r > .5 - .102(1+D) \end{cases} \tag{10}$$

where $\bar{U}_c(\bar{X}_1)$ is the mean centerline jet velocity, and

$$\mu_2 = \frac{r - .5}{1+D} \tag{11}$$

and for $D > 5$,

$$\frac{\bar{U}(\bar{X}_1, r)}{\bar{U}_c(\bar{X}_1)} = \exp(-1.44(\mu_3 + .69)^2) \tag{12}$$

where

$$\mu_3 = 10.3\{\frac{r}{\bar{X}_1}\} - .69 \tag{13}$$

Superimposed on the given mean velocity field is a turbulent fluctuating component $\vec{v}'(\vec{x},t)$. To ensure that $\vec{v}'(\vec{x},t)$ satisfies the incompressibility constraint (4), we express $\vec{v}'(\vec{x},t)$ in the form

$$\vec{v}'(\vec{x},t) = \vec{\nabla}\times\vec{A}'(\vec{x}) \tag{14}$$

where the vector potential $\vec{A}'(\vec{x})$ is of the form

$$\vec{A}'(\vec{x}) = [I(r)]^{1/2}\,\vec{B}(\vec{x})$$

Here, $\vec{B}(\vec{x})$ is chosen as a realization of a homogeneous, isotropic random field with specified isotropic energy spectrum $E(k)$, while $I(r)$, the intensity function, is chosen in accordance with the experimental data on the root-mean-square turbulent intensity[1]. $E(k)$ is of the form

$$E(k) = Ak^4\exp(-Bk^2). \tag{16}$$

$I(r)$ has been approximated at various downstream positions D, e.g. at $D = 4$

$$R(s) = [I(r)]^{1/2} = \begin{cases} .16-.11\exp(-5s^2) & 0<s<1 \\ .159\ \exp(-1.5(s-1)) & s>1 \end{cases} \tag{17}$$

where $s = 2r/d_0$. Also, we use

$$R(s) = \begin{cases} .185 - .055\exp(-8s^2) & 0<s<.55 \\ .183\exp(-.7(s-.65)^2) & s>.65 \end{cases} \quad \text{for } D=8 \tag{18}$$

$$R(s) = \begin{cases} .225 - .045\exp(-16s^2) & 0<s<.4 \\ .2215\exp(-.5(s-.4)^2) & s>.4 \end{cases} \quad \text{for } D=12 \tag{19}$$

Three principal runs are reported corresponding to locations D = 4, 8, and 12 jet diameters downstream of the jet exit. Each computational slab extends over about 2-3 jet diameters in the downstream direction (the variation being due to the need for increased size of the computational box further downstream). The initial mean flow profiles are shown in Figs. 1, 2.

Finally, it is important to discuss the Reynolds numbers of the simulations. In all three simulations, $\nu = .006 m^2/s$ so that the Reynolds number based on jet diameter and centerline velocity is about $R \sim 22{,}000$. On the other hand, the laboratory jet is run in air with the much lower viscosity $\nu = 1.5 \times 10^{-5}\ m^2/s$ giving a Reynolds number roughly 40 times larger. The important question concerns how these two flows, numerical and laboratory, can possibly relate to each other considering the huge discrepancy in Reynolds number. However, this discrepancy in Reynolds numbers appears to be important only at the very smallest scales and not at those scales of motion responsible for sound generation. In fact, this is consistent with Lighthill's theory[7] which shows that neither energy-containing nor energy-dissipating eddies dominate the noise generation process; rather, noise generation is dominated by an intermediate range of eddies whose size is roughly eight times smaller than the energy-containing eddies. It has been shown elsewhere[8] that such intermediate scales of motion are already approximately Reynolds number independent at the Reynolds numbers of the numerical simulations. The principal source of Reynolds number dependence of laboratory jet flows is not the intrinsic viscous effect on the fluid motion, but rather is due to the viscous effect on the boundary layers at the jet exit which governs the flow through its initial and boundary conditions. <u>In the numerical simulations, the viscous effect on upstream boundary and initial conditions is avoided by use of mean profiles corresponding to Reynolds numbers of order 800,000 not 20,000</u>. In this way it is expected that the numeri-

cal simulations avoid most of the pitfalls of Reynolds number effects and thereby give results useful for the study of noise production.

Some results of the numerical simulations are presented in Figs. 3-34. Here the three components of velocity are contoured within several slices of the computational domain at several evolution times (measured in seconds) and at the three downstream locations D = 4, 8, 12. These figures show the characteristic jet shape as well as indicating the nature of the motions resolved by the simulations.

The quadrupole moment distribution $Q(\vec{x},t)$ for the three simulations is contoured in Figs. 35-58, again for several times, locations, and slices. It is striking how the quadrupole moment distribution is so much more localized and spotty than the velocity field itself, consistent with our treatment of a slab of the jet isolated from its surroundings.

5. Discussion

The results of the simulations discussed in Sec. 4 are being used together with Lighthill's integral to determine the radiated sound field of the jet. For this purpose, Lighthill's integral is broken up into contributions from the several downstream slabs whose contributions are then superposed. The results of this calculation will be reported later.

It is important to emphasize that noise generation is possible despite the periodic boundary conditions that are applied to the computational domain, because the contributions from neighboring slabs are distinct and do not cancel.

There are at least three areas where the present computations are being extended and improved. They are:

1) Inclusion of a nonlinear eddy viscosity to model the effects of unresolved turbulence. These calculations with a subgrid scale eddy viscosity are being compared with those with the molecular viscosity discussed here, in order to better gauge the Reynolds number effects on the simulations.

2) Inclusion of compressibility, so that noise production at higher Mach numbers can be studied.

3) Inclusion of realistic jet geometry, including jet growth, entrainment, and inflow-outflow boundary conditions. Because of limited spatial resolution on available computers, these flow simulations in realistic jet geometries are limited presently to about the first five jet diameters downstream.

The latter improvement will permit the proper simulation of jets in the presence of a pressure gradient by allowing for jet expansion downstream.

Another problem of interest is the study of the present simulations for evidence of coherent large scale flow structures, as observed recently by Crow & Champagne, Laufer, and others. While these large-scale flow structures probably do not dominate noise production, they may give a component of the noise that is controllable. In this way, it may be possible to achieve the design of minimum noise flows at a given flow rate and Mach number.

REFERENCES

1. Liu, C. H.; and Maestrello, L.: Propagation of Sound Through a Real Jet Flow Field. AIAA Paper No. 74-5, Presented at the AIAA 12th Aerospace Sciences Meeting, Washington, D. C., January 30-February 1, 1974.

2. Lighthill, M. J.: On Sound Generated Aerodynamically: I. General Theory. Proc. Roy. Soc, vol. 211A, pp. 564-587, 1952.

3. Orszag, S. A.: Lectures on the Statistical Theory of Turbulence in Proceeding of the 1973 Les Houches Summer School. Gordon and Breach (Paris), 1975.

4. Orszag, S. A.: Numerical Simulation of Incompressible Flow within Simple Geometries: I. Galerkin (Spectral) Representations. Stud. in Appl. Math., vol. 50, p. 293, 1971.

5. Fox, D. G.; and Orszag, S. A.: Pseudospectral Approximation to Two-Dimensional Turbulence. J. Comp. Phys., vol. 11, p. 612, 1973.

6. Maestrello, L.; and McDaid, E: Near-Field Characteristics of a High Subsonic Jet. AIAA Paper No. 71-155, January 1971.

7. Lighthill, M. J.: On Sound Generated Aerodynamically: II.Turbulence as a Source of Sound. Proc. Roy. Soc, vol. 222A, pp. 1-32, 1954.

8. Orszag, S. A.: Numerical Simulation of Turbulent Flows. Flow Research Report No. 52, 1974.

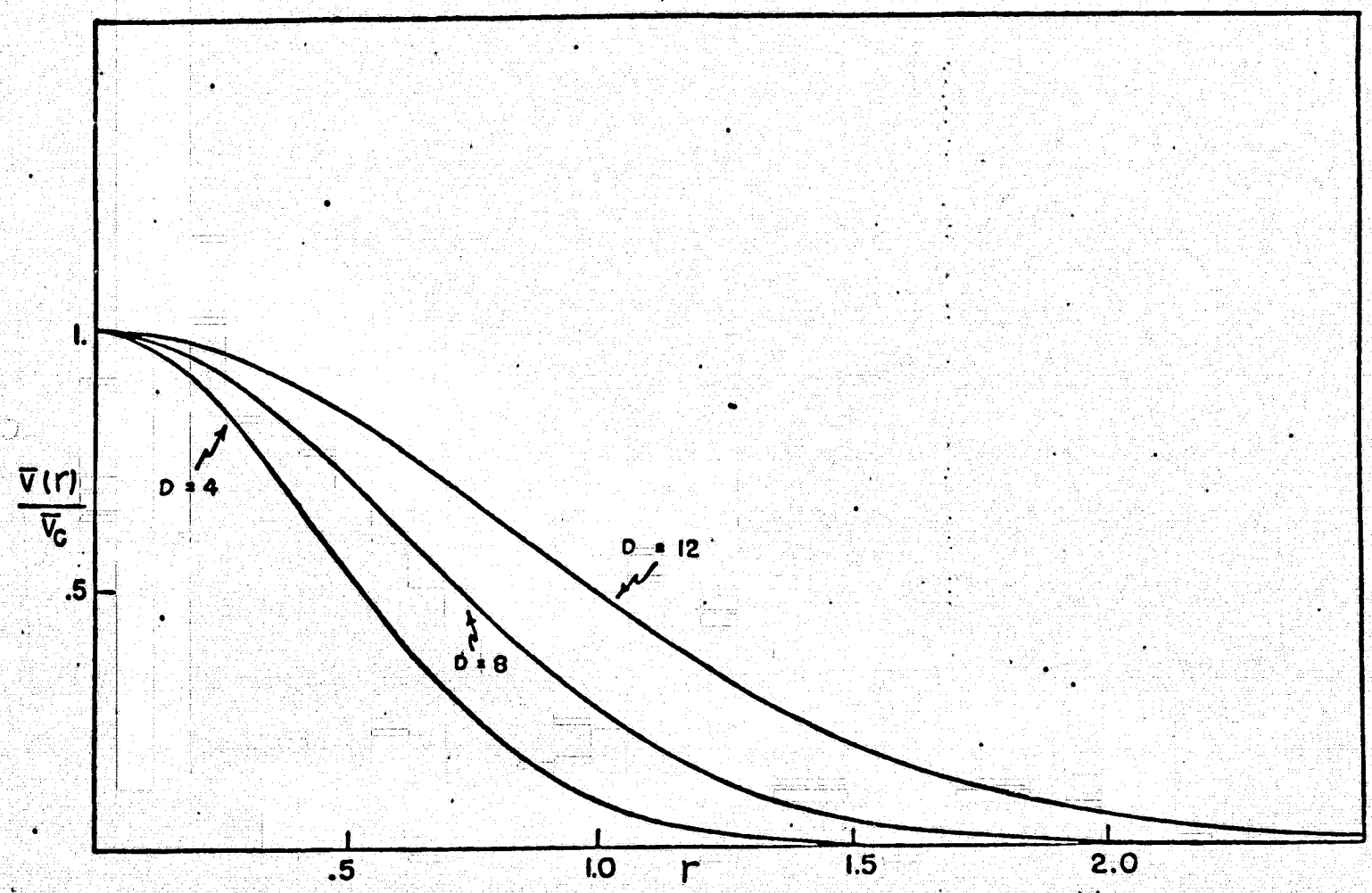

Fig. 1. Initial mean velocity profiles at three downstream positions

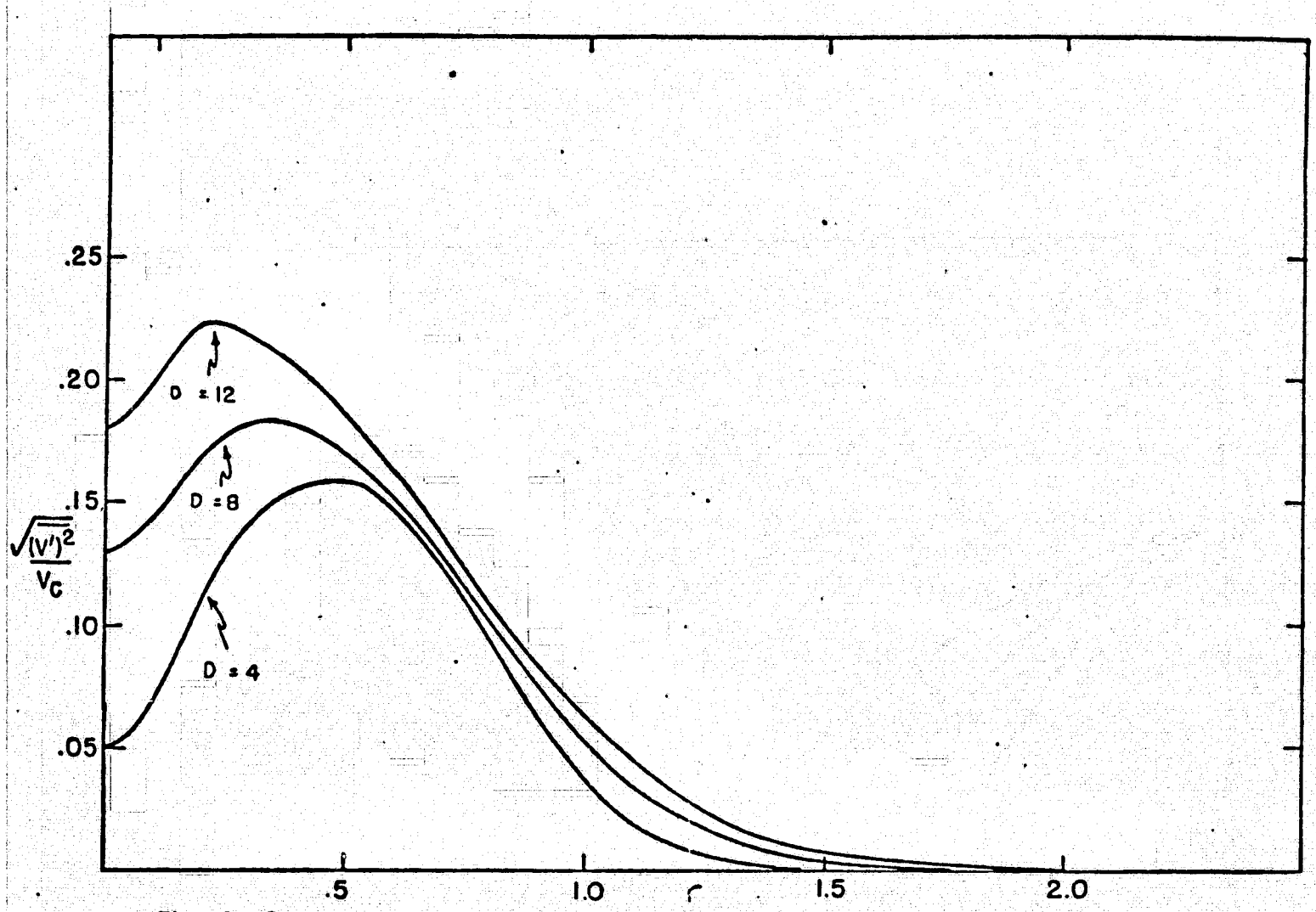

Fig. 2. Root mean square turbulent intensities at three downstream positions

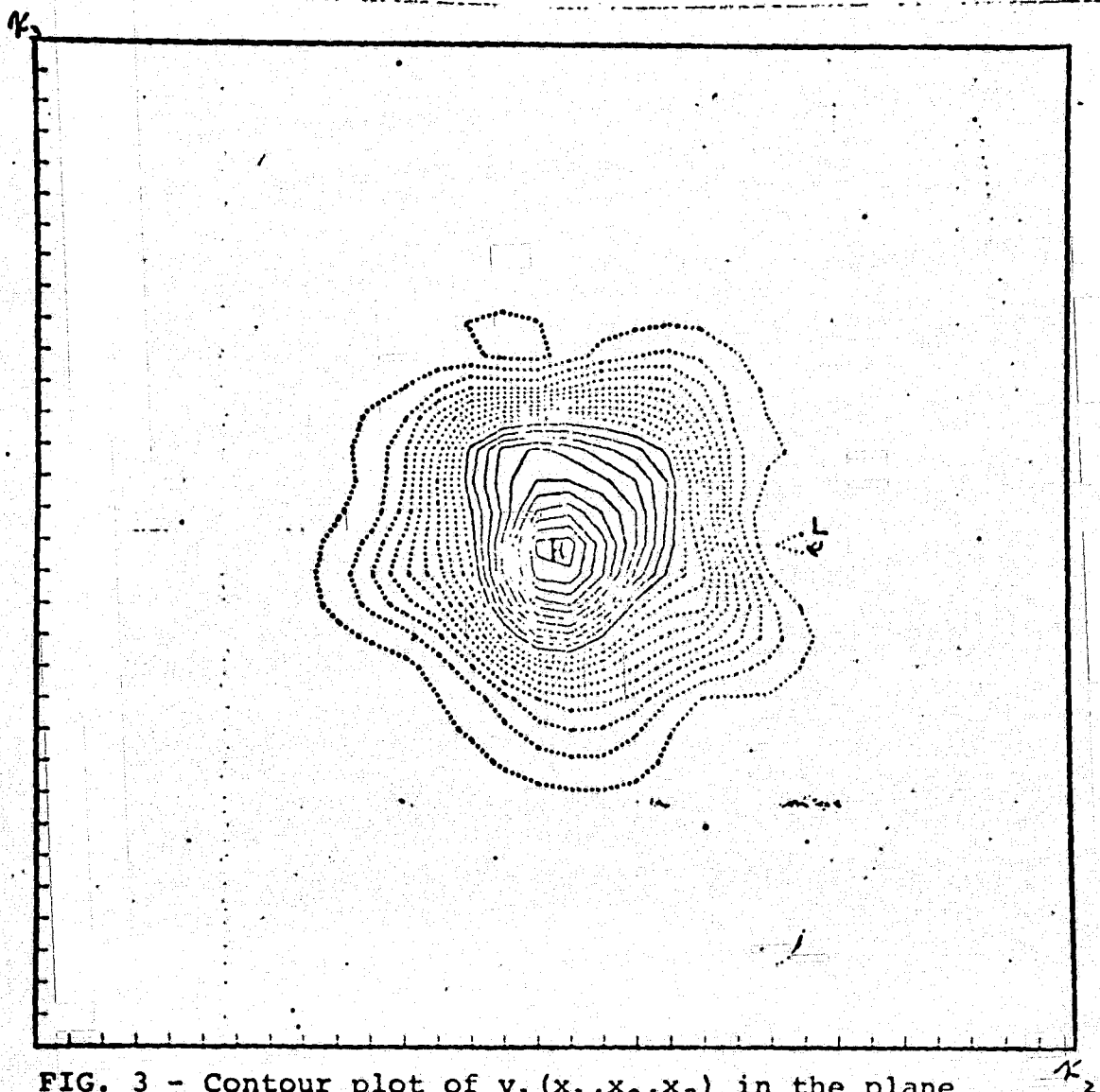

FIG. 3 - Contour plot of $v_1(x_1,x_2,x_3)$ in the plane $x_1=\frac{1}{2}L$ at $\overline{X}=4$ diameters downstream from the jet exit. Here t=0, the contour minimum $v_{min}=-1.1(2)$, the contour maximum $v_{max}=1.(2)$ and the contour interval $\Delta v=1.(1)$. The time t is the time of evolution with t=0 the initial turbulent state.

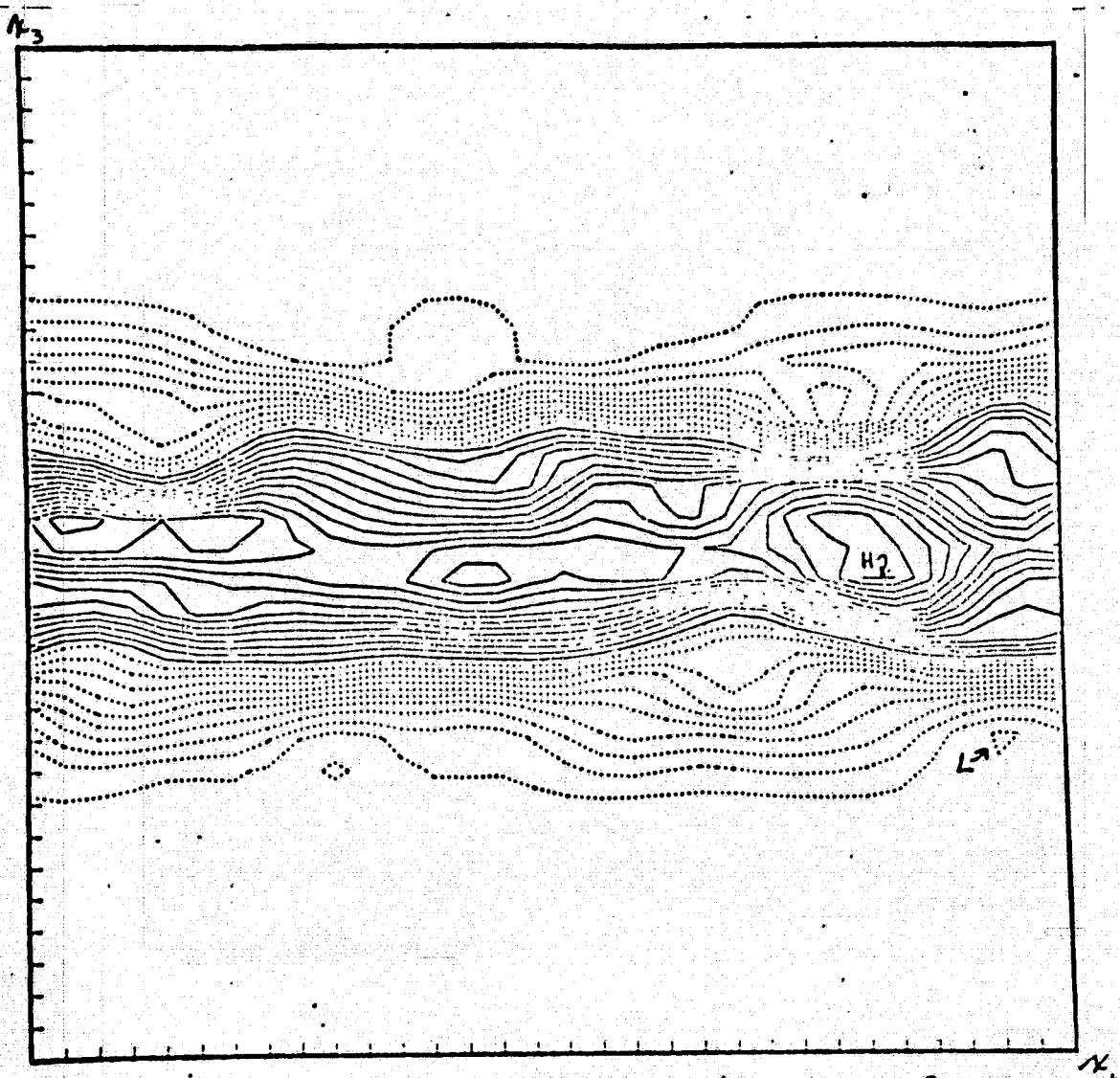

FIG. 4 - Same as Fig. 3 except the contours are for v_1 in the plane $x_2=\frac{1}{2}L$. Here t=0, $\bar{X}=4$, $v_{min}=-1.1(2)$, $v_{max}=1.4(2)$, $\Delta v=1.(1)$.

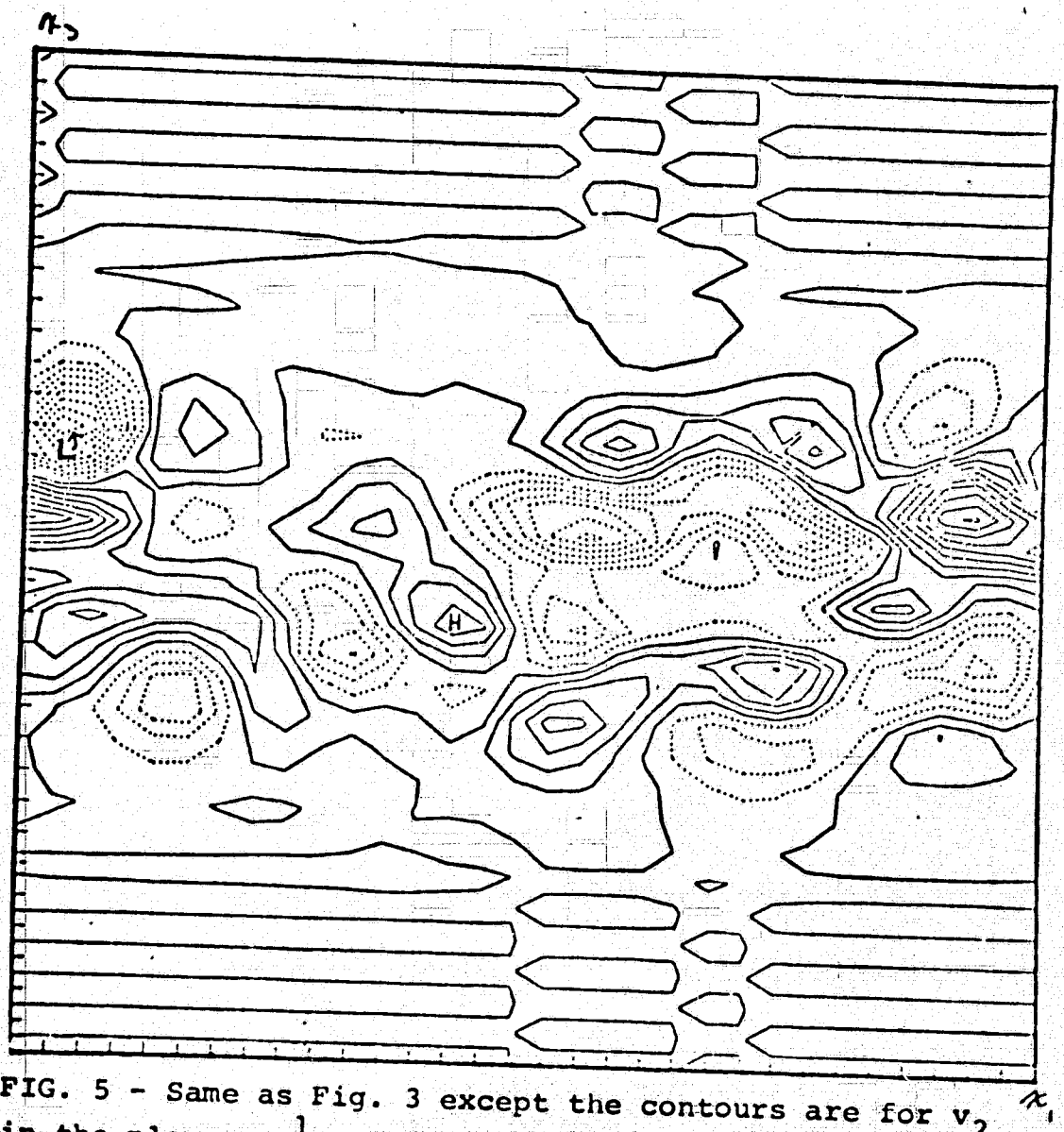

FIG. 5 - Same as Fig. 3 except the contours are for v_2 in the plane $x_2=\frac{1}{2}L$. Here $t=0$, $\bar{X}=4$, $v_{min}=-9.(1)$, $v_{max}=9.(1)$, $\Delta v=1.(1)$.

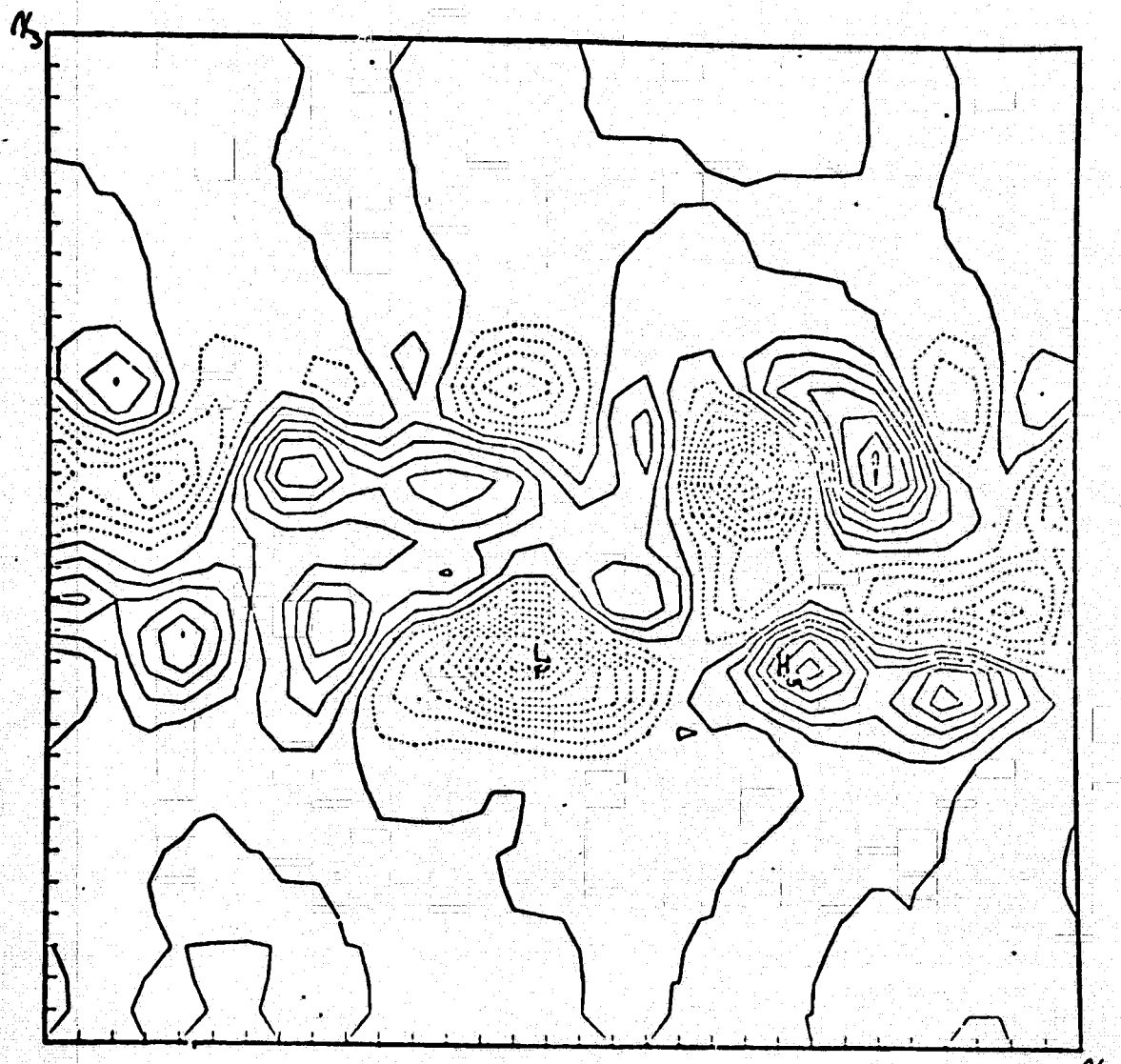

FIG. 6 - Same as Fig. 3 except the contours are for v_3 in the plane $x_2=\frac{1}{2}L$. Here $t=0$, $\overline{X}=4$, $v_{min}=-6.(1)$, $v_{max}=4.2(1)$, $\Delta v=6.(0)$.

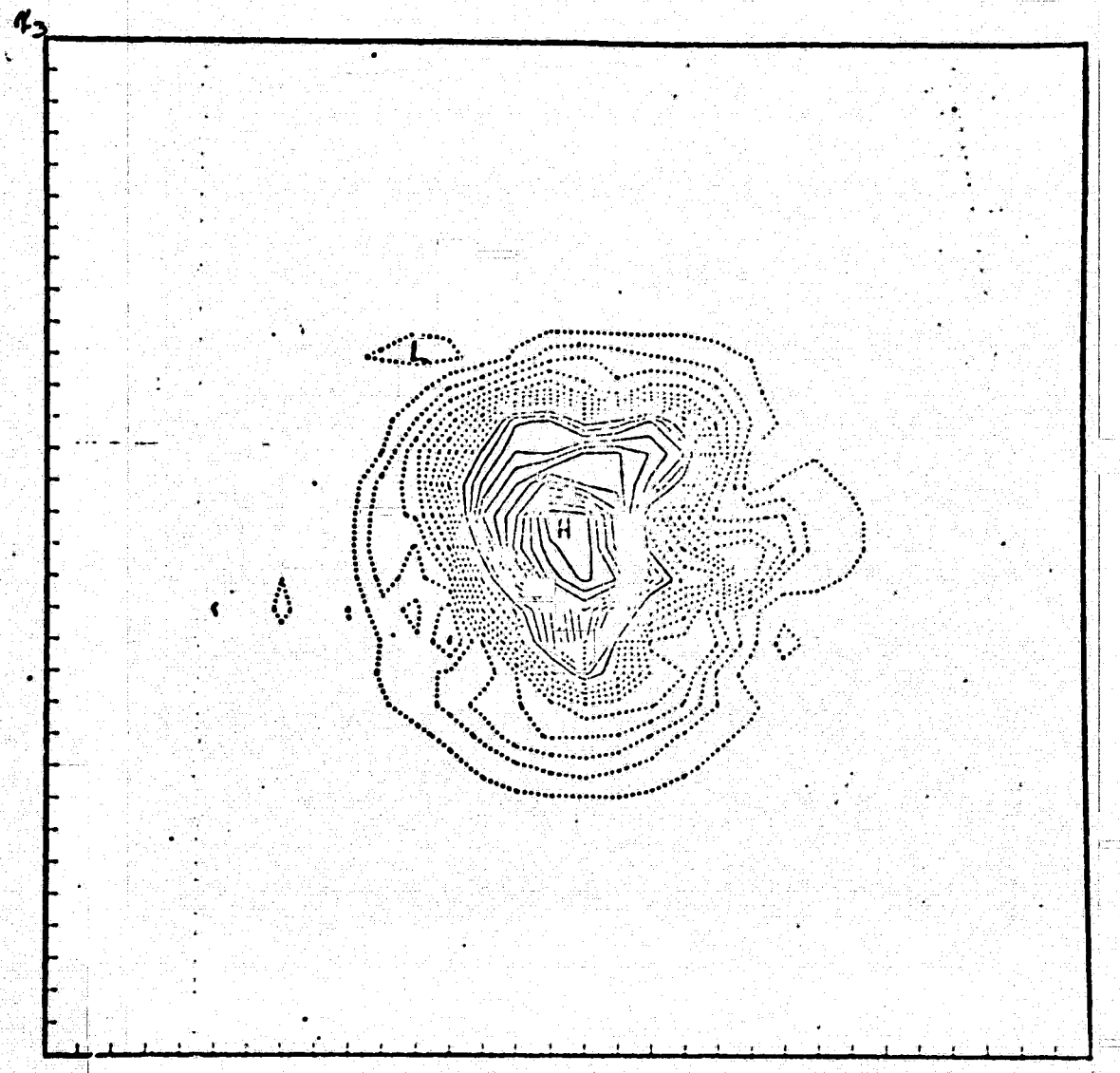

FIG. 7 - Same as Fig. 3 except the contours are for v_1 in the plane $x_1=\frac{1}{2}L$. Here t=.020, $\overline{X}$=4, v_{min}=-1.1(2), v_{max}=1.1(2), Δv=1.(1).

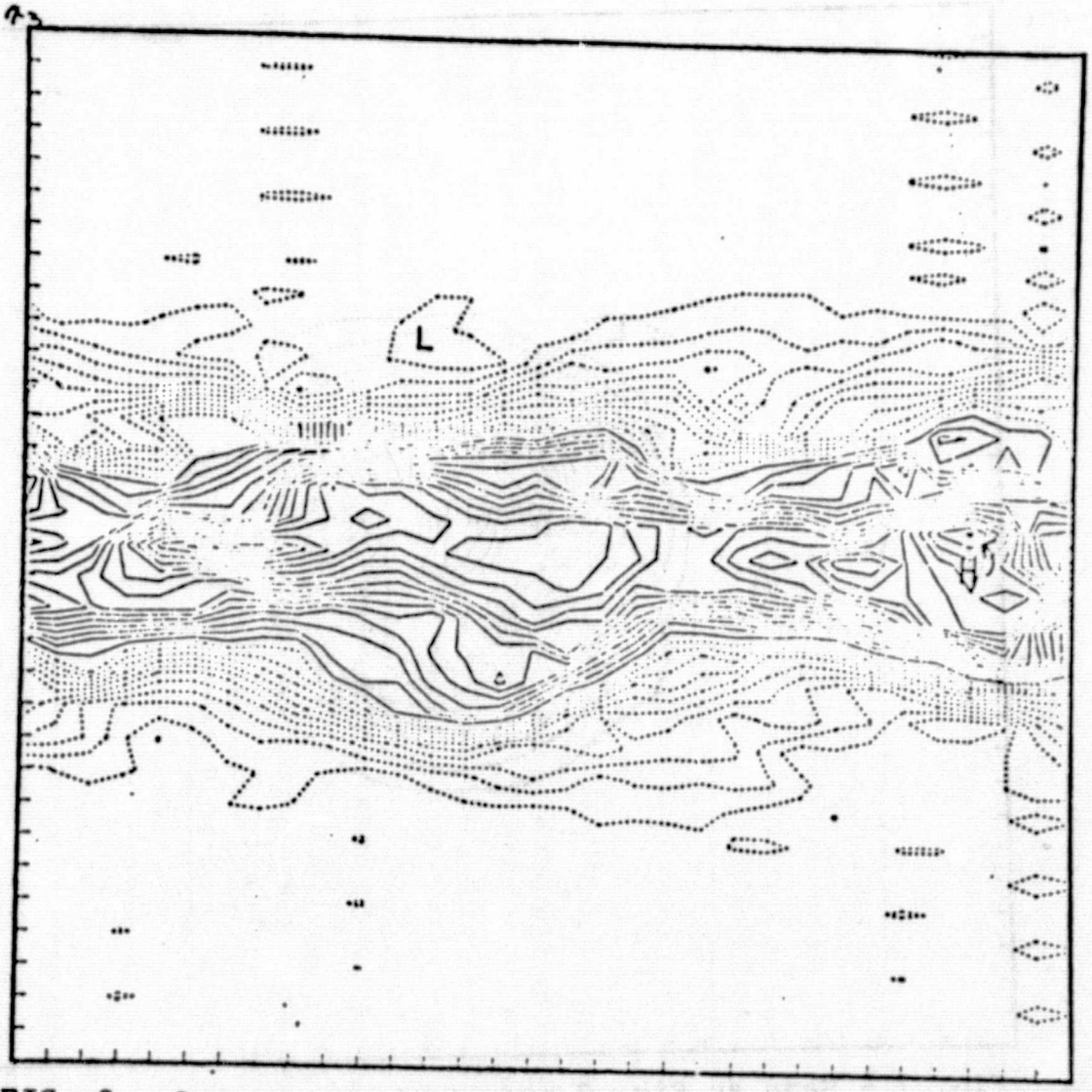

FIG. 8 - Same as Fig. 3 except the contours are for v_1 in the plane $x_2=\frac{1}{2}L$. Here t=.020, $\overline{X}$=4, v_{min}=-1.2(2), v_{max}=1.7(2), Δv=1.(1).

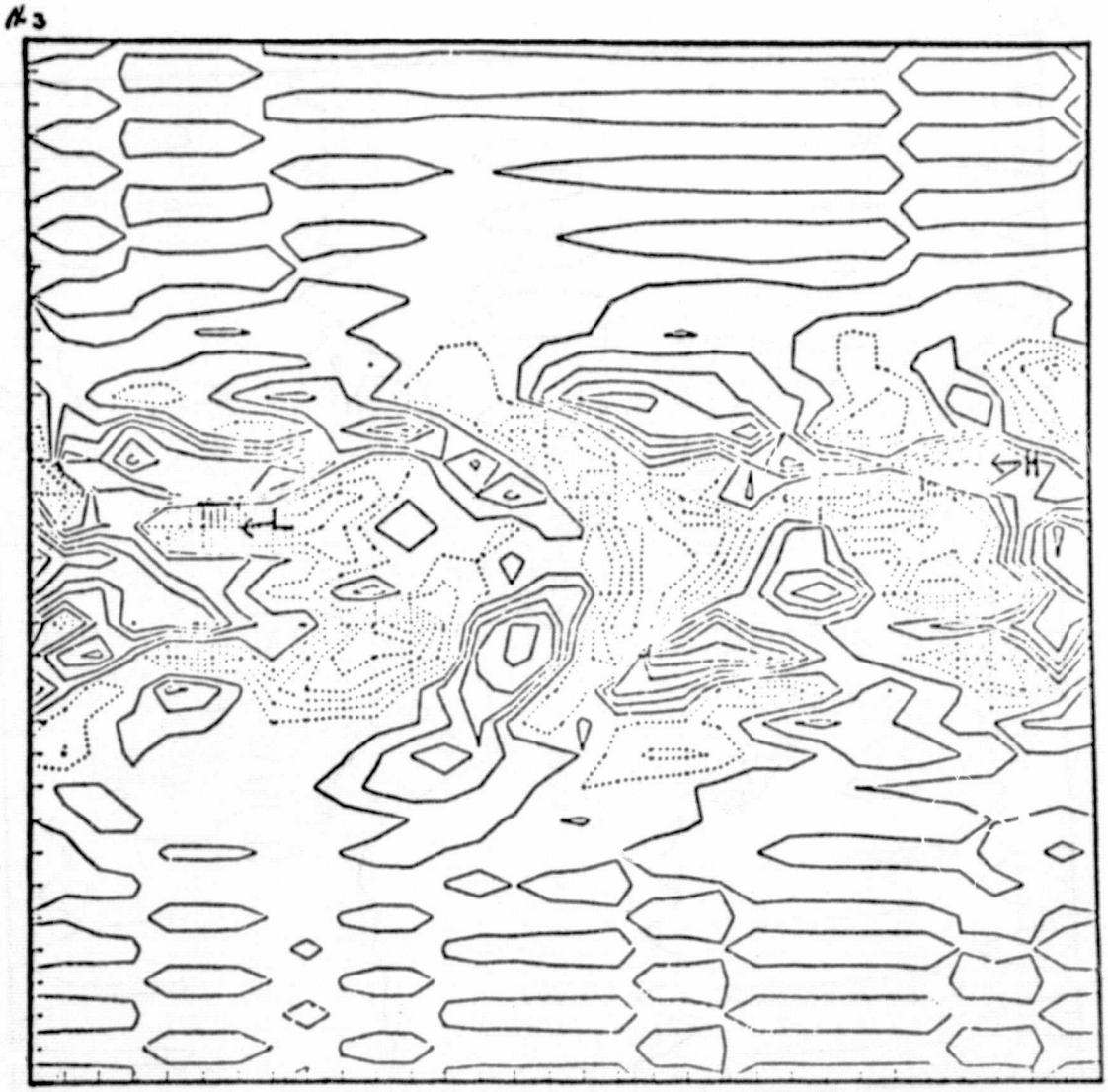

FIG. 9 - Same as Fig. 3 except the contours are for v_2, in the plane $x_2=\frac{1}{2}L$. Here t=.020, $\bar{X}$=4, v_{min}=-7.(1), v_{max}=8.(1), Δv=1.(1).

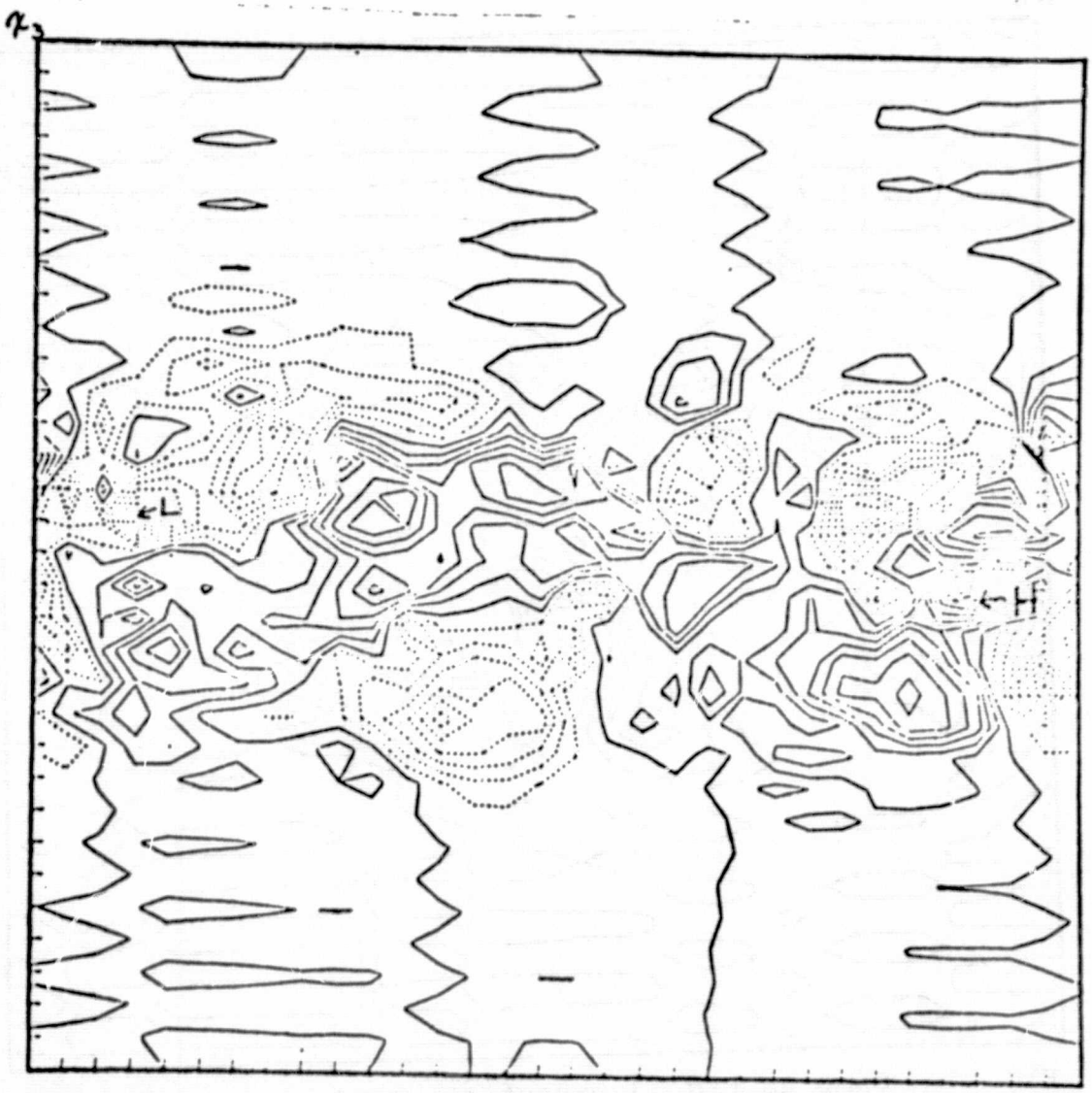

FIG. 10 - Same as Fig. 3 except the contours are for v_3, in the plane $x_2=\frac{1}{2}L$. Here t=.020, $\overline{X}$=4, v_{min}=-6.4(1), v_{max}=5.6(1), Δv=8.(0).

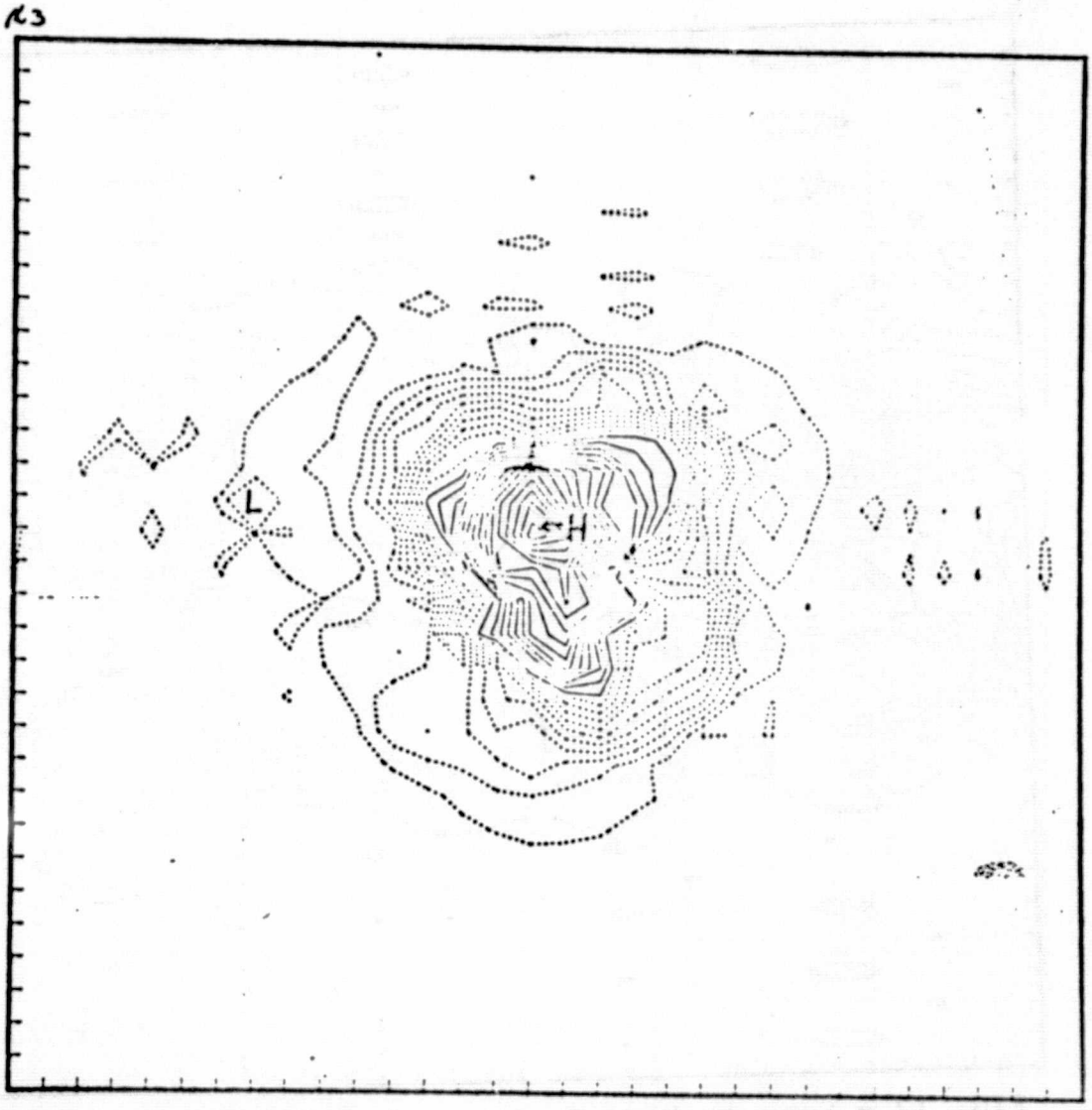

FIG. 11 - Same as Fig. 3 except the contours are for v_1 in the plane $x_1=\frac{1}{2}L$. Here t=.031, $\bar{X}=4$, $v_{min}=-1.1(2)$, $v_{max}=1.4(2)$, $\Delta v=1.(1)$.

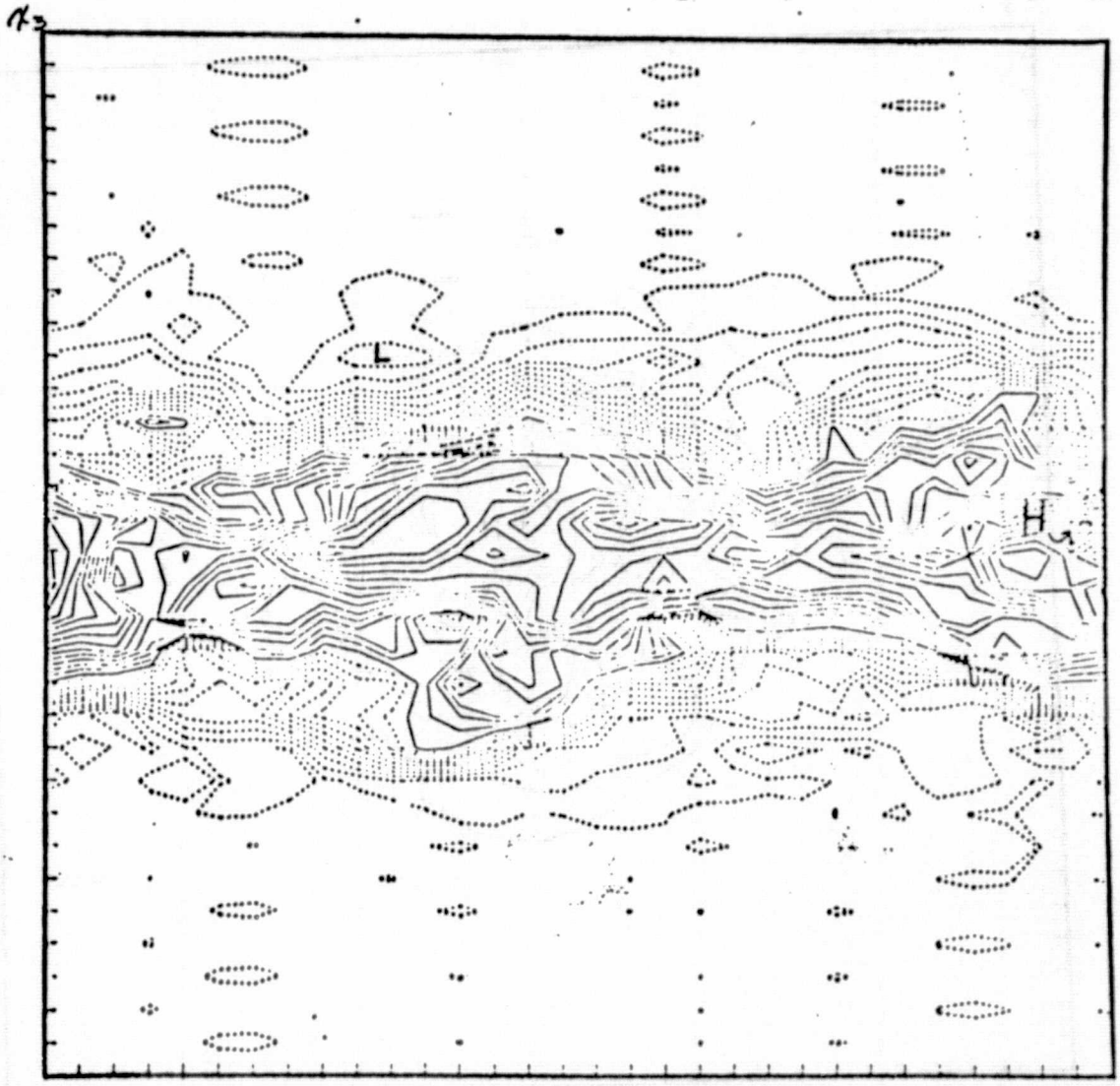

FIG. 12 - Same as Fig. 3 except the contours are for v_1, in the plane $x_2=\frac{1}{2}L$. Here t=.031, $\overline{X}$=4, v_{min}=-1.3(2), v_{max}=1.8(2), Δv=1.(1).

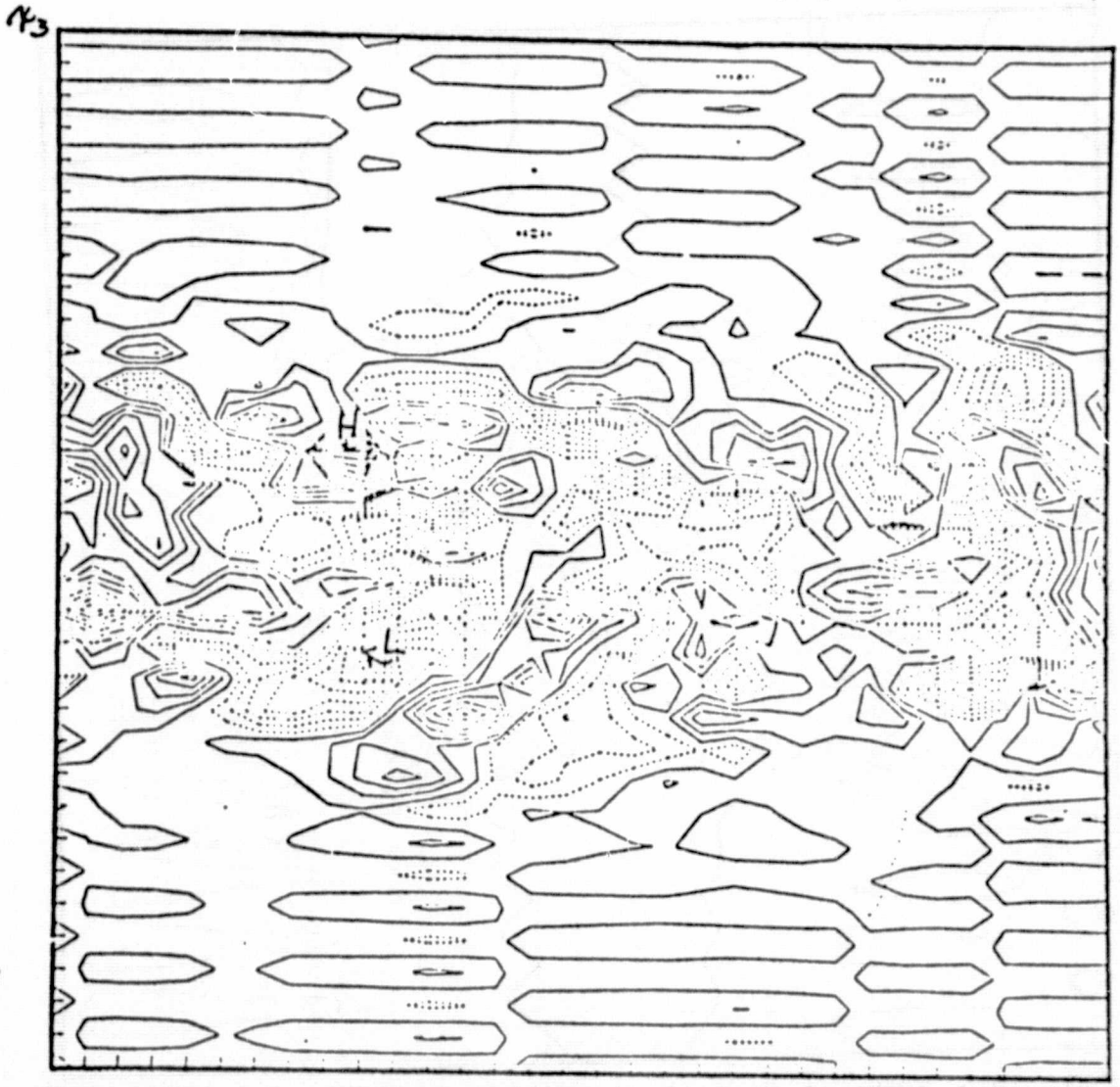

FIG. 13 - Same as Fig. 3 except the contours are for v_2, in the plane $x_2=\frac{1}{2}L$. Here t=.031, $\overline{X}$=4, v_{min}=-9.(1), v_{max}=9.(1), Δv=1.(1).

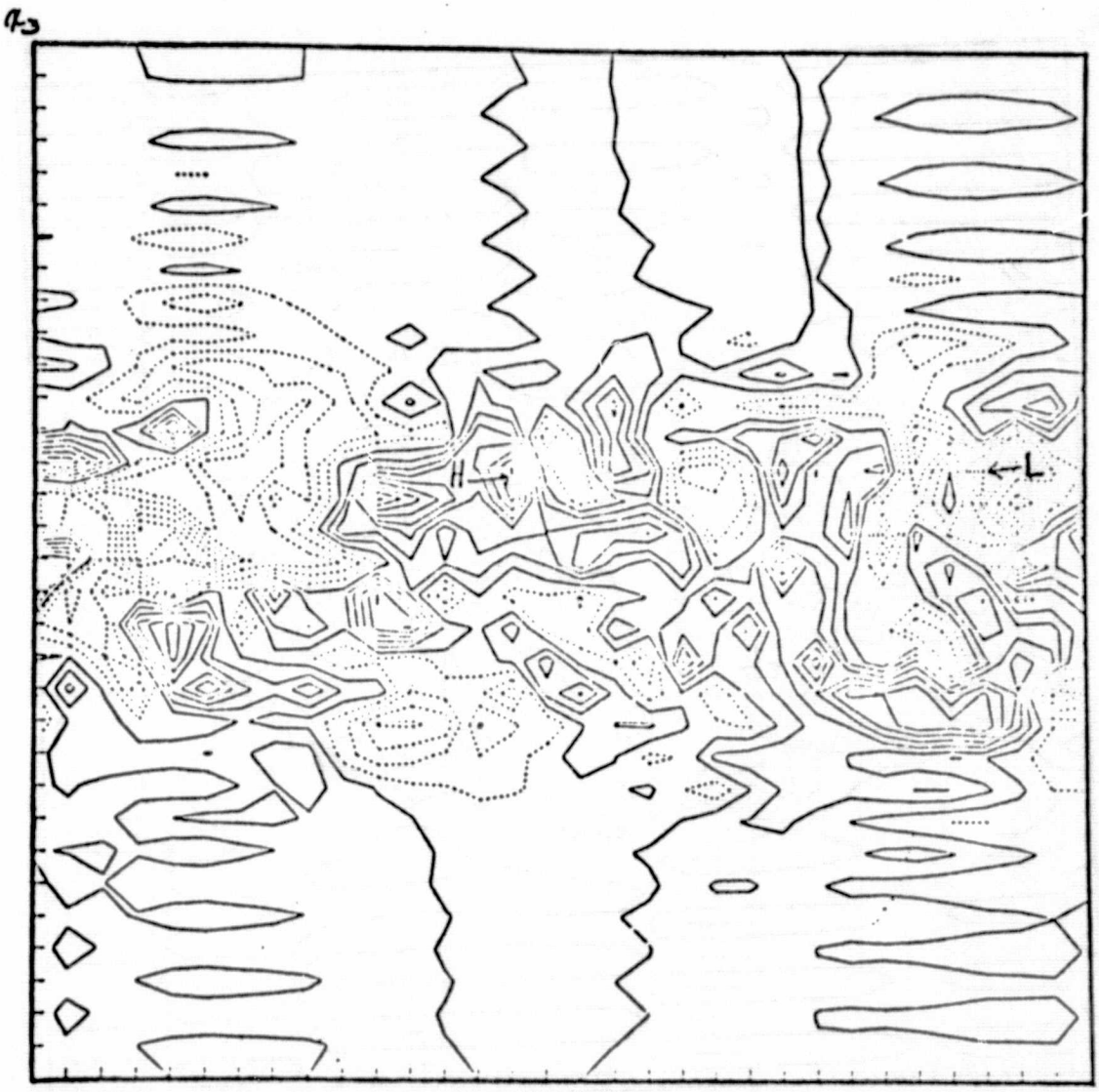

FIG. 14 - Same as Fig. 3 except the contours are for v_3 in the plane $x_2=\frac{1}{2}L$. Here t=.031, $\bar{X}$=4, v_{min}=-8.(1), v_{max}=8.(1), Δv=1.(1).

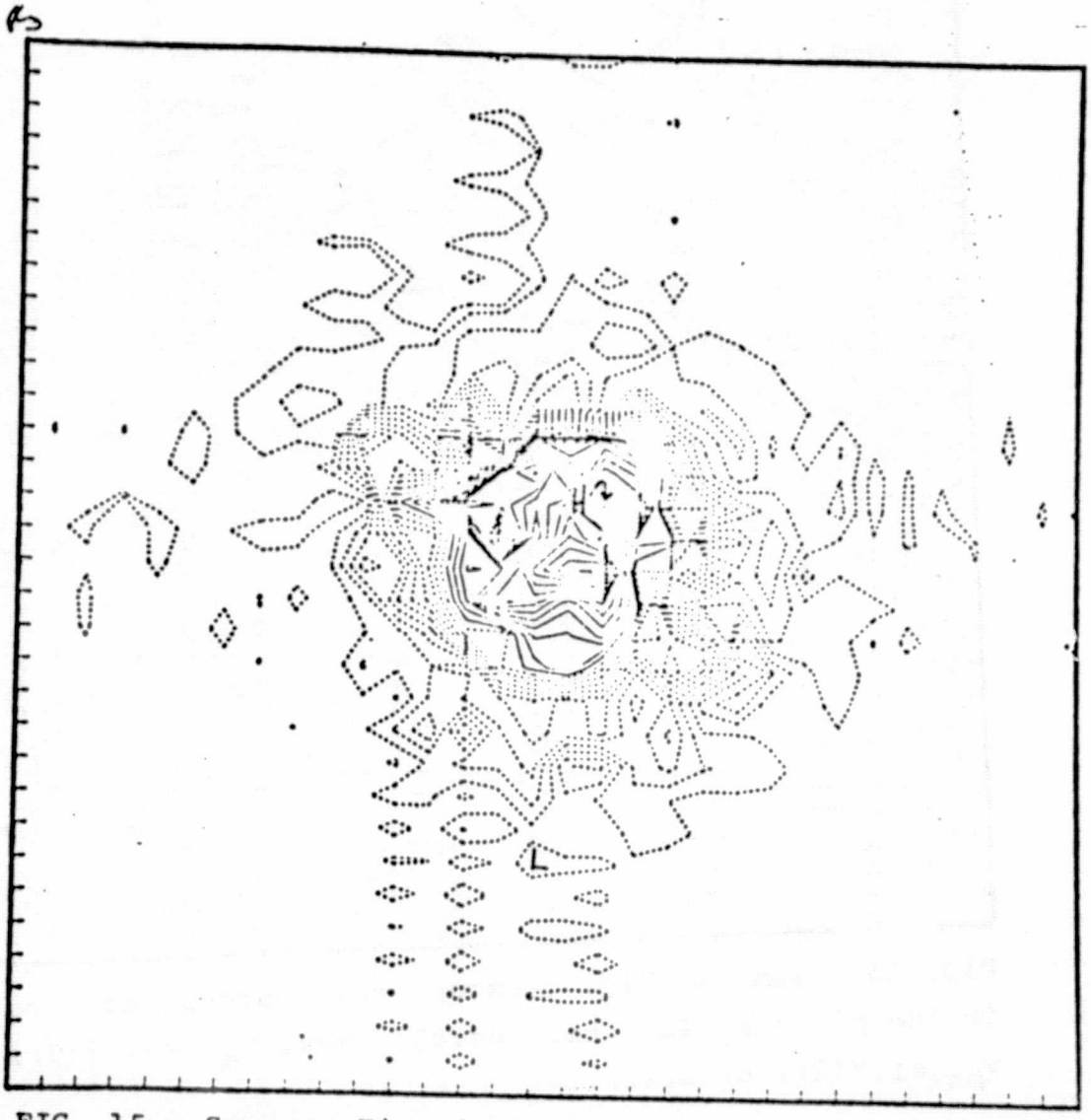

FIG. 15 - Same as Fig. 3 except the contours are for v_1 in the plane $x_1=\frac{1}{2}L$. Here t=.051, $\overline{X}$=4, v_{min}=-1.4(2), v_{max}=1.4(2), Δv=1.(1).

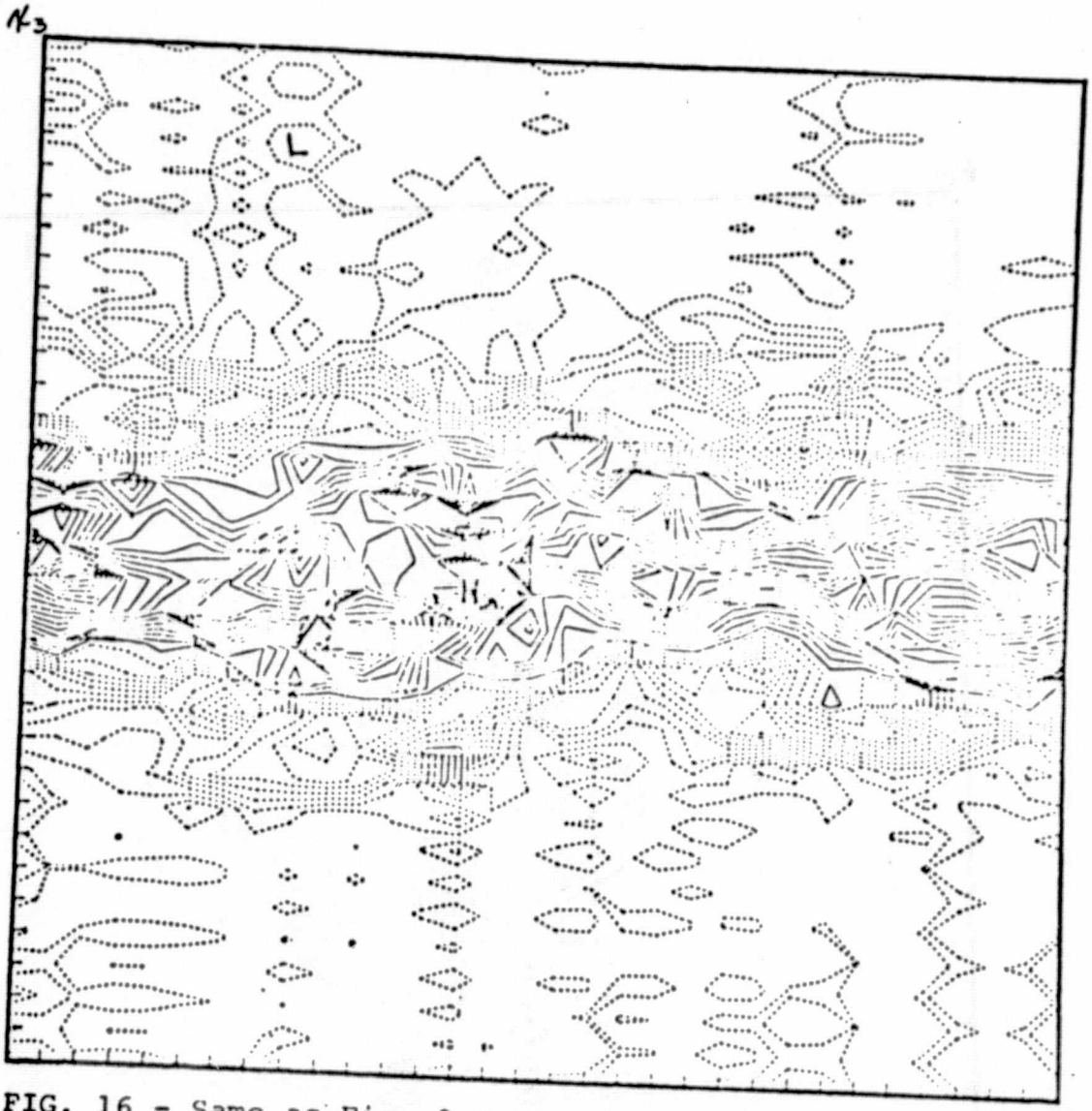

FIG. 16 - Same as Fig. 3 except the contours are for v_1 in the plane $x_2=\frac{1}{2}L$. Here t=.051, $\overline{X}$=4, v_{min}=-1.3(2), v_{max}=1.7(2), Δv=1.(1).

x_3

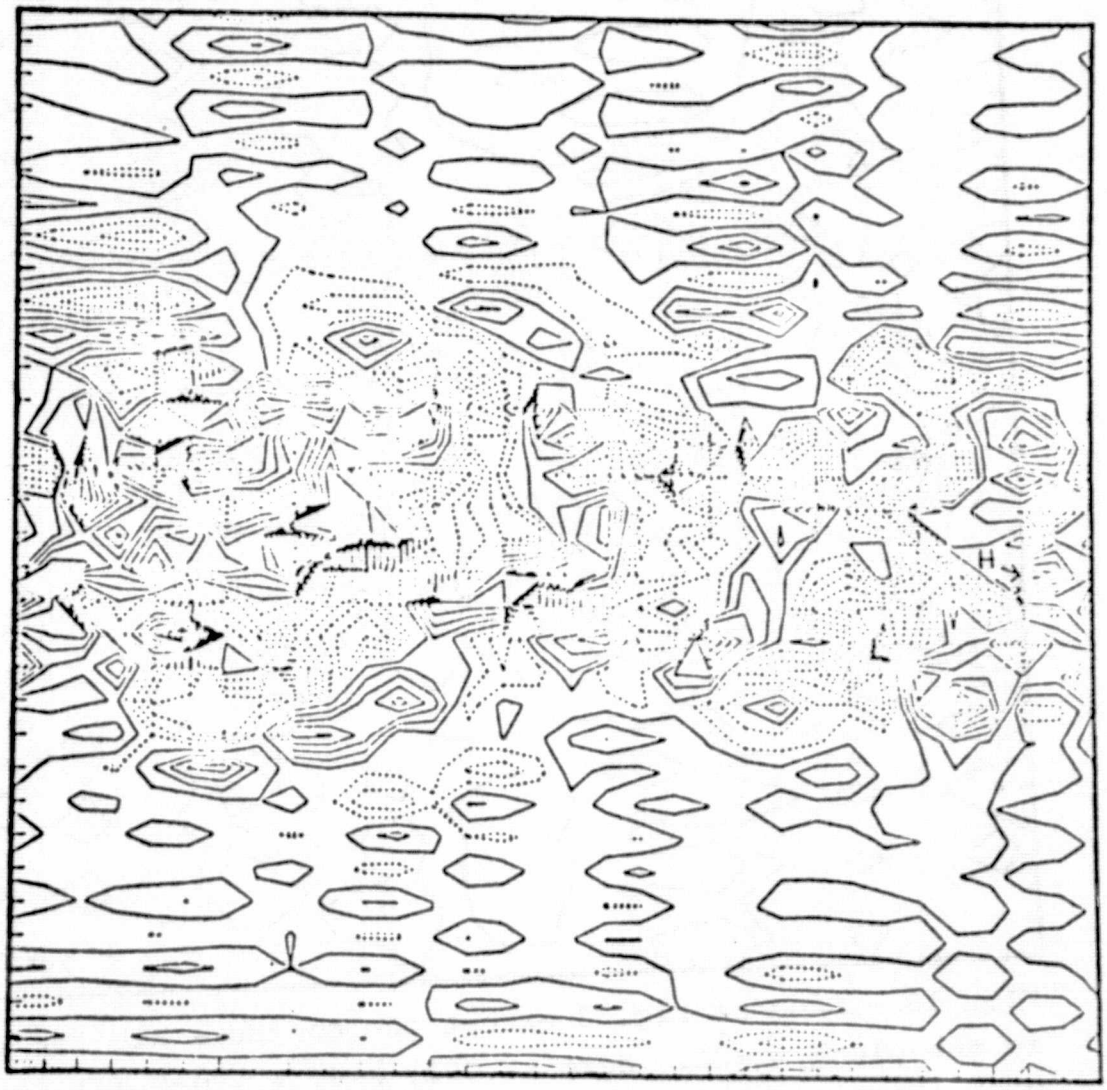

x_1

FIG. 17 - Same as Fig. 3 except the contours are for v_2 in the plane $x_2=\frac{1}{2}L$. Here $t=.051$, $\overline{X}=4$, $v_{min}=-1.2(2)$, $v_{max}=9.(1)$, $\Delta v=1.(1)$.

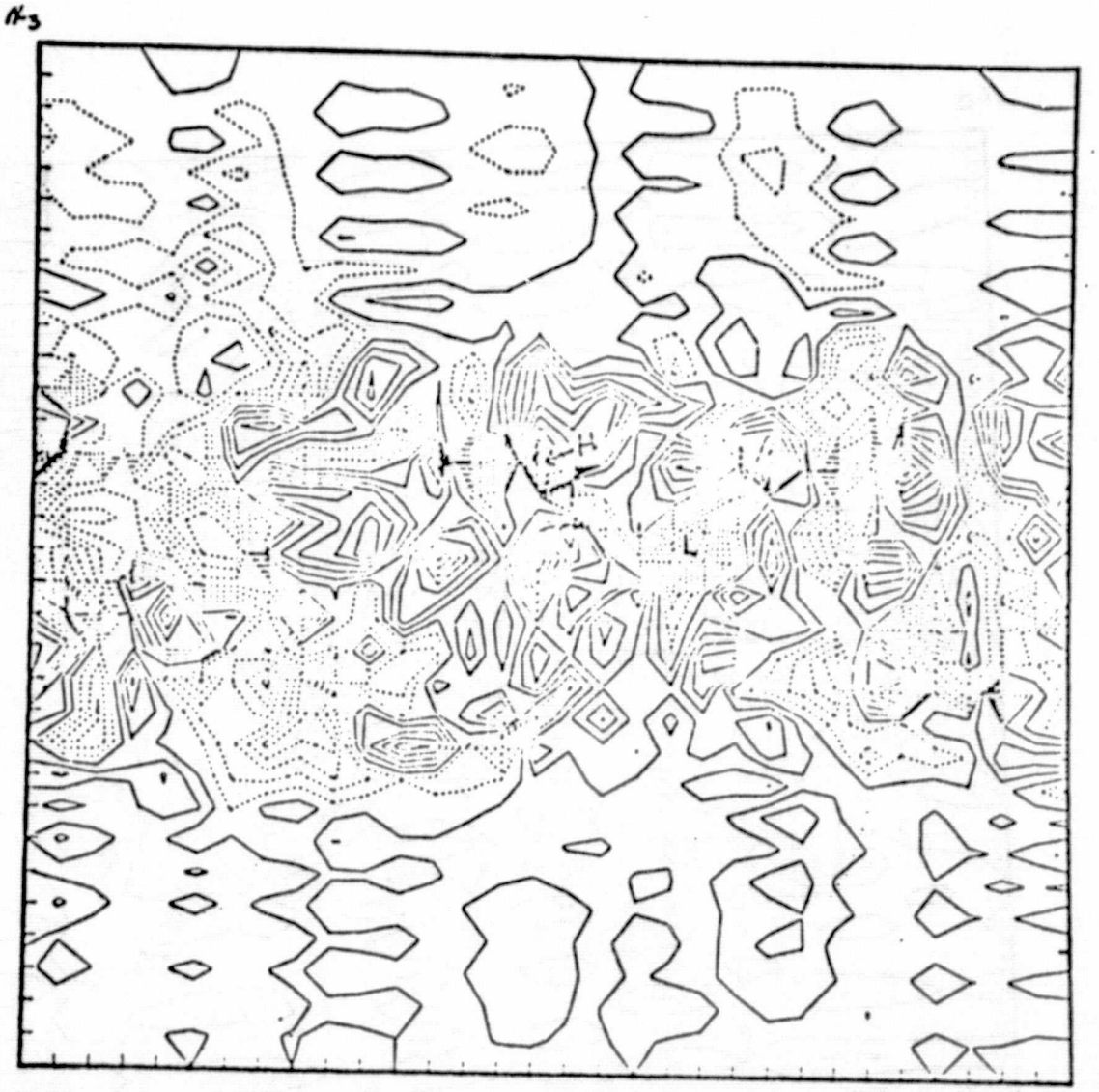

FIG. 18 - Same as Fig. 3 except the contours are for v_3 in the plane $x_2=\frac{1}{2}L$. Here t=.051, $\bar{X}$=4, v_{min}=-9.(1), v_{max}=1.1(2), Δv=1.(1).

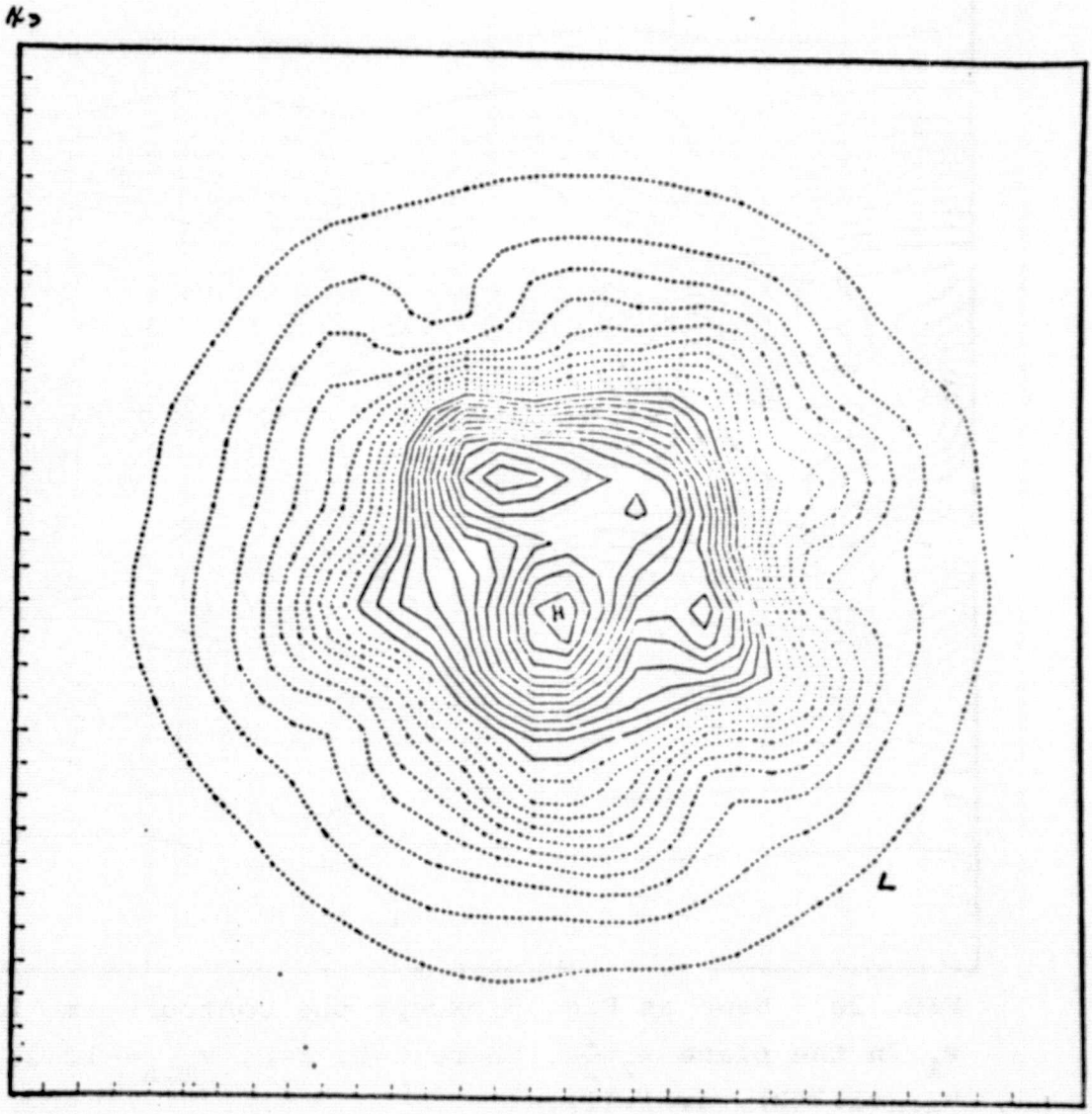

FIG. 19 - Same as Fig. 3 except the contours are for v_1 in the plane $x_1=\frac{1}{2}L$. Here $t=0$, $\overline{X}=8$, $v_{min}=-1.(2)$, $v_{max}=1.1(2)$, $\Delta v=1.(1)$.

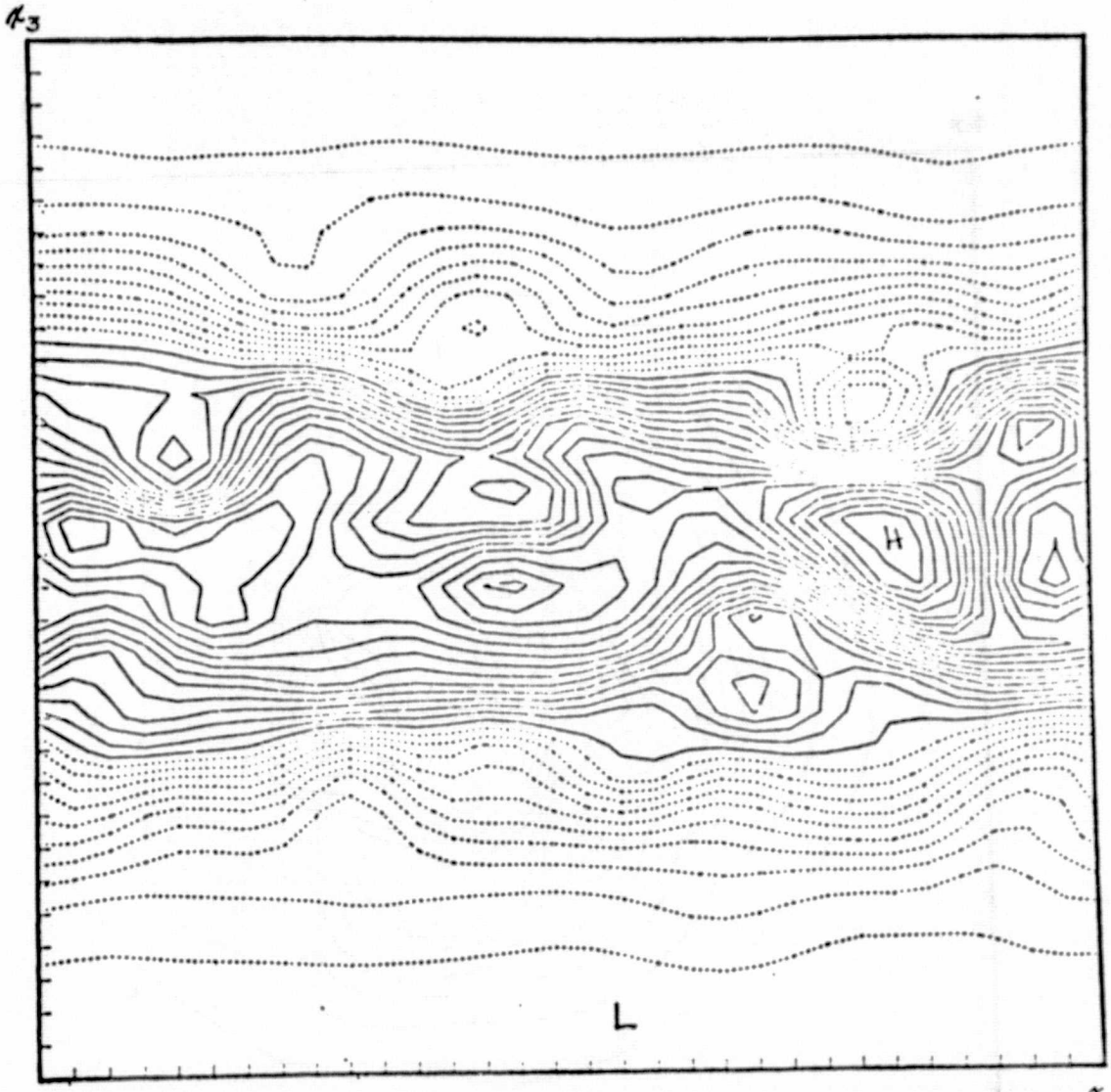

FIG. 20 - Same as Fig. 3 except the contours are for v_1 in the plane $x_2=\frac{1}{2}L$. Here t=0, $\overline{X}=8$, $v_{min}=-1.(2)$, $v_{max}=1.7(2)$, $\Delta v=1.(1)$.

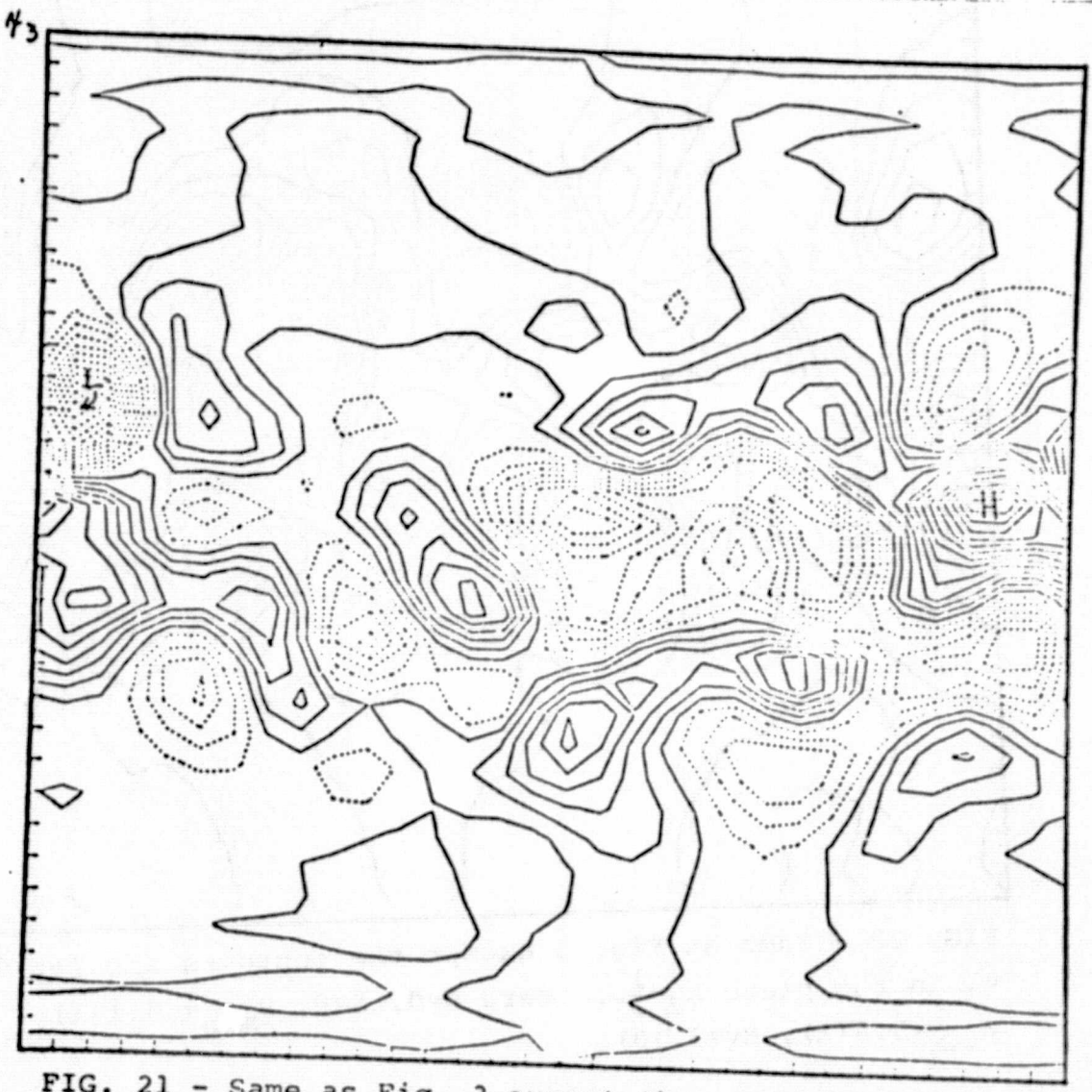

FIG. 21 - Same as Fig. 3 except the contours are for v_2 in the plane $x_2=\frac{1}{2}L$. Here t=0, $\overline{X}=8$, $v_{min}=-1.2(2)$, $v_{max}=1.2(2)$, $\Delta v=1.(1)$.

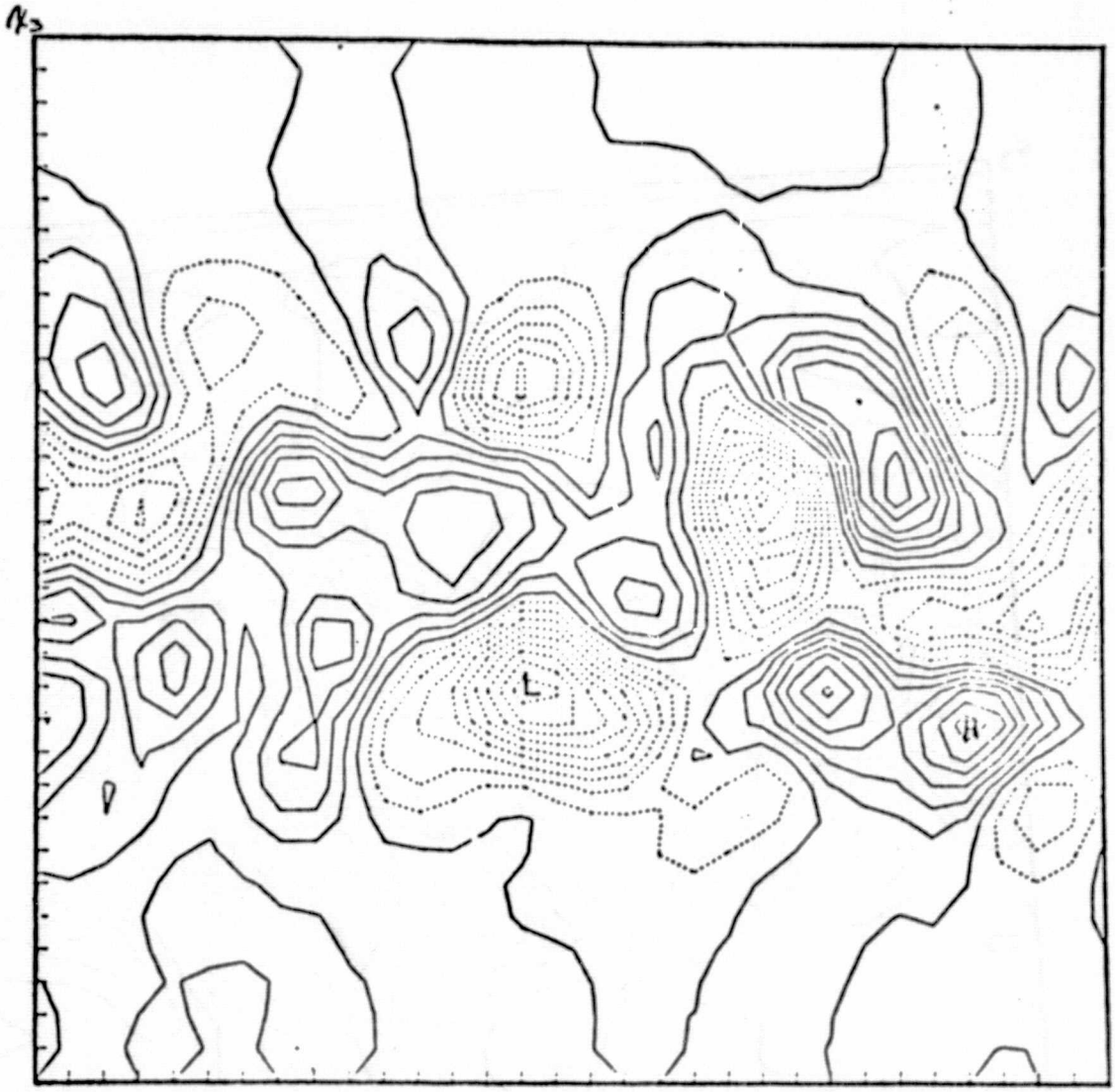

FIG. 22 - Same as Fig. 3 except the contours are for v_3 in the plane $x_2=\frac{1}{2}L$. Here t=0, $\overline{X}=8$, $v_{min}=-8.1(1)$, $v_{max}=5.4(1)$, $\Delta v=9.(0)$.

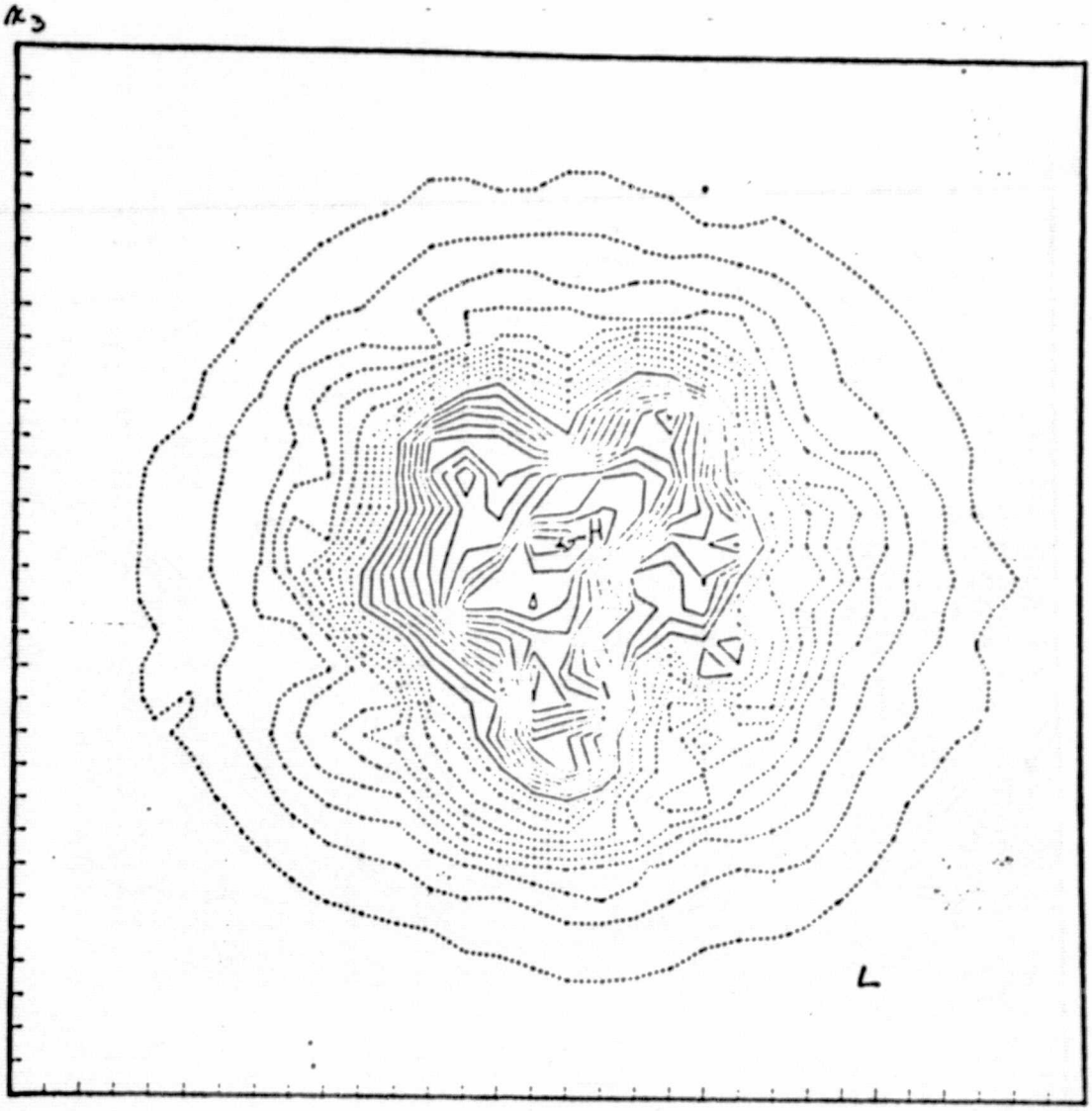

FIG. 23 - Same as Fig. 3 except the contours are for v_1 in the plane $x_1=\frac{1}{2}L$. Here t=.020, $\overline{X}$=8, v_{min}=-1.(2), v_{max}=1.3(2), Δv=1.(1).

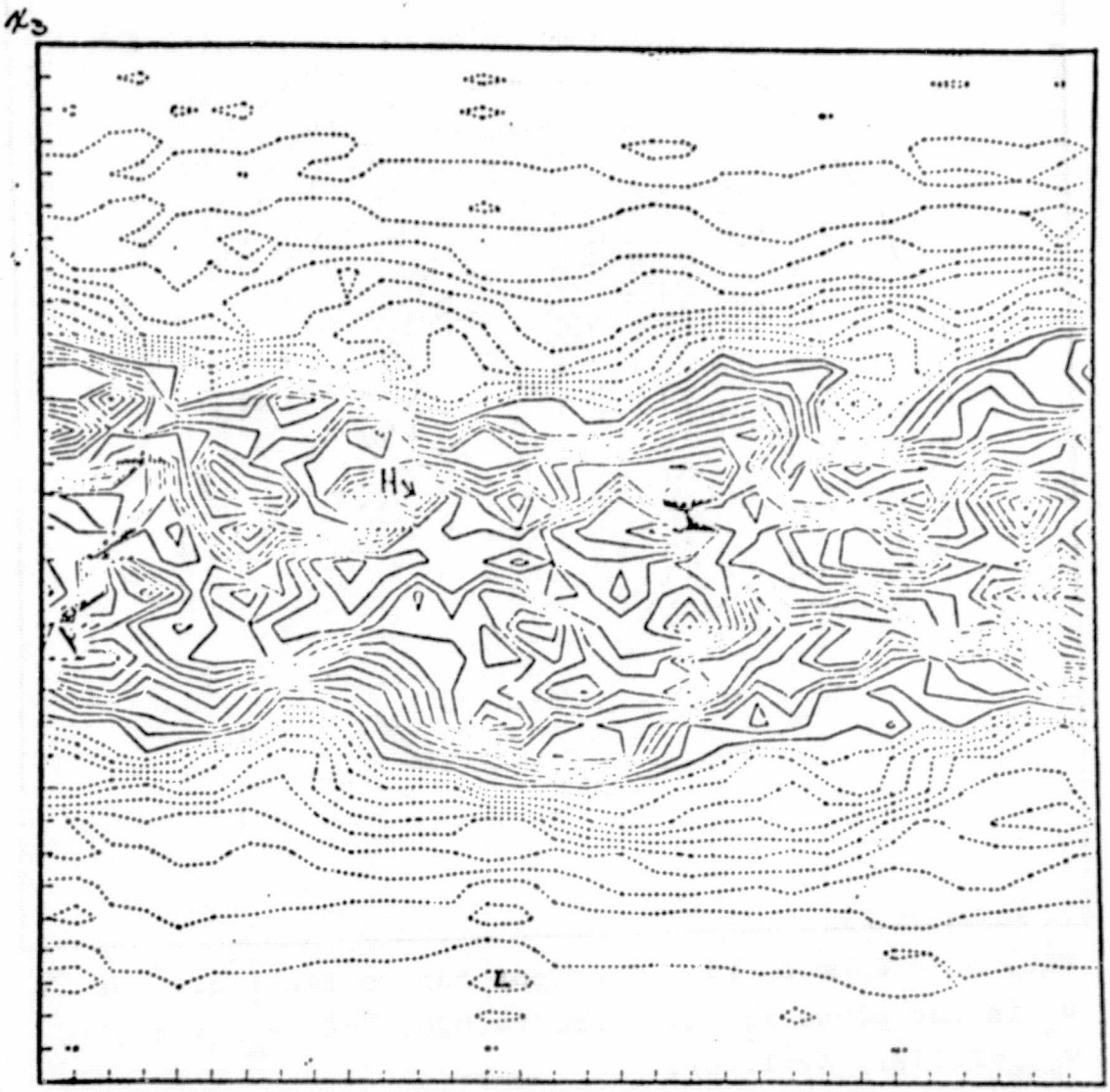

FIG. 24 - Same as Fig. 3 except the contours are for x_1, v_1 in the plane $x_2=\frac{1}{2}L$. Here t=.020, $\overline{X}$=8, v_{min}=-1.1(2), v_{max}=1.9(2), Δv=1.(1).

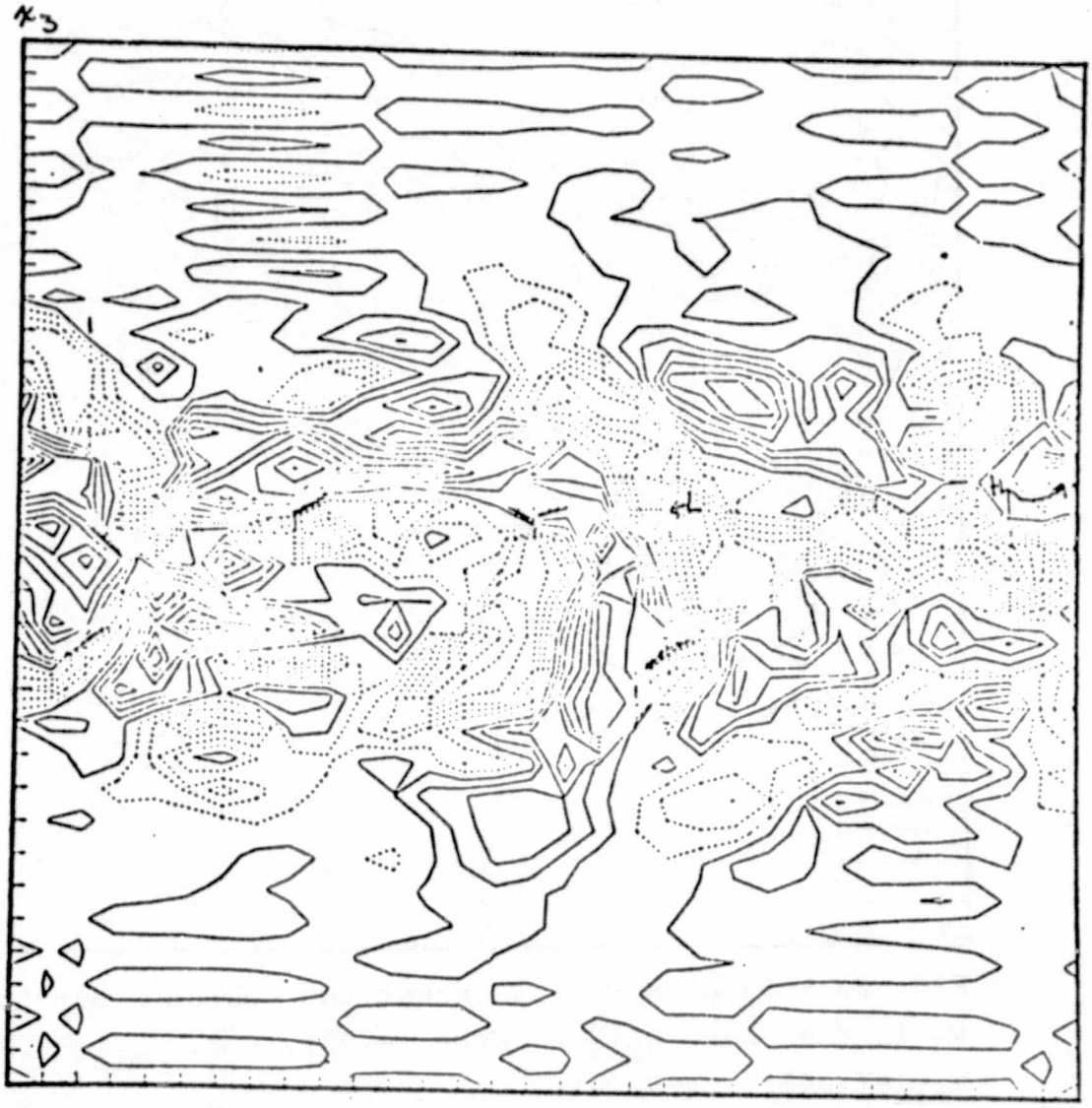

FIG. 25 - Same as Fig. 3 except the contours are for v_2 in the plane $x_2=\frac{1}{2}L$. Here t=.020, $\overline{X}$=8, v_{min}=-1.1(2), v_{max}=1.(2), Δv=1.(1).

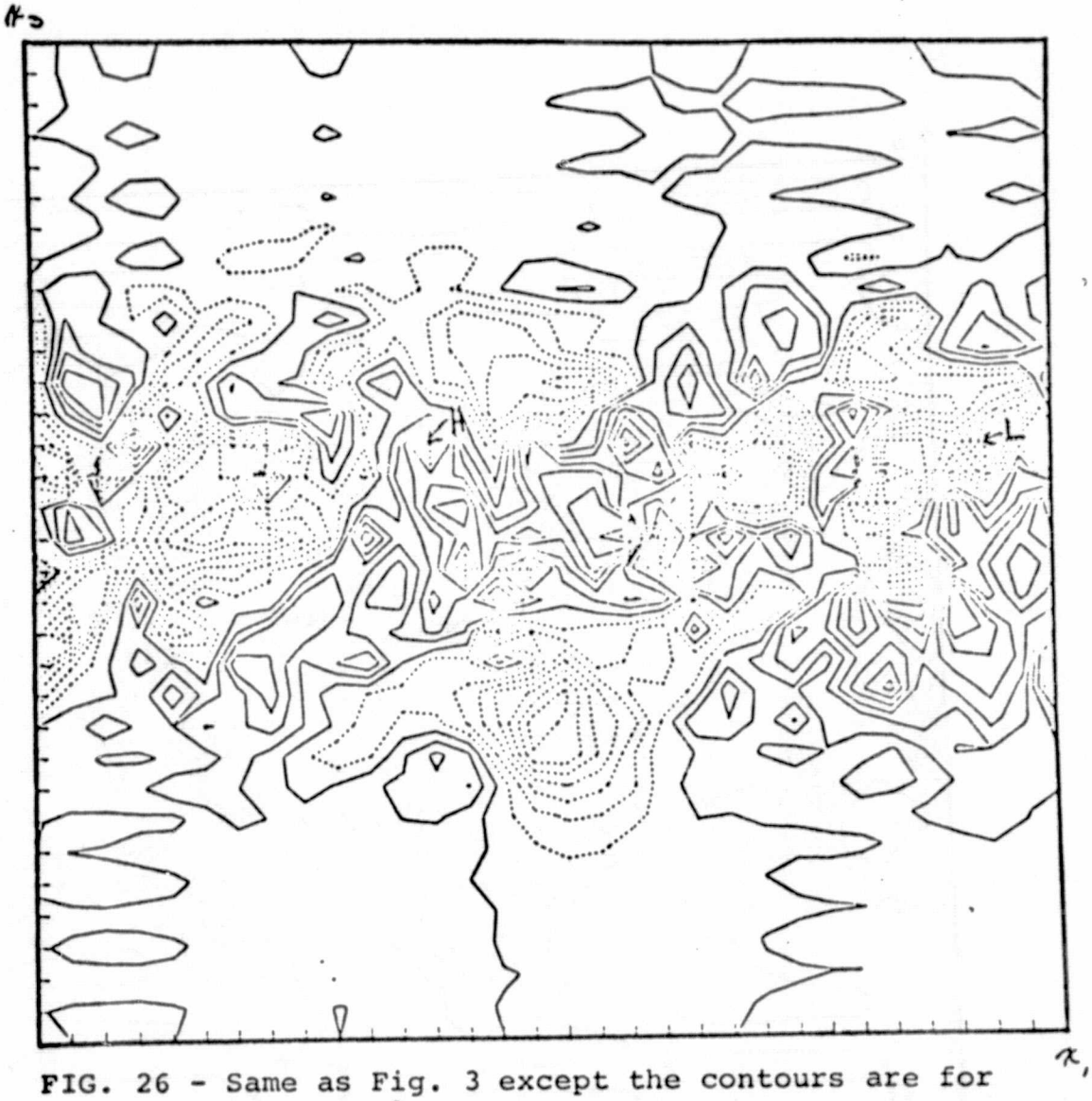

FIG. 26 - Same as Fig. 3 except the contours are for v_3 in the plane $x_2=\frac{1}{2}L$. Here t=.020, $\overline{X}$=8, v_{min}=-7.2(1), v_{max}=7.2(1), Δv=9.(0).

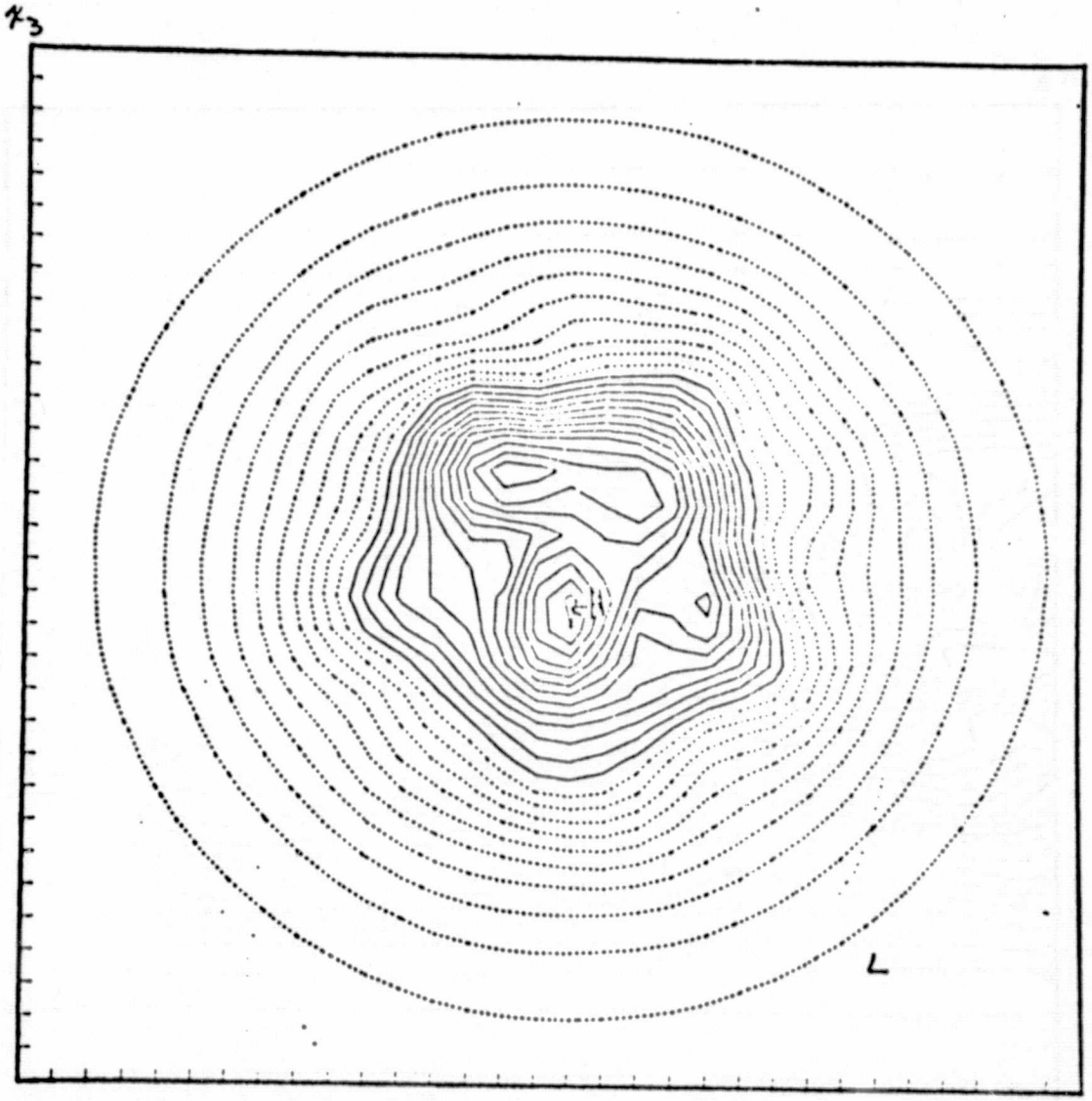

FIG. 27 - Same as Fig. 3 except the contours are for x_2 v_1 in the plane $x_1=\frac{1}{2}L$. Here t=0, $\overline{X}$=12, v_{min}=-1.(2), v_{max}=1.2(2), Δv=1.(1).

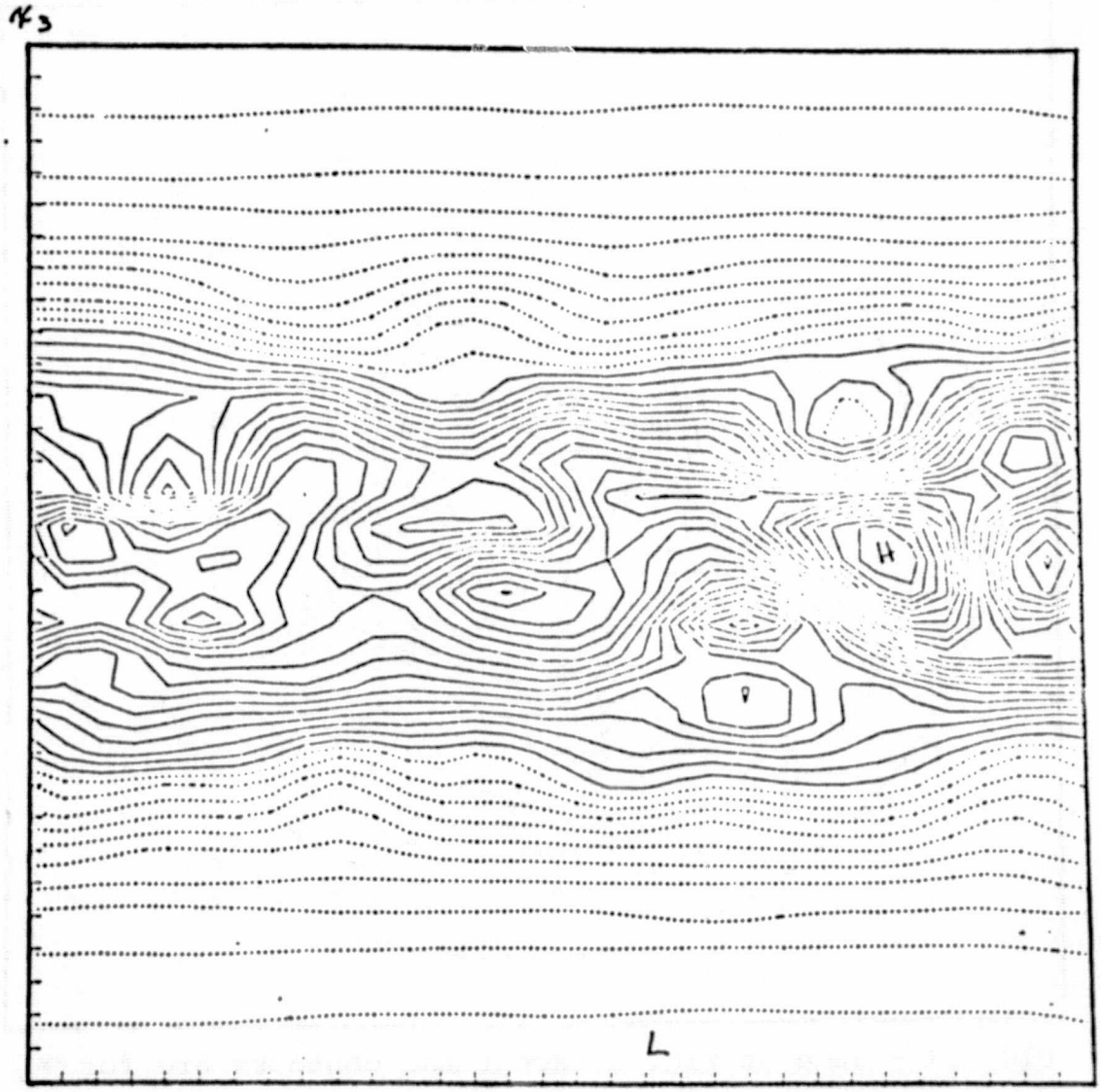

FIG. 28 - Same as Fig. 3 except the contours are for v_1 in the plane $x_2=\frac{1}{2}L$. Here t=0, $\overline{X}$=12, v_{min}=-1.(2), v_{max}=1.9(2), Δv=1.(1).

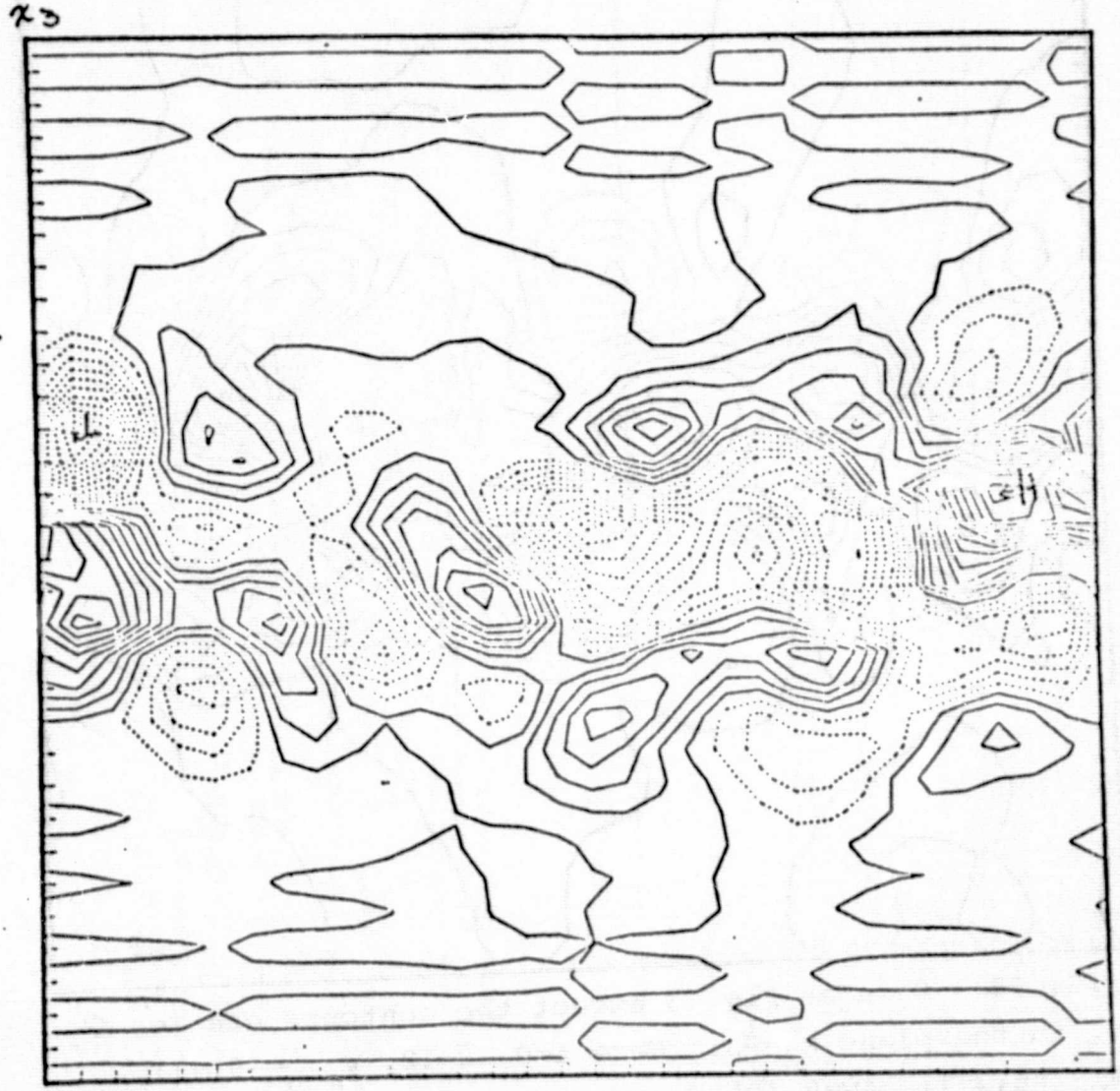

FIG. 29 - Same as Fig. 3 except the contours are for v_1 v_2 in the plane $x_2=\frac{1}{2}L$. Here t=0, $\overline{X}$=12, v_{min}=-1.2(2), v_{max}=1.3(2), Δv=1.(1).

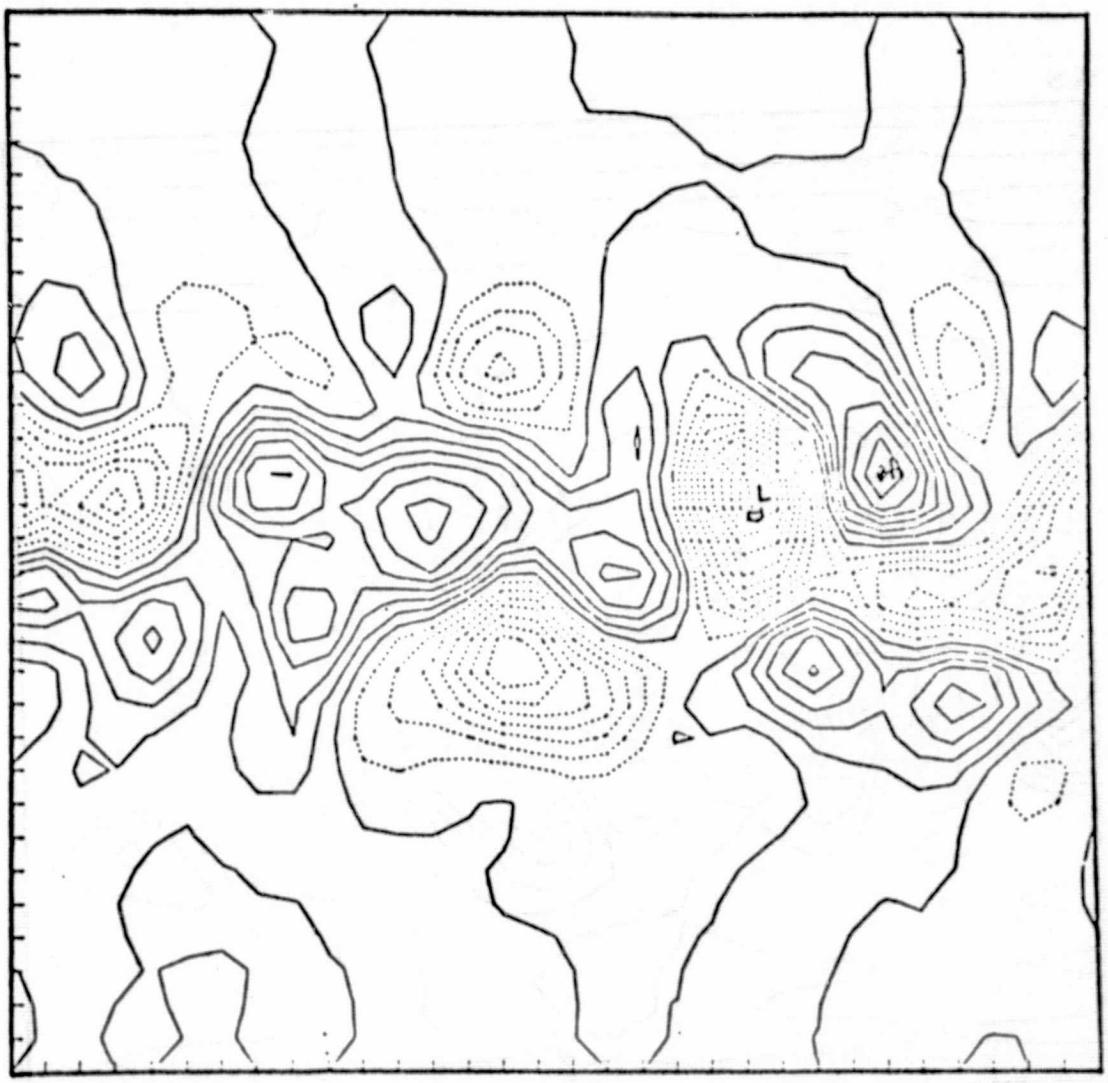

FIG. 30 - Same as Fig. 3 except the contours are for v_3 in the plane $x_2=\frac{1}{2}L$. Here $t=0$, $\overline{X}=12$, $v_{min}=-9.(1)$, $v_{max}=6.3(1)$, $\Delta v=9.(0)$.

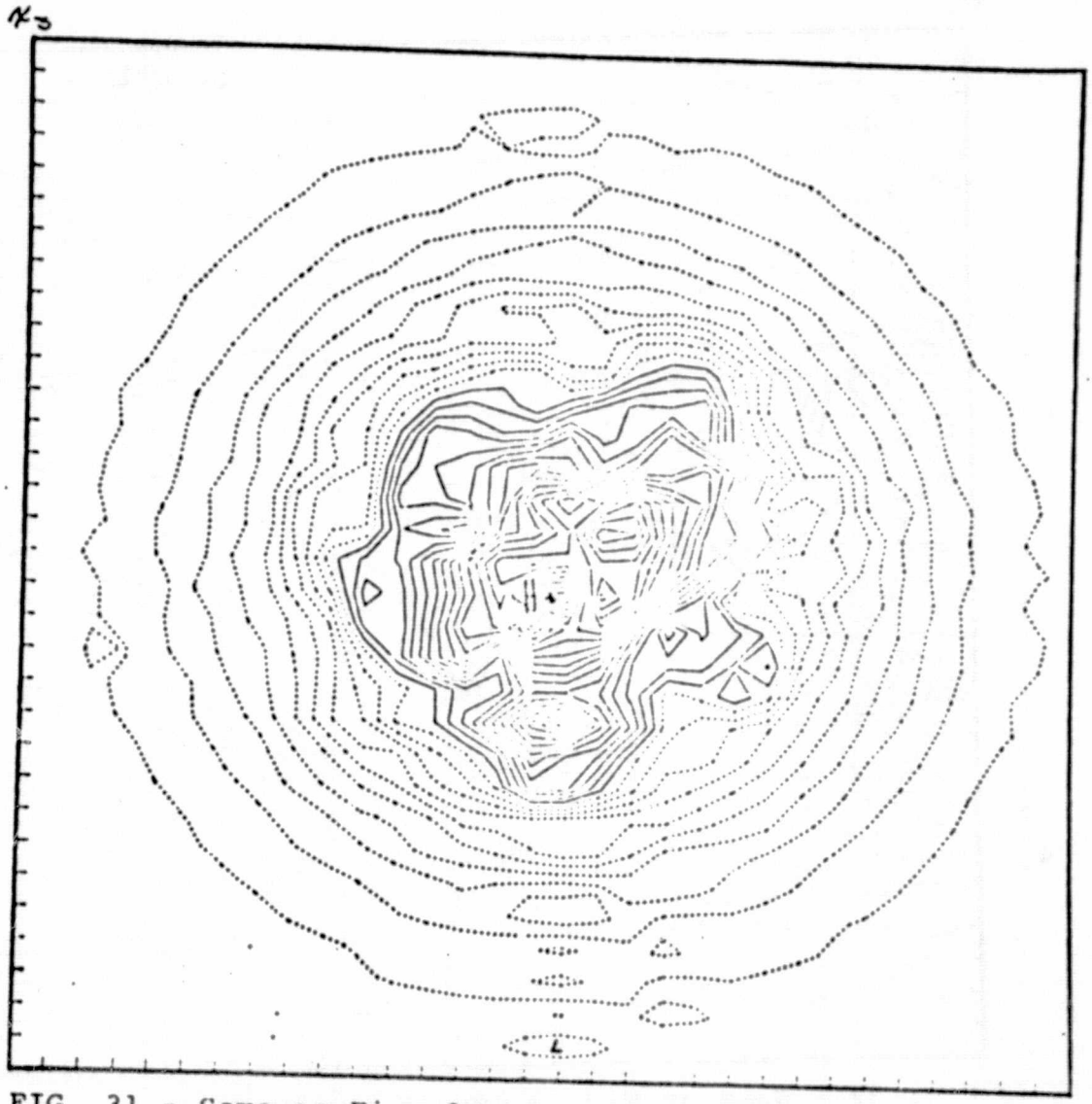

FIG. 31 - Same as Fig. 3 except the contours are for v_1 in the plane $x_1=\frac{1}{2}L$. Here $t=.032$, $\overline{X}=12$, $v_{min}=-1.1(2)$, $v_{max}=1.6(2)$, $\Delta v=1.(1)$.

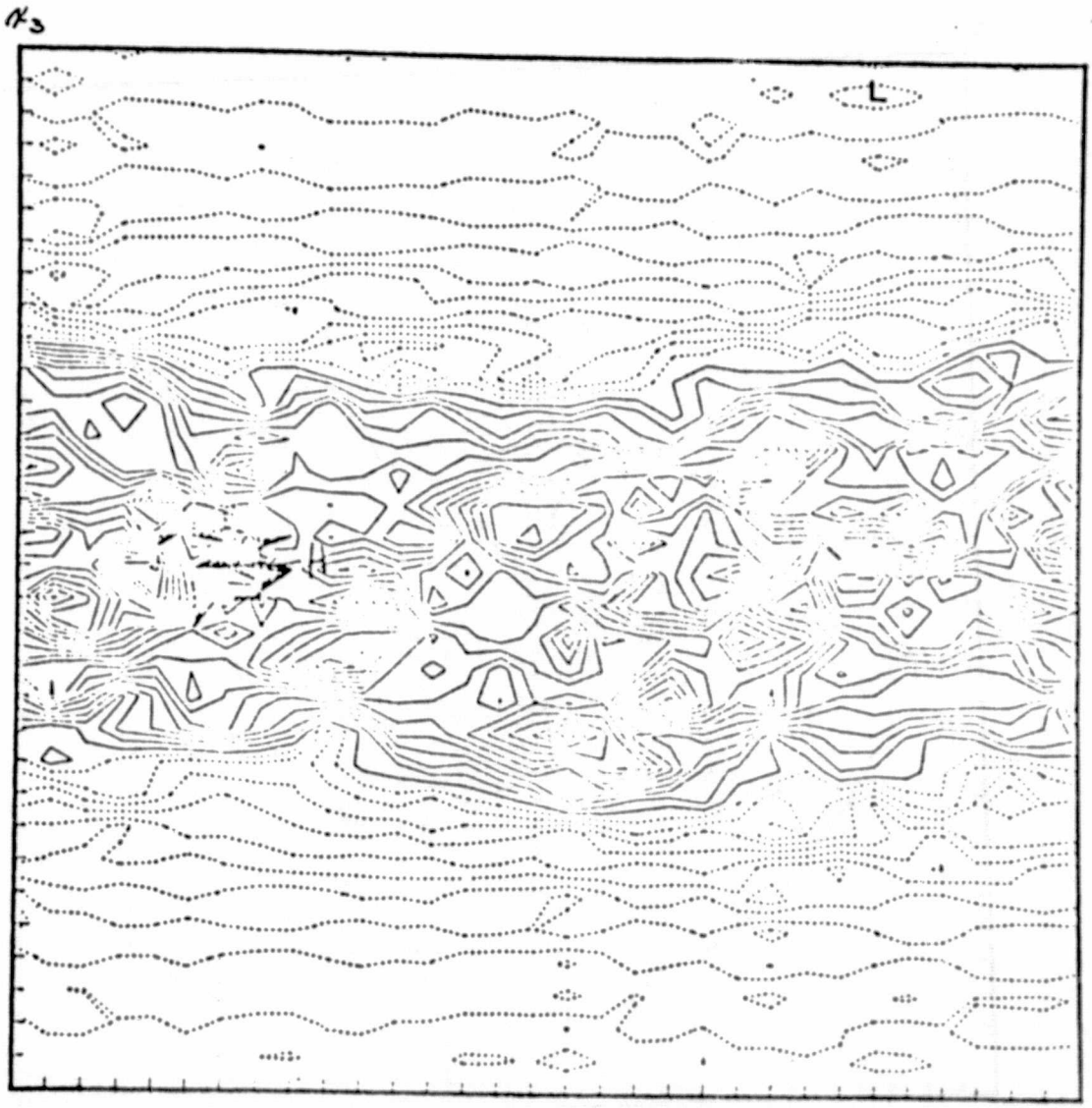

FIG. 32 - Same as Fig. 3 except the contours are for x_1 v_1 in the plane $x_2=\frac{1}{2}L$. Here t=.032, $\overline{X}$=12, v_{min}=-1.1(2), v_{max}=2.(2), Δv=1.(1).

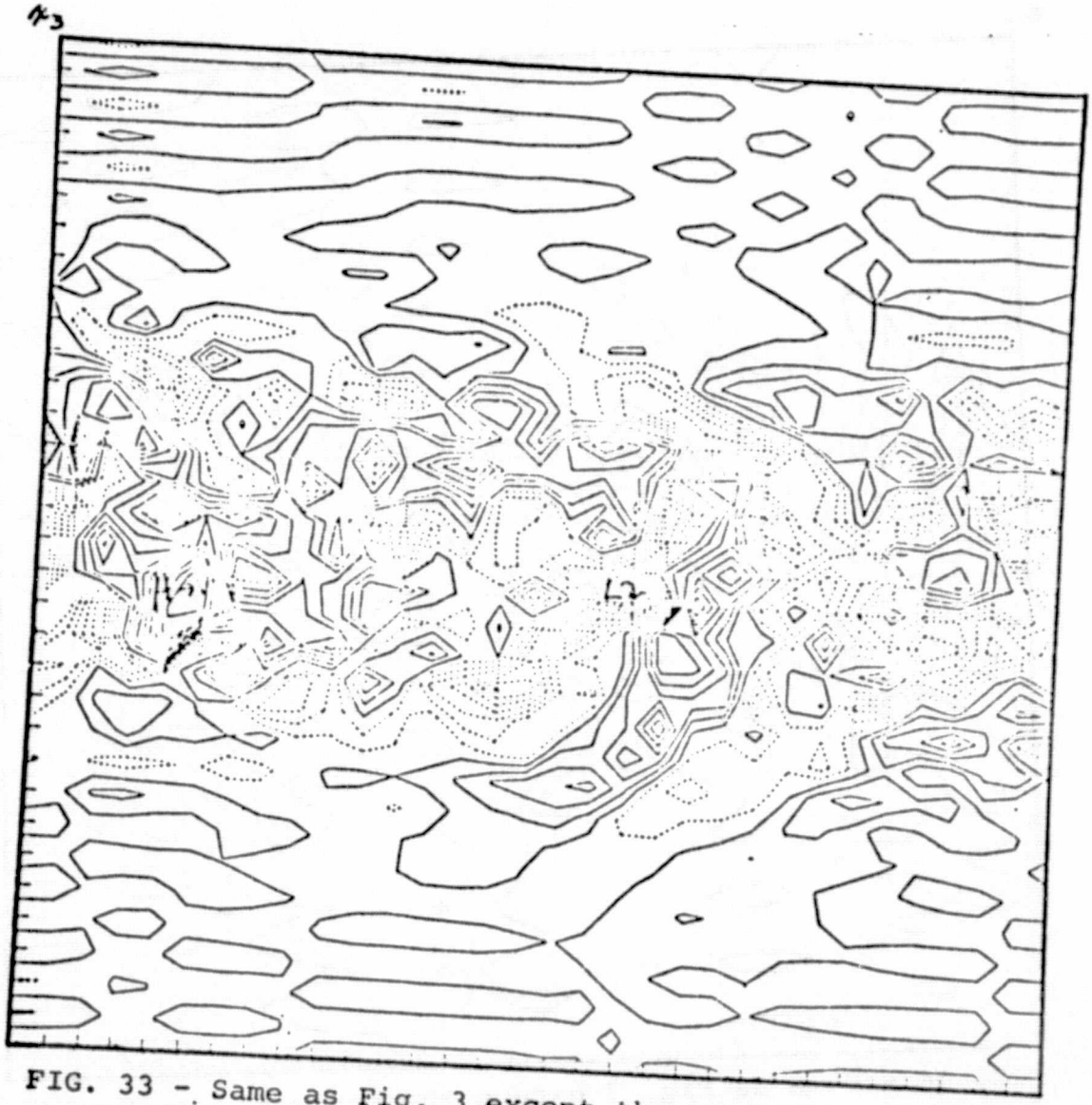

FIG. 33 - Same as Fig. 3 except the contours are for v_2 in the plane $x_2=\frac{1}{2}L$. Here t=.032, $\bar{X}$=12, v_{min}=-1.2(2), v_{max}=9.(1), Δv=1.(1).

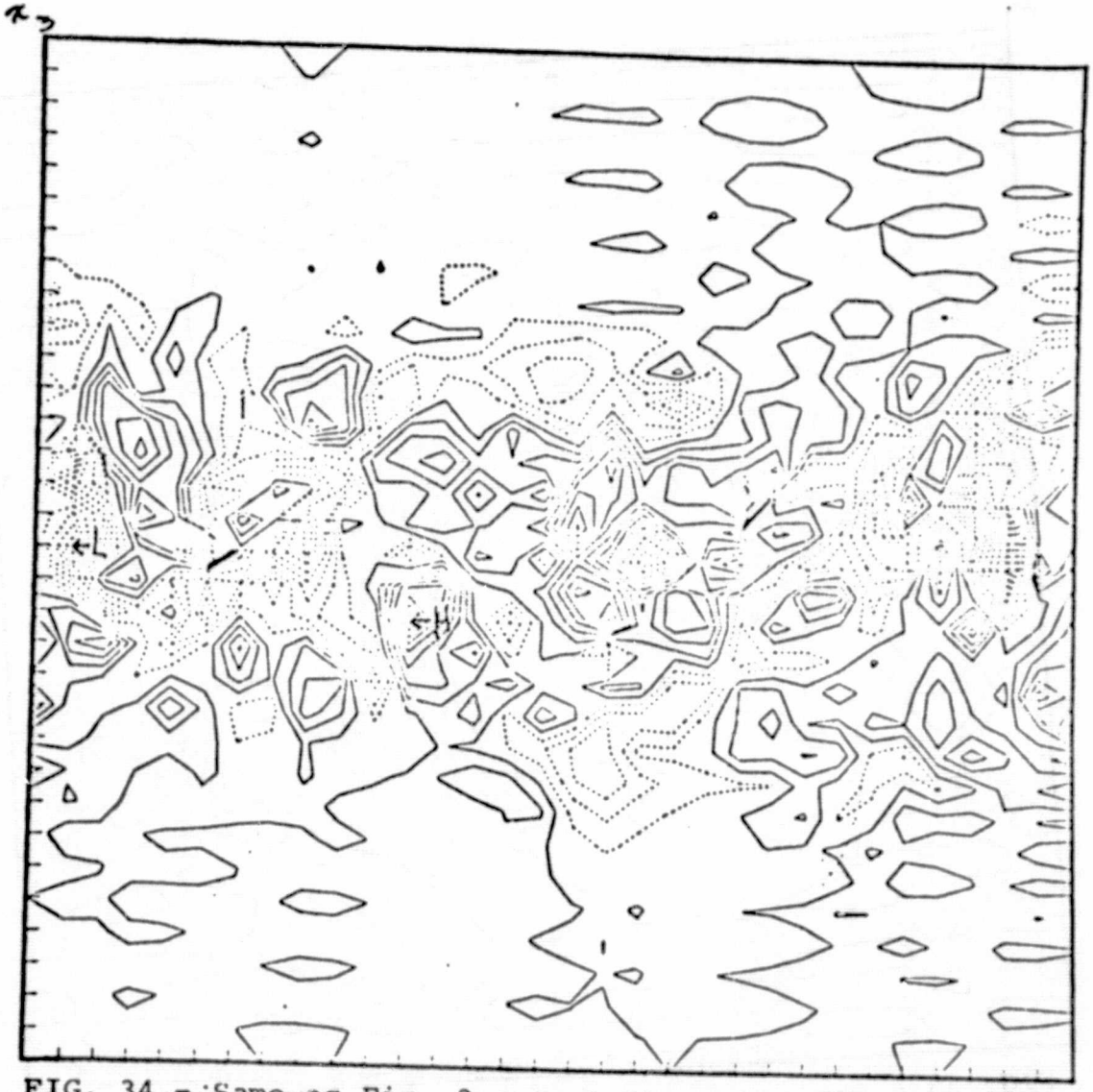

FIG. 34 - Same as Fig. 3 except the contours are for v_3 in the plane $x_2=\frac{1}{2}L$. Here t=.032, $\overline{X}$=12, v_{min}=-1.(2), v_{max}=9.(1), Δv=1.(1).

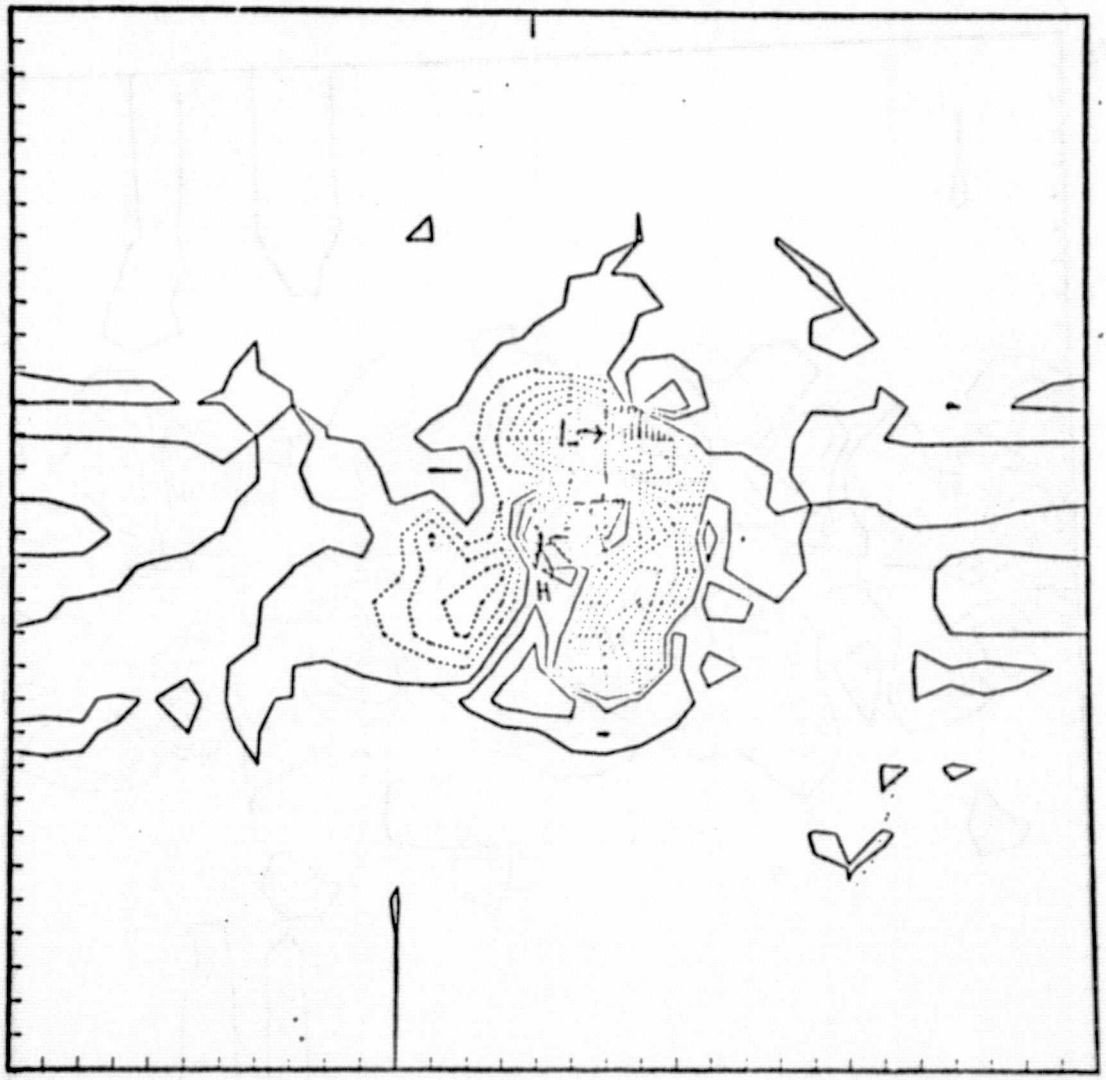

FIG. 35 -- Contour plot of the quadrupole moments in the plane $x_1=\frac{1}{2}L$ at $\overline{X}=4$ diameters downstream from the jet exit. Here t=0, the contour minimum is $Q_{min}=-1.4(5)$, the contour maximum is $Q_{max}=4.(4)$ and the contour interval is $\Delta Q=1.(4)$.

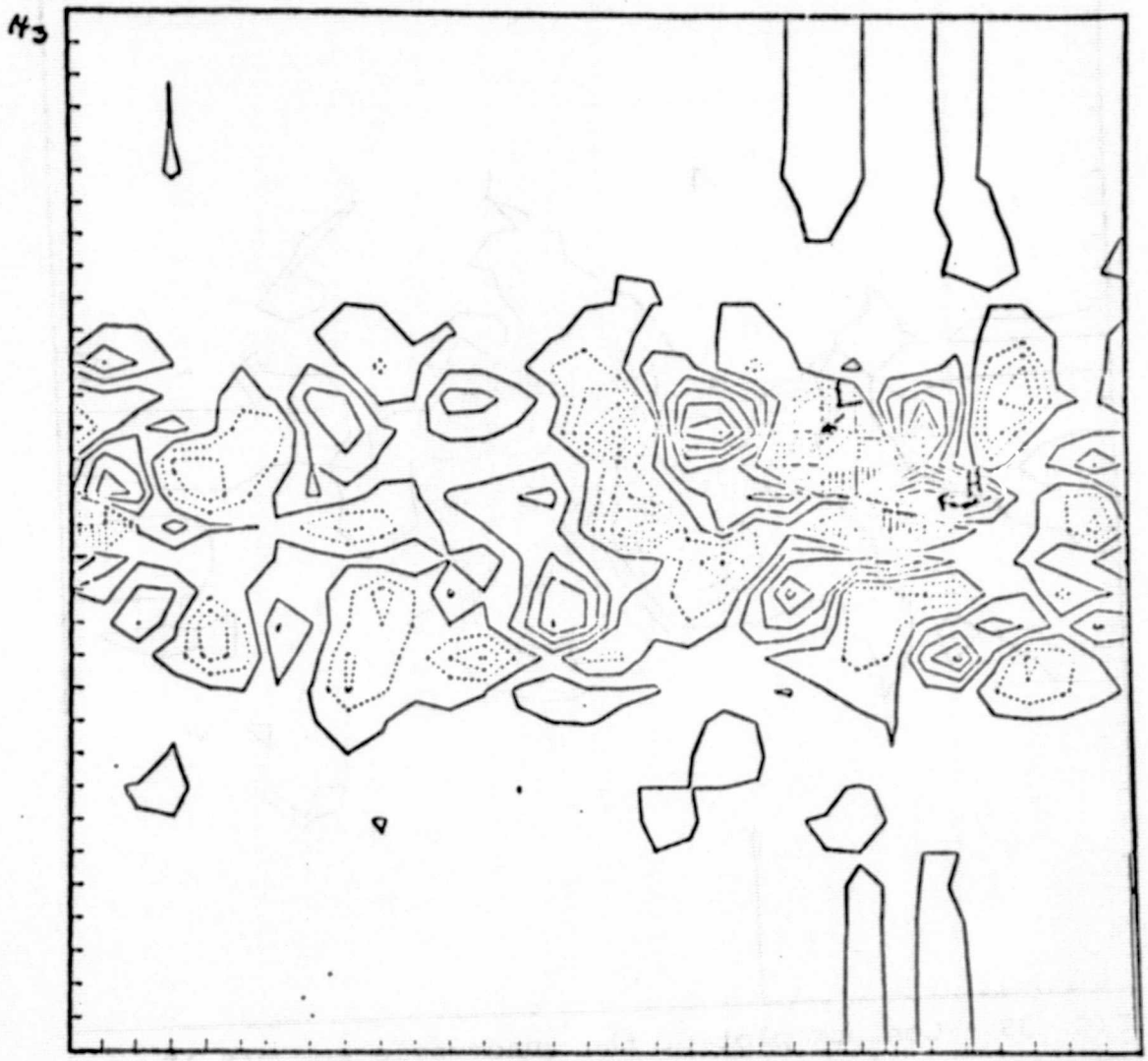

FIG. 36 - Same as Fig. 35 except the contours are made in the plane $x_2=\frac{1}{2}L$ at $\overline{X}=4$. Here t=0, $Q_{min}=-2.4(5)$, $Q_{max}=1.2(5)$, $\Delta Q=2.(4)$.

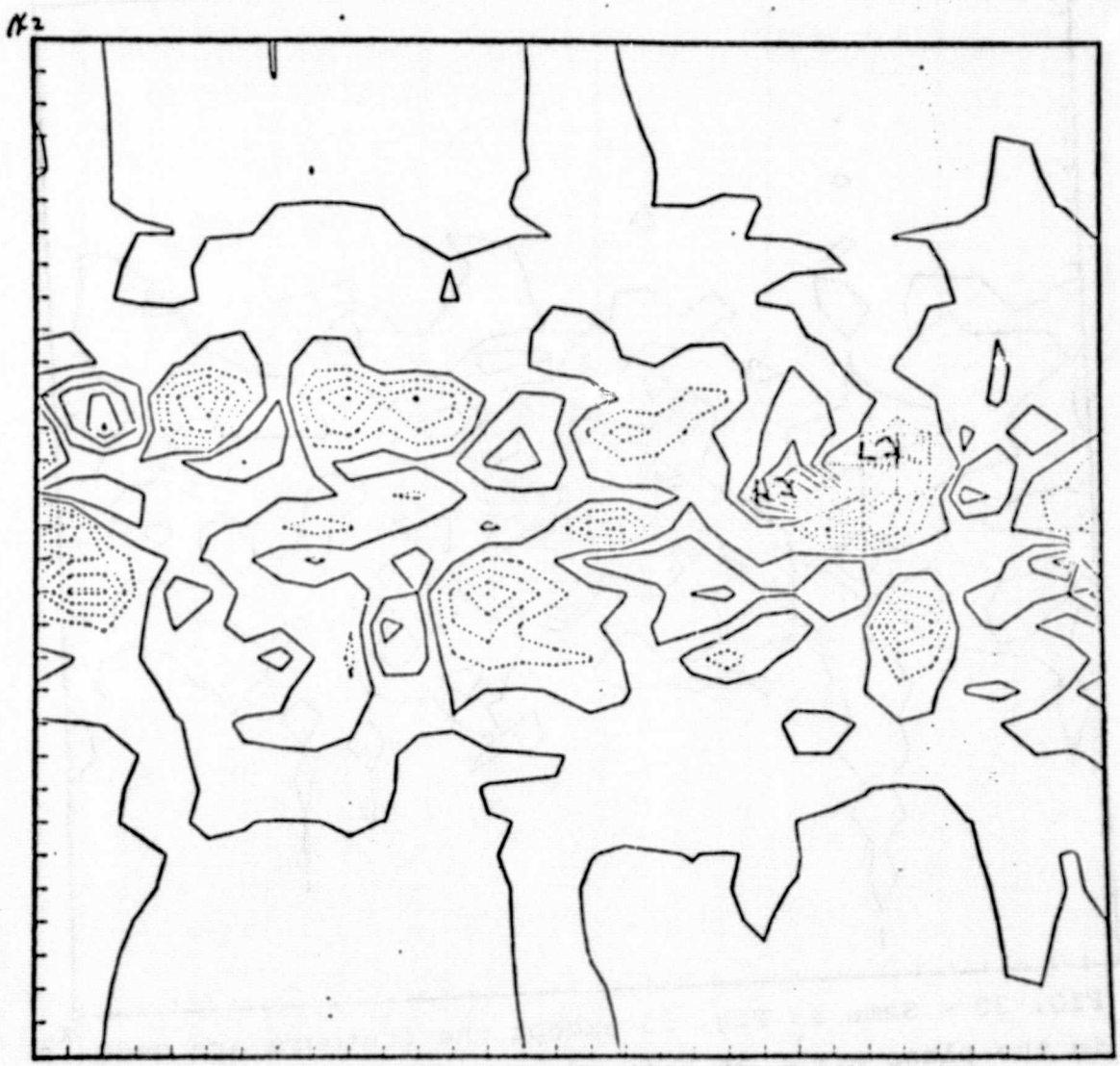

FIG. 37 - Same as Fig. 35 except the contours are made in the plane $x_3=\frac{1}{4}L$ at $\overline{X}=4$. Here $t=0$, $Q_{min}=-3.9(5)$, $Q_{max}=1.5(5)$, $\Delta Q=3.(4)$.

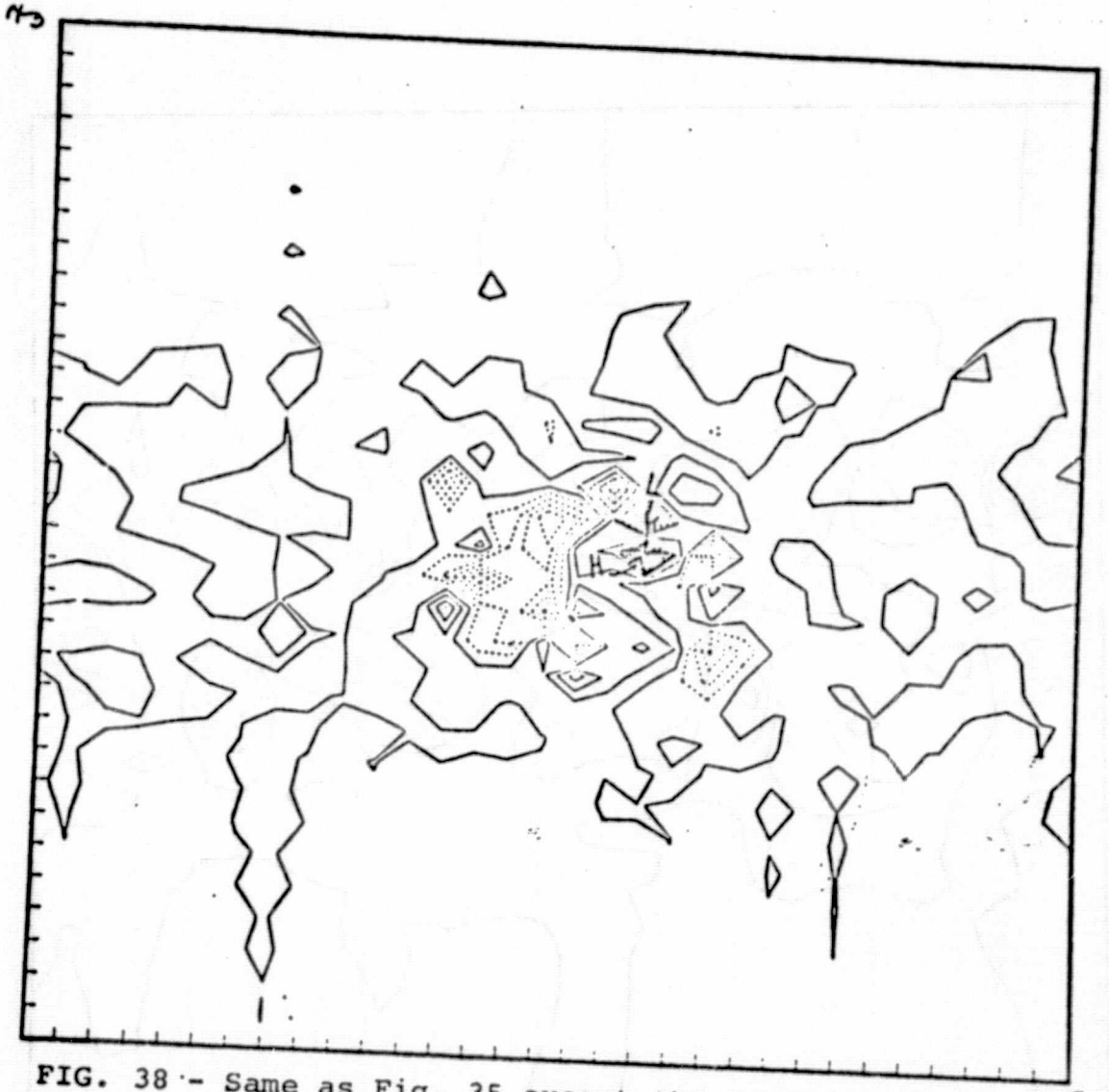

FIG. 38 - Same as Fig. 35 except the contours are made in the plane $x_1=\frac{1}{2}L$ at $\overline{X}=4$. Here t=.020, Q_{min}=-2.4(5), Q_{max}=3.6(5), ΔQ=4.(4).

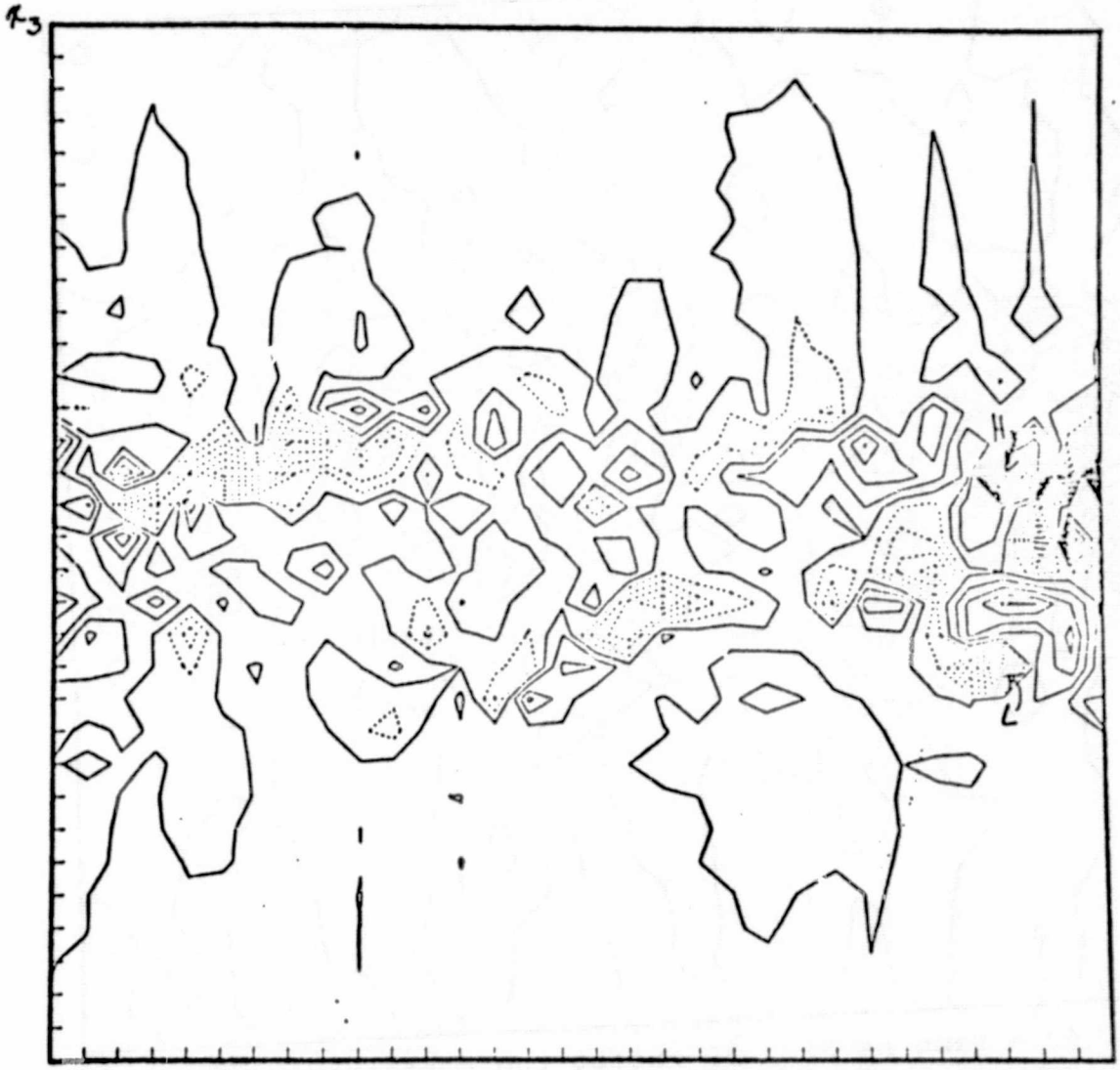

FIG. 39 - Same as Fig. 35 except the contours are made in the plane $x_2=\frac{1}{2}L$ at $\overline{X}=4$. Here $t=.020$, $Q_{min}=-4.9(5)$, $Q_{max}=5.6(5)$, $\Delta Q=7.(4)$.

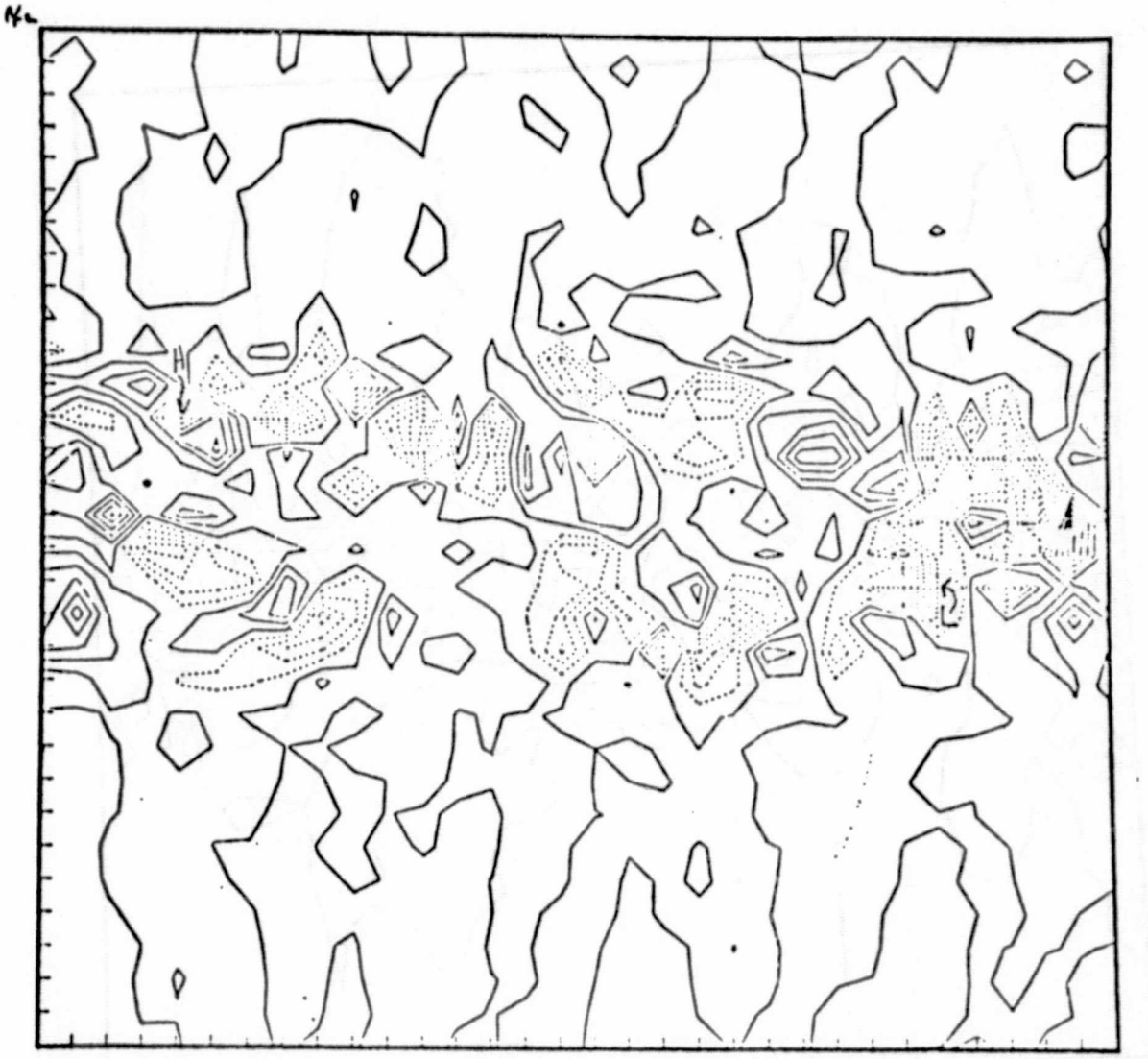

FIG. 40 - Same as Fig. 35 except the contours are made in the plane $x_3=\frac{1}{4}L$ at $\overline{X}=4$. Here t=.020, Q_{min}=-4.5(5), Q_{max}=3.5(5), ΔQ=5.(4).

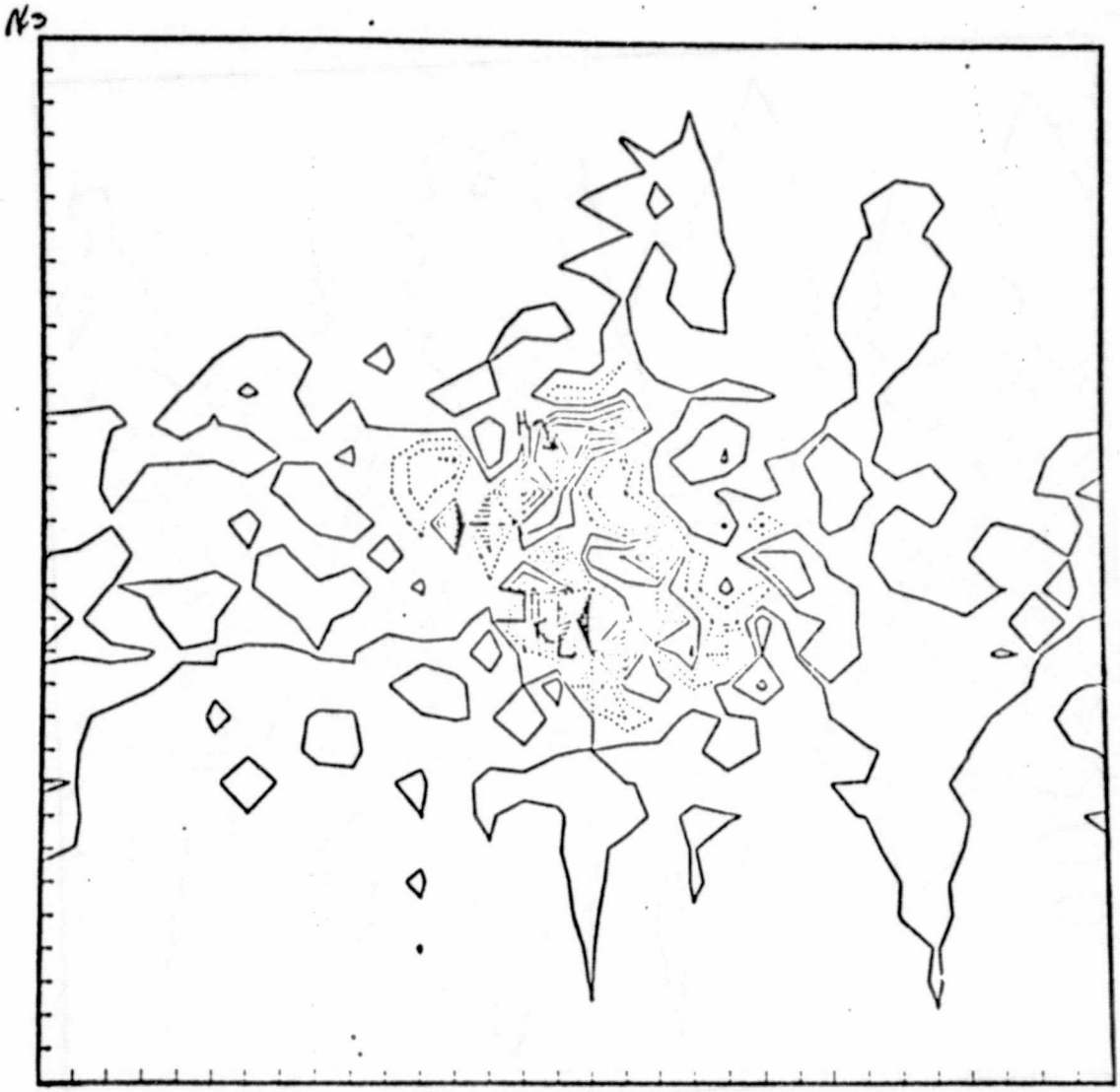

FIG. 41 - Same as Fig. 35 except the contours are made in the plane $x_1=\frac{1}{2}L$ at $\overline{X}=4$. Here $t=.031$, $Q_{min}=-5.(5)$, $Q_{max}=3.(5)$, $\Delta Q=5.(4)$.

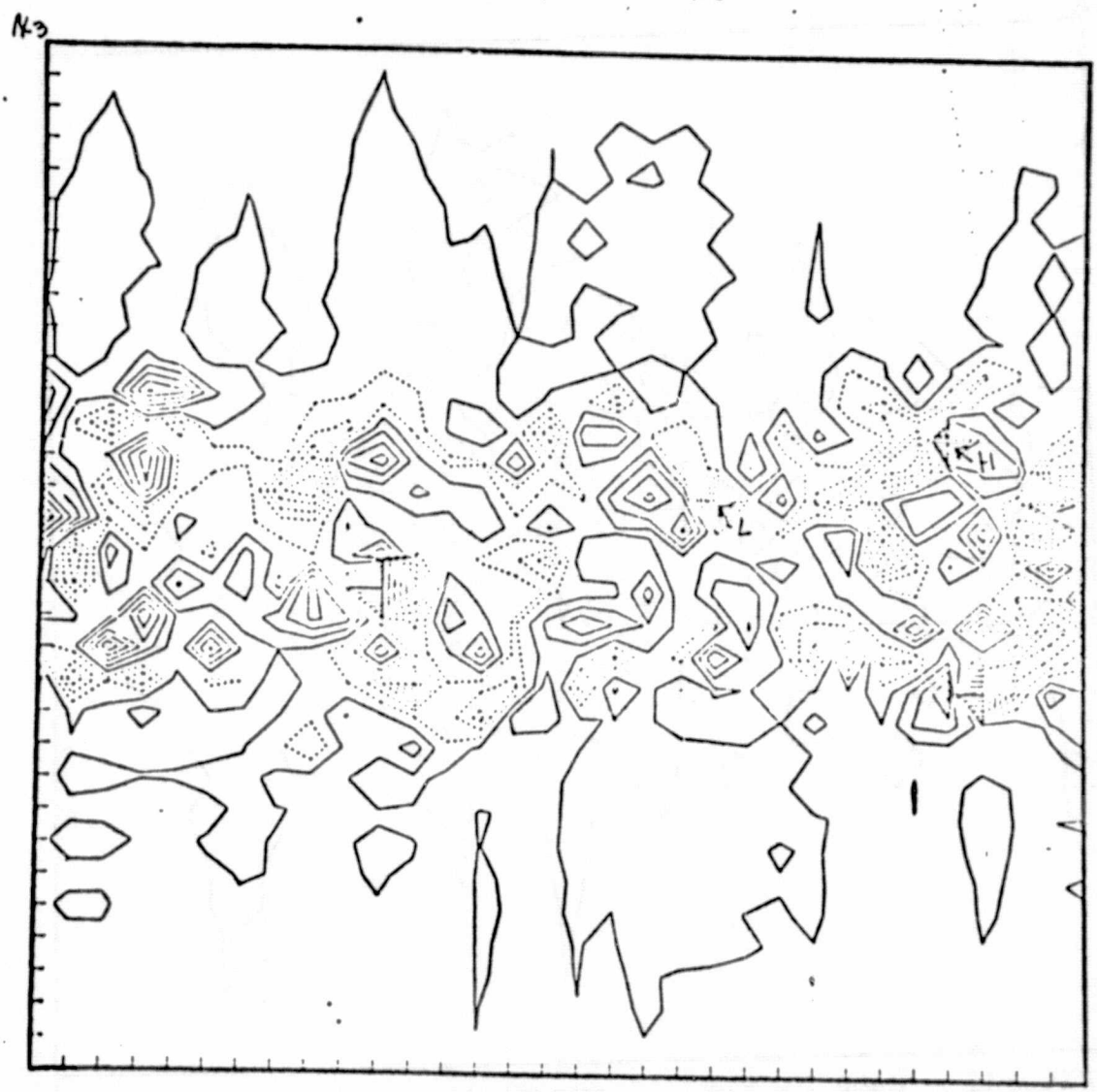

FIG. 42 - Same as Fig. 35 except the contours are made in the plane $x_2=\frac{1}{2}L$ at $\bar{X}=4$. Here t=.031, Q_{min}=-1.5(6), Q_{max}=6.(5), ΔQ=1.(5).

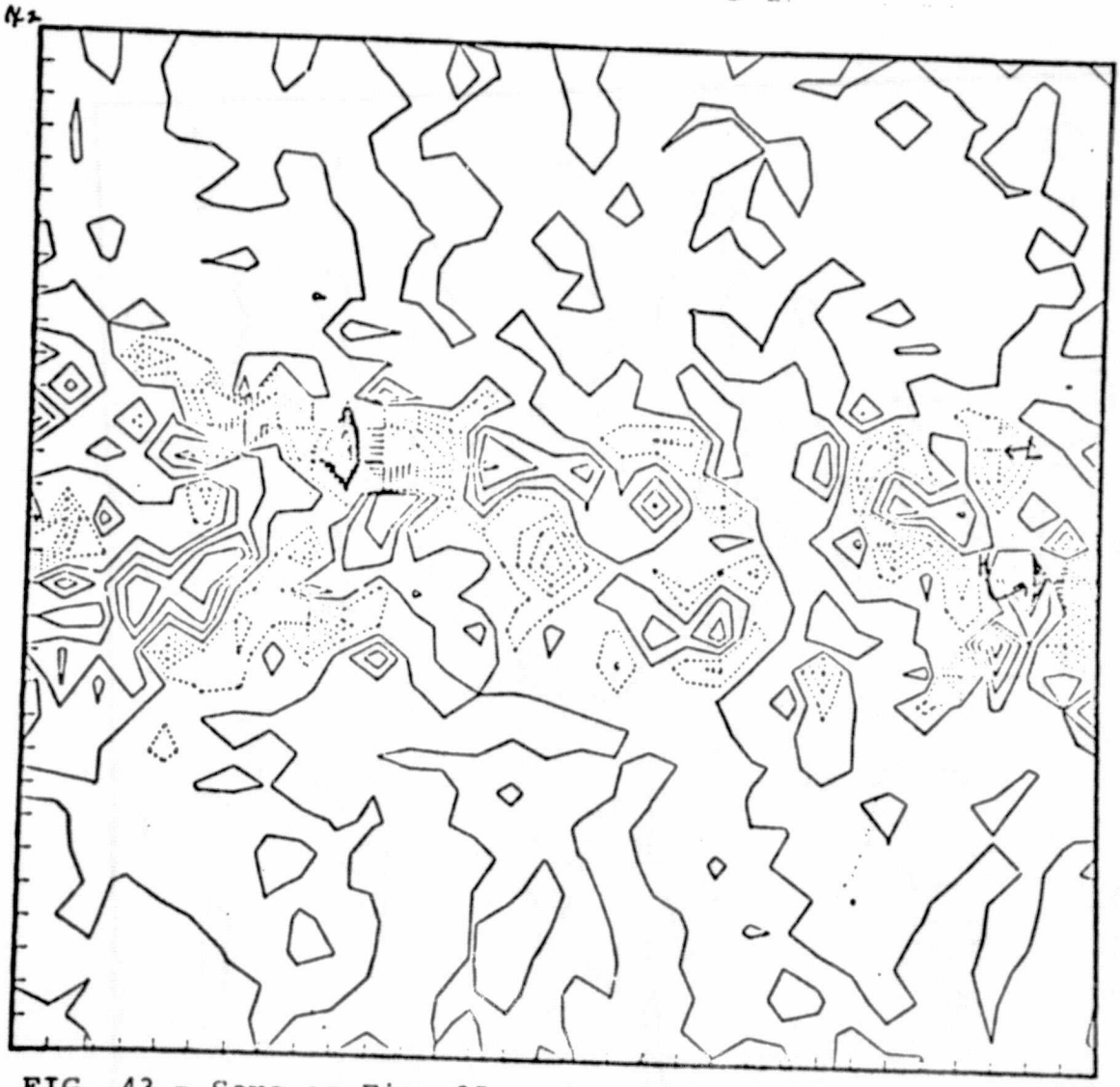

FIG. 43 - Same as Fig. 35 except the contours are made in the plane $x_3=\frac{1}{4}L$ at $\overline{X}=4$. Here $t=.031$, $Q_{min}=-1.2(6)$, $Q_{max}=8.(5)$, $\Delta Q=1.(5)$.

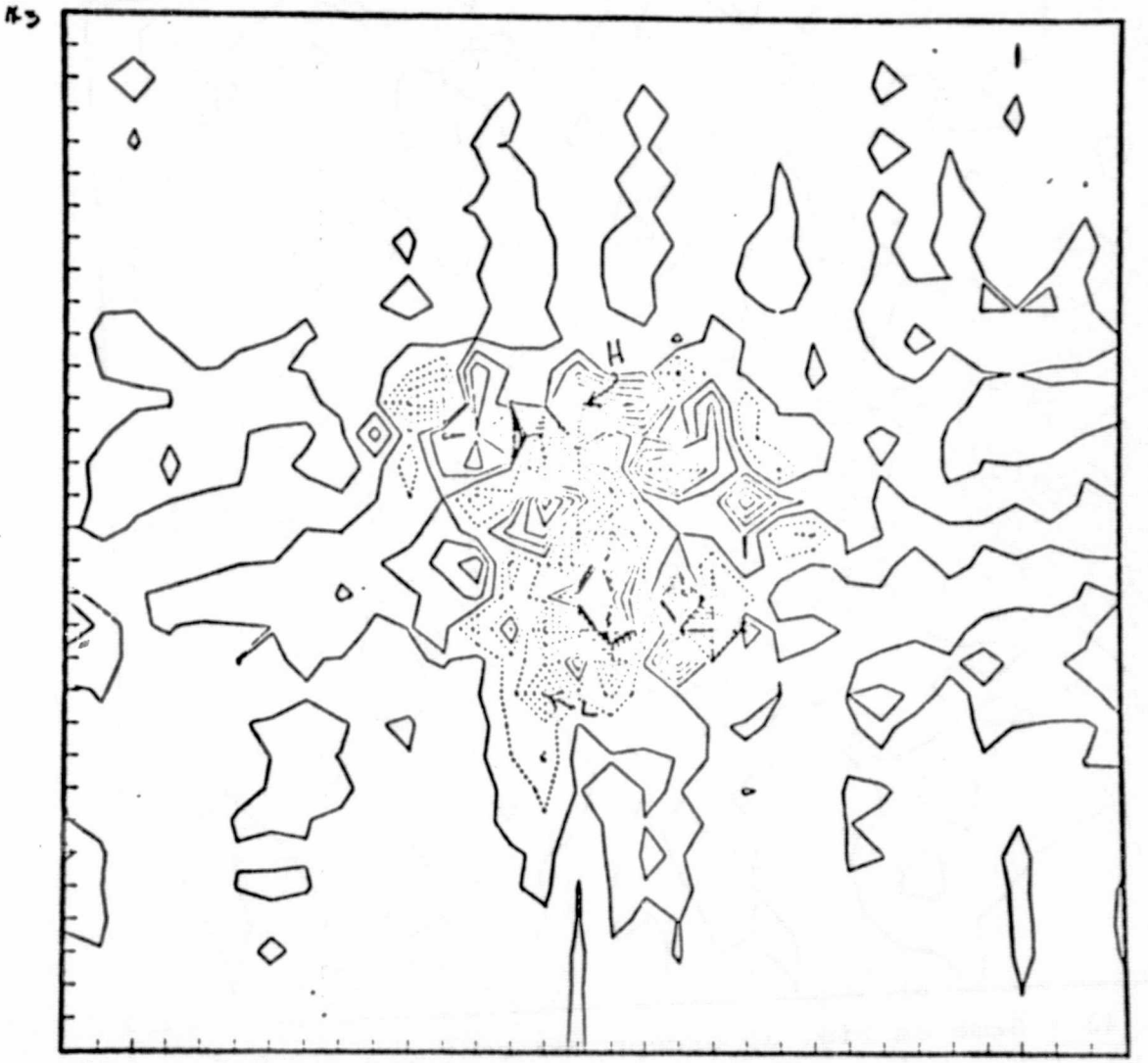

FIG. 44 - Same as Fig. 35 except the contours are made in the plane $x_1=\frac{1}{2}L$ at $\overline{X}=4$. Here t=.051, $Q_{min}=-1.3(6)$, $Q_{max}=8.(5)$, $\Delta Q=1.(5)$.

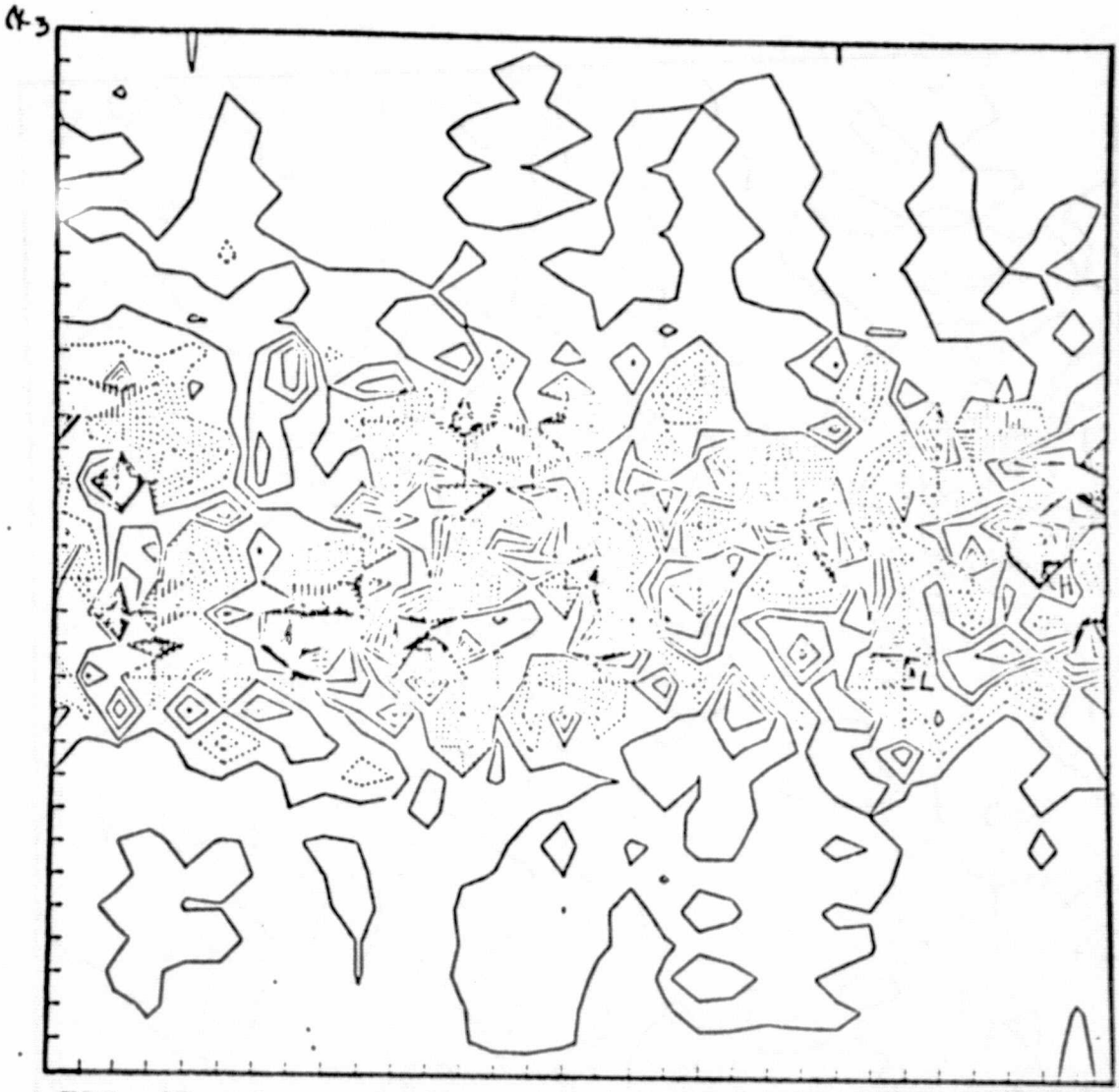

FIG. 45 - Same as Fig. 35 except the contours are made in the plane $x_2=\frac{1}{2}L$ at $\overline{X}=4$. Here $t=.051$, $Q_{min}=-1.2(6)$, $Q_{max}=1.4(6)$, $\Delta Q=1.(5)$.

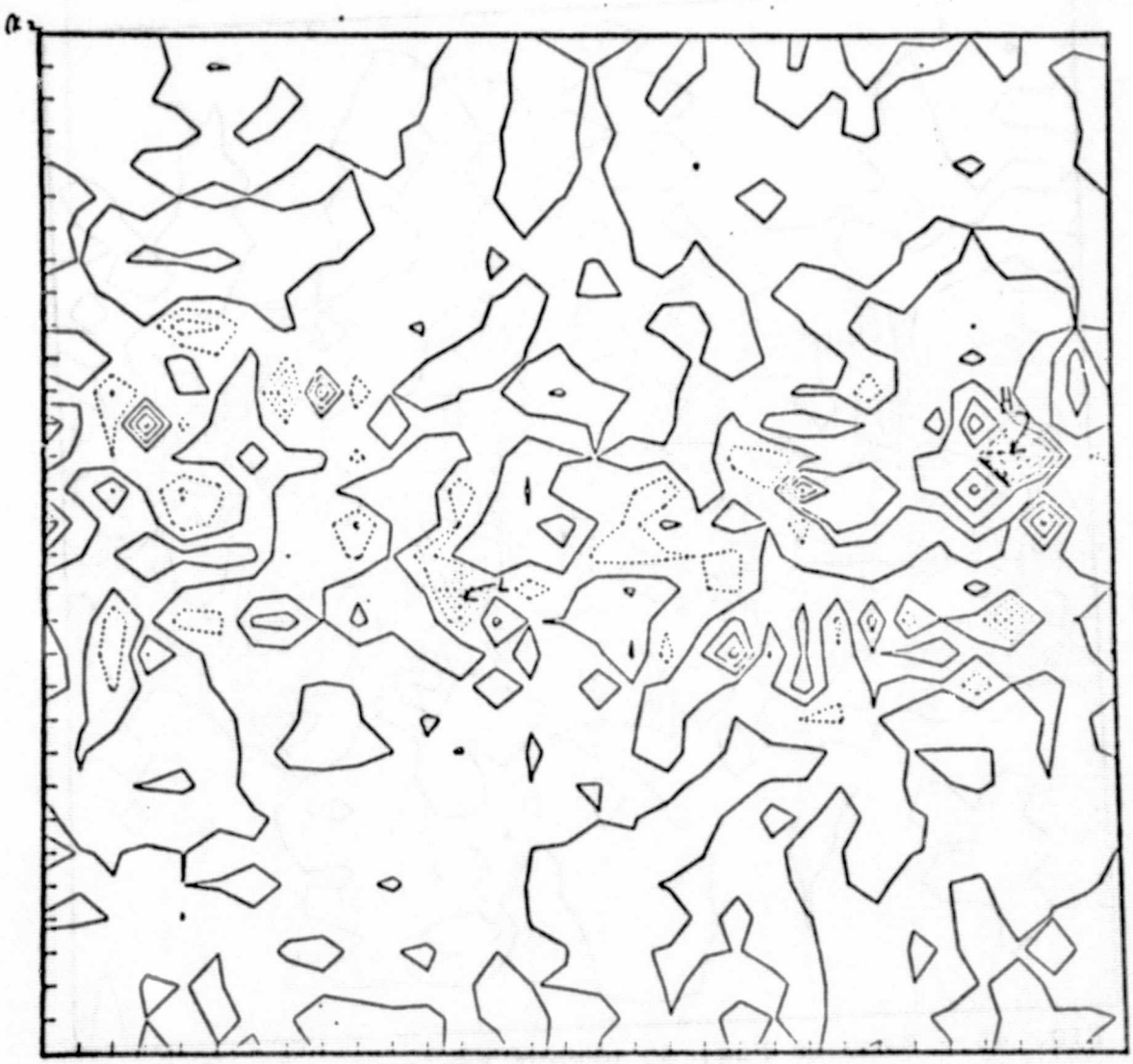

FIG. 46 - Same as Fig. 35 except the contours are made in the plane $x_3=\frac{1}{4}L$ at $\overline{X}=4$. Here t=.051, $Q_{min}=-1.2(6)$, $Q_{max}=3.3(6)$, $\Delta Q=3.(5)$.

N-3

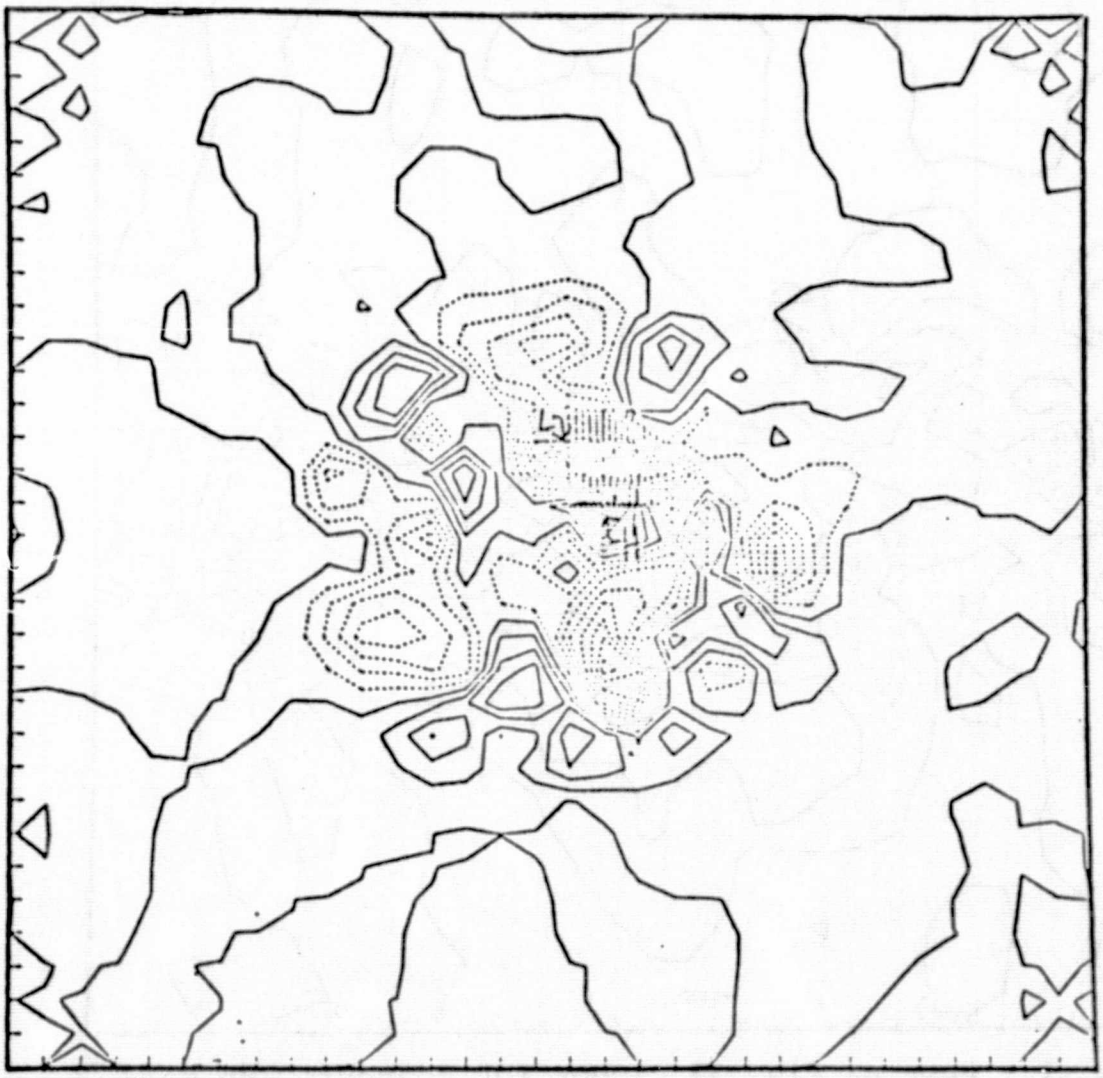

FIG. 47 - Same as Fig. 35 except the contours are made x_2 in the plane $x_1=\frac{1}{2}L$ at $\overline{X}=8$. Here $t=0$, $Q_{min}=-1.6(5)$, $Q_{max}=8.(4)$, $\Delta Q=1.(4)$.

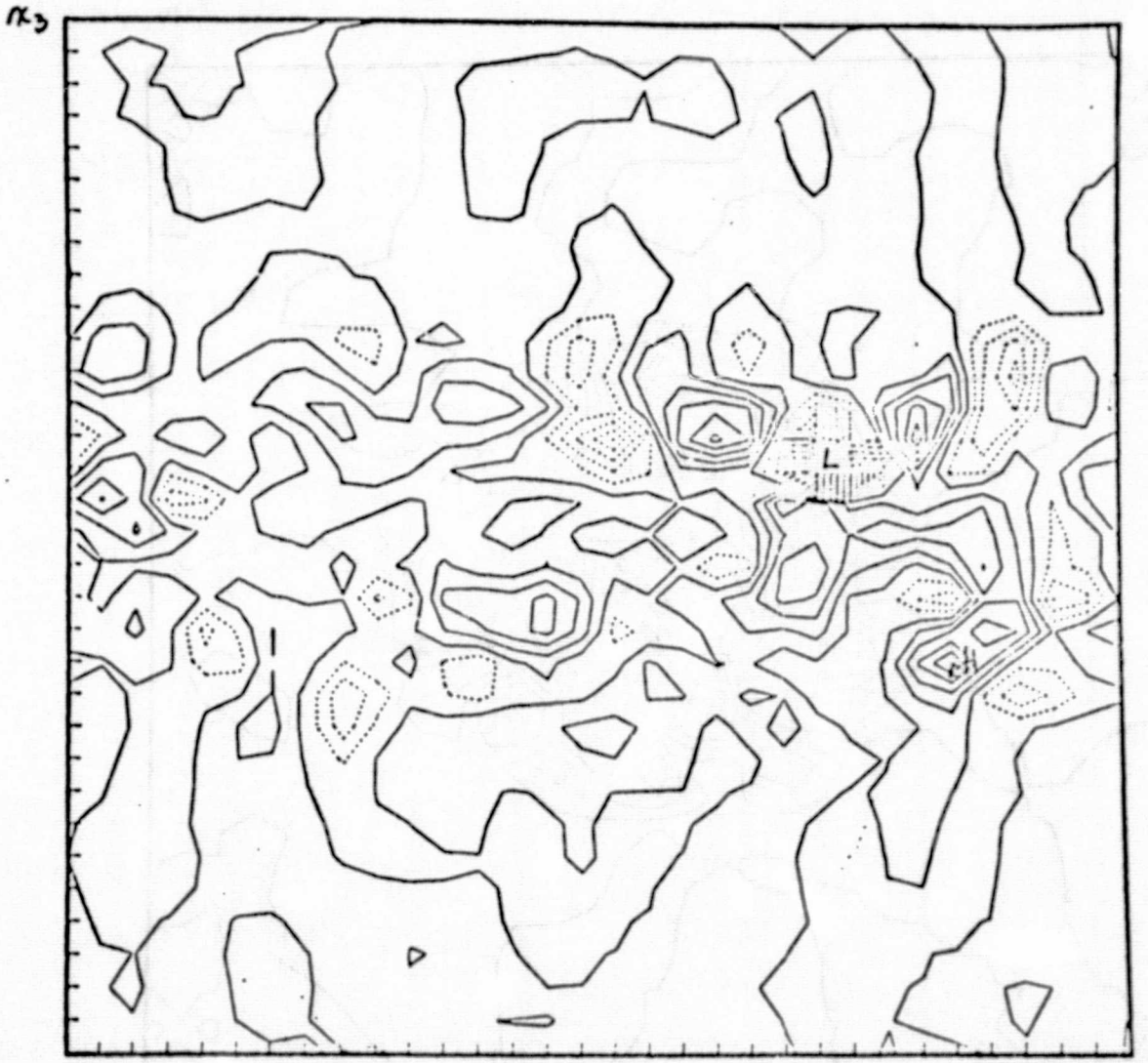

FIG. 48 - Same as Fig. 35 except the contours are made in the plane $X_2=\frac{1}{2}L$ at $\overline{X}=8$. Here t=0, $Q_{min}=-3.6(5)$, $Q_{max}=1.5(5)$, $\Delta Q=3.(4)$.

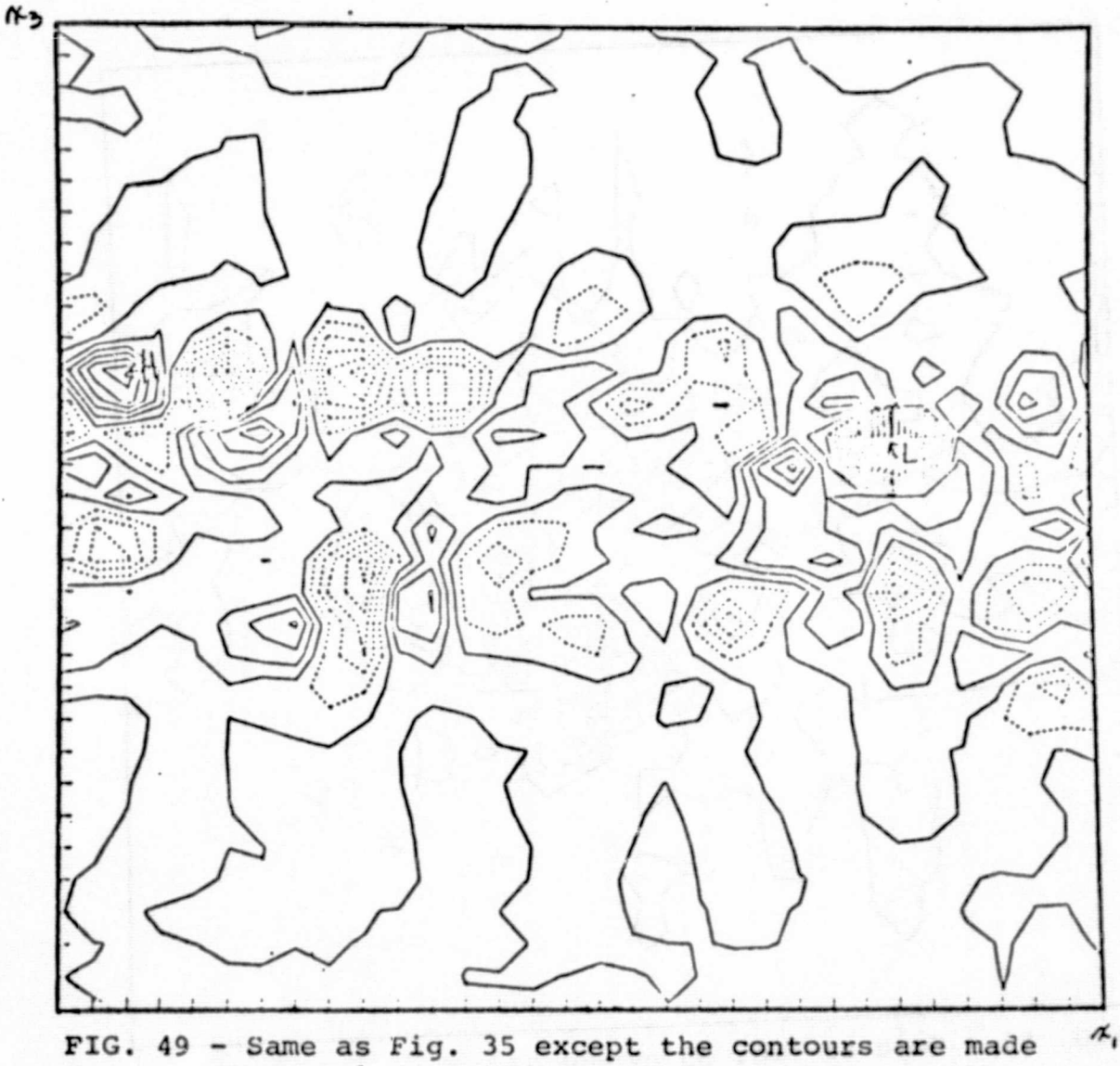

FIG. 49 - Same as Fig. 35 except the contours are made in the plane $x_3=\frac{1}{4}L$ at $\overline{X}=8$. Here t=0, $Q_{min}=-3.9(5)$, $Q_{max}=1.5(5)$, $\Delta Q=3.(4)$.

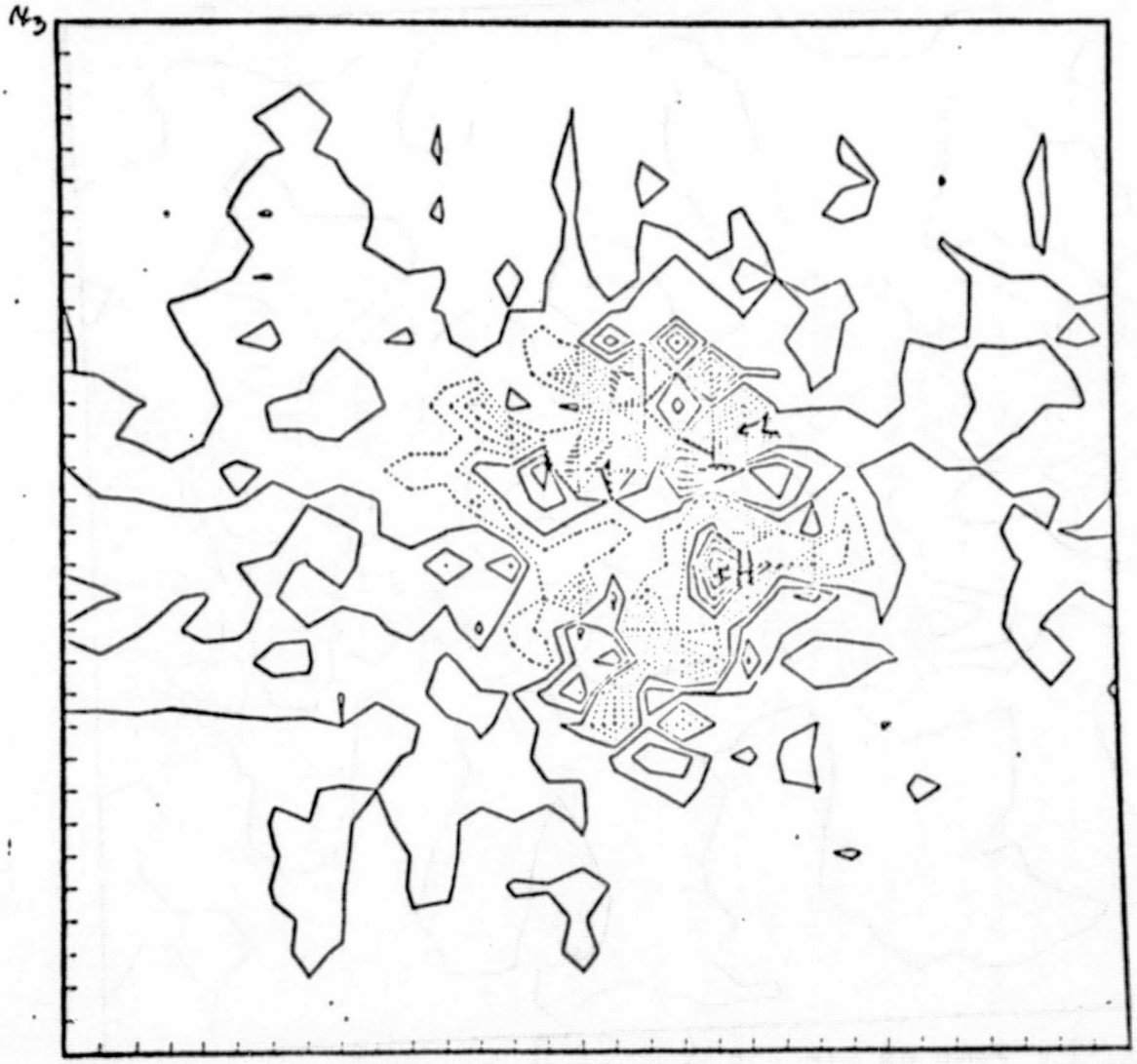

FIG. 50 - Same as Fig. 35 except the contours are made in the plane $x_1=\frac{1}{2}L$ at $\overline{X}=8$. Here t=.020, Q_{min}=-6.(5), Q_{max}=2.5(5), ΔQ=5.(4).

FIG. 51 - Same as Fig. 35 except the contours are made in the plane $x_2=\frac{1}{2}L$ at $\overline{X}=8$. Here t=.020, Q_{min}=-9.(5), Q_{max}=5.4(5), ΔQ=9.(4).

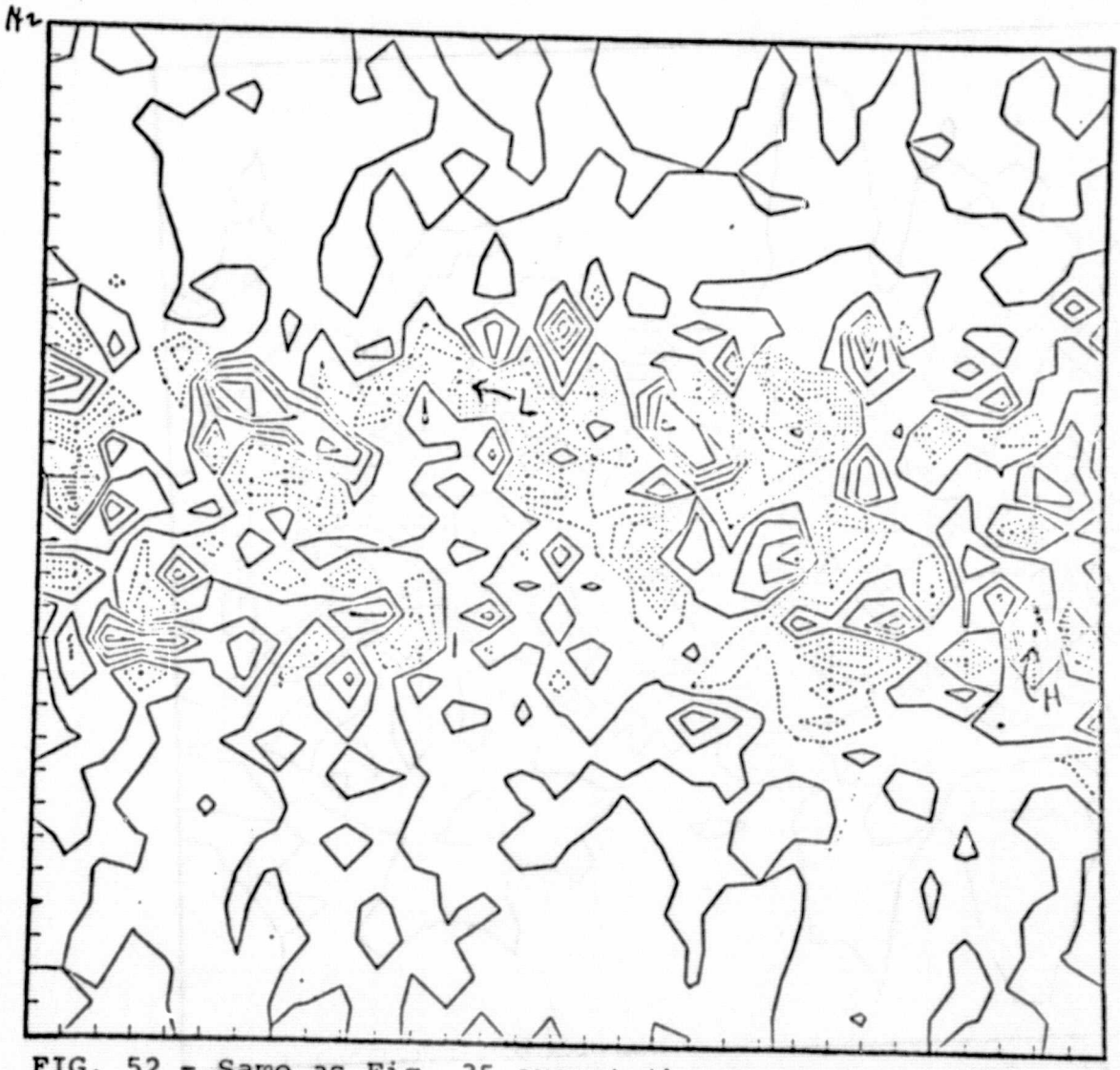

FIG. 52 - Same as Fig. 35 except the contours are made in the plane $x_3=\frac{1}{4}L$ at $\overline{X}=8$. Here t=.020, $Q_{min}=-5.6(5)$, $Q_{max}=4.9(5)$, $\Delta Q=7.(4)$.

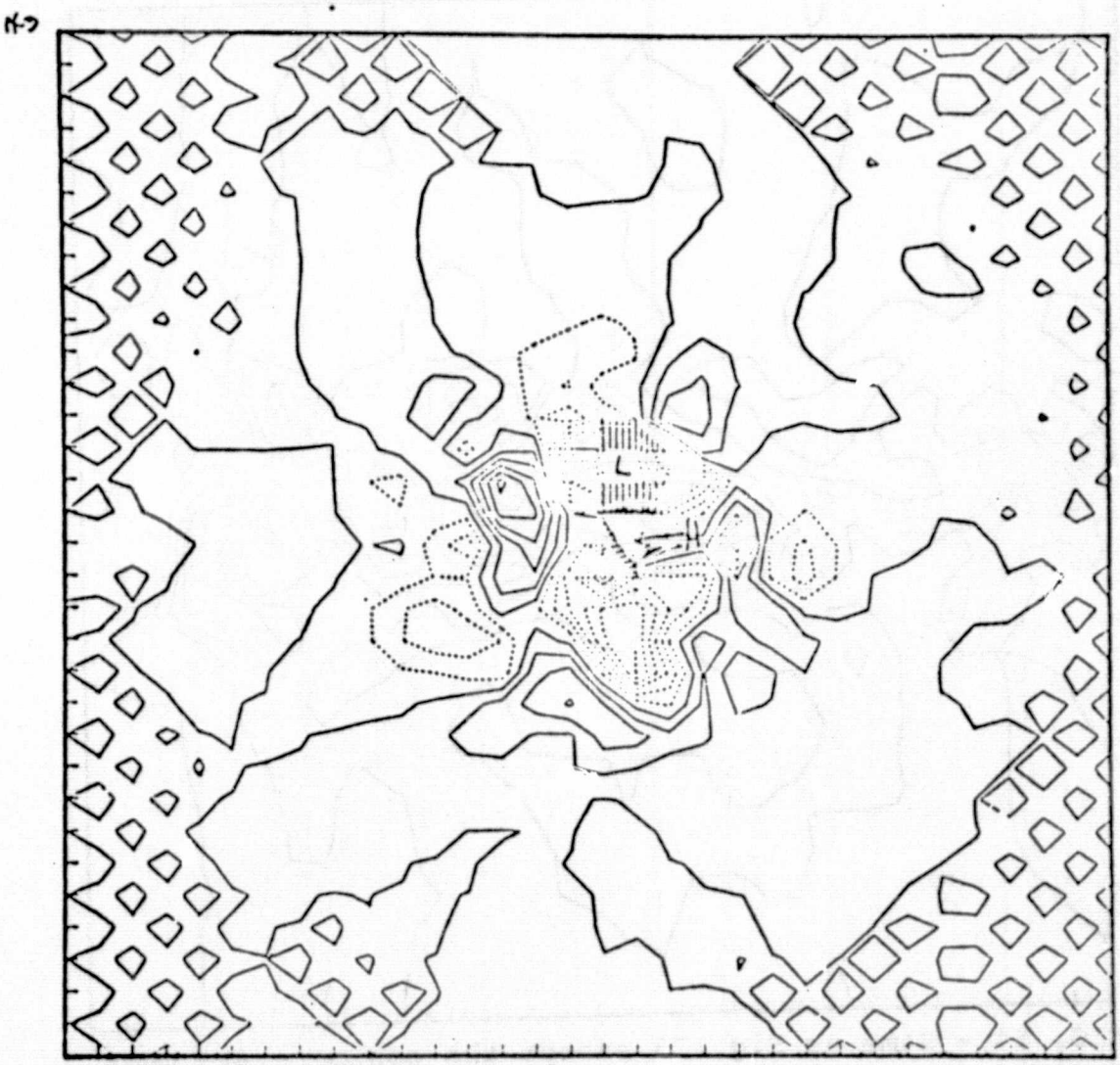

FIG. 53 - Same as Fig. 35 except the contours are made in the plane $x_1=\frac{1}{2}L$ at $\overline{X}=12$. Here $t=0$, $Q_{min}=-1.4(5)$, $Q_{max}=8.(4)$, $\Delta Q=1.(4)$.

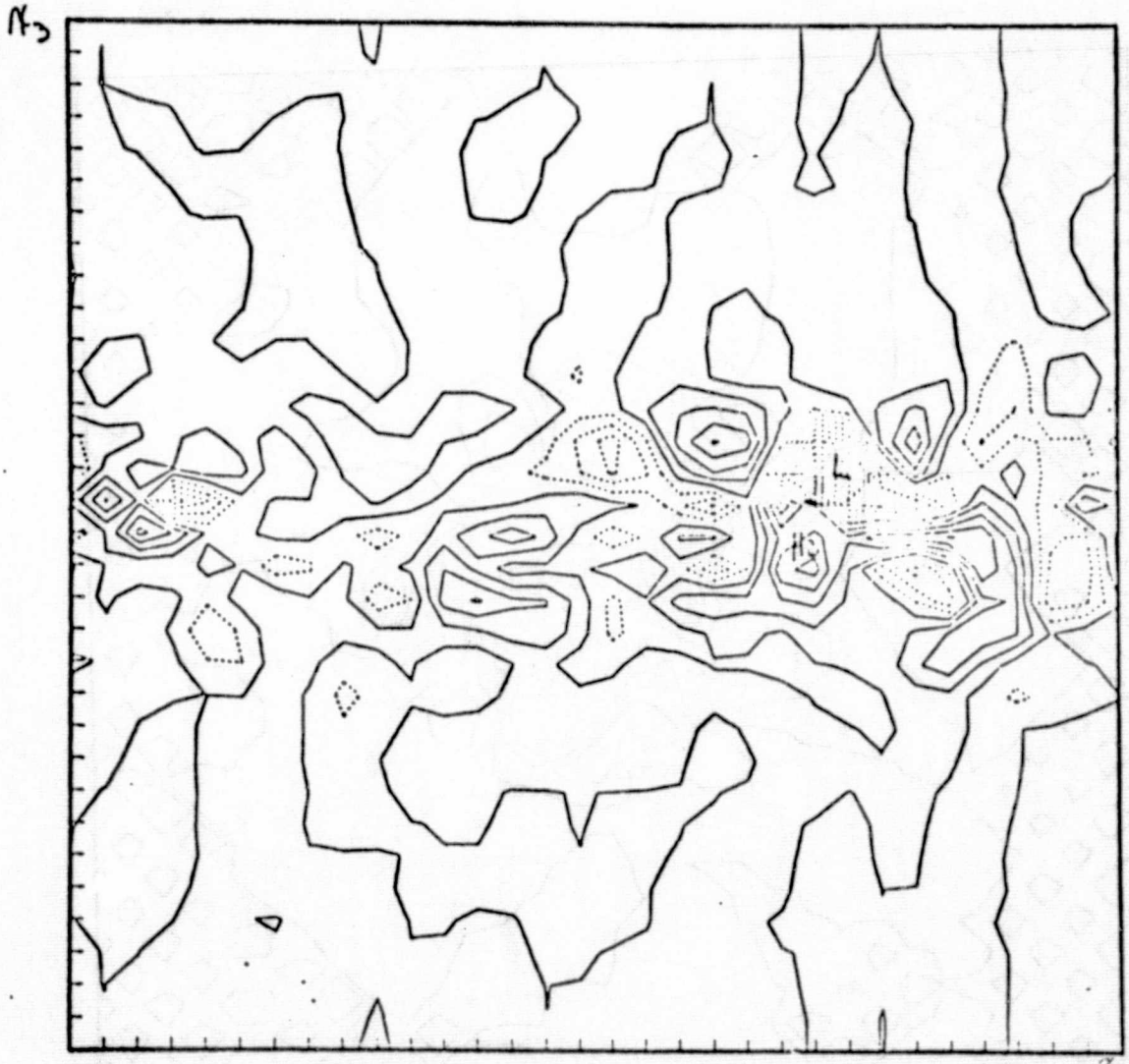

FIG. 54 - Same as Fig. 35 except the contours are made in the plane $x_2=\frac{1}{2}L$ at $\overline{X}=12$. Here t=0, $Q_{min}=-4.8(5)$, $Q_{max}=1.6(5)$, $\Delta Q=4.(4)$.

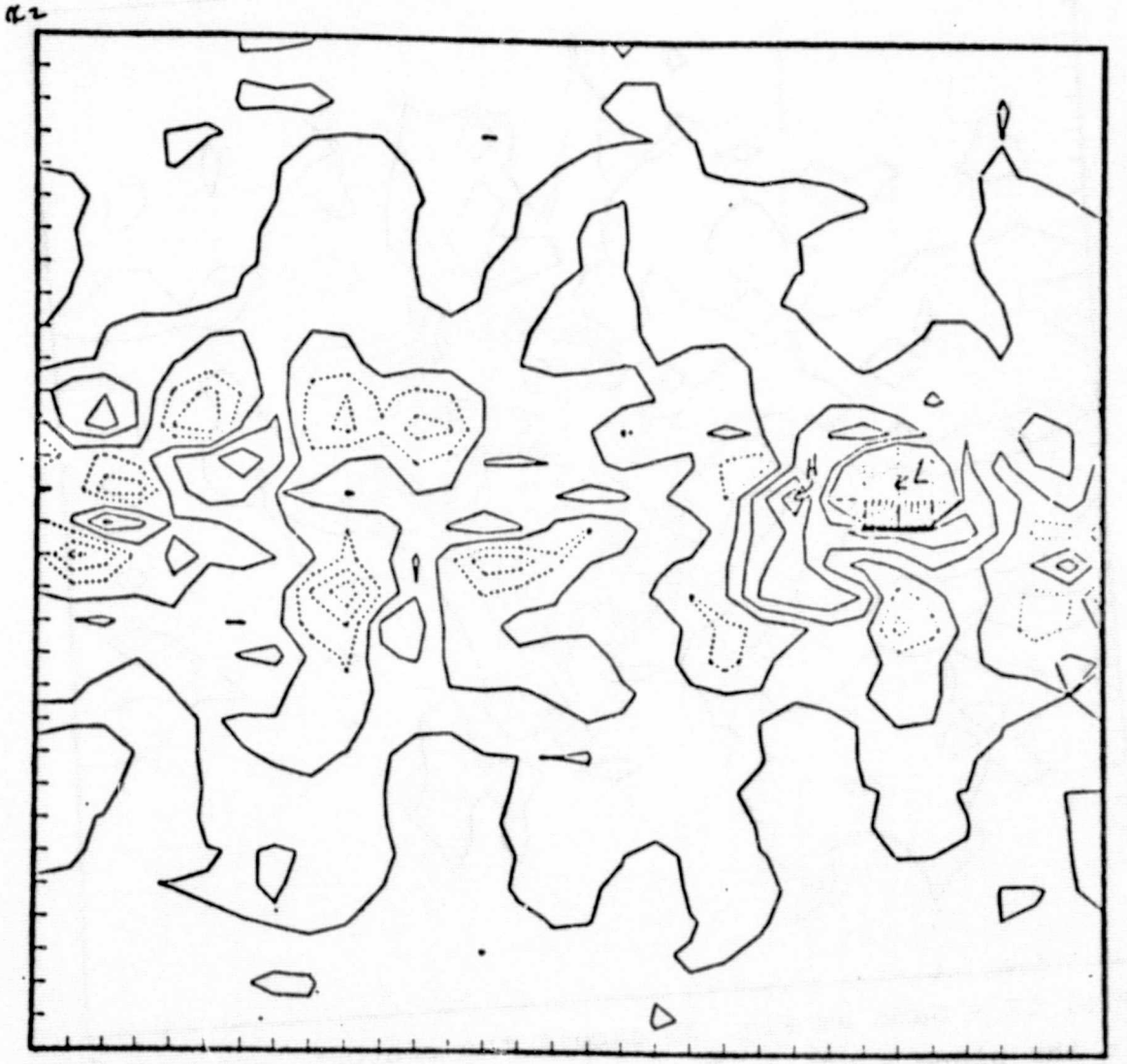

FIG. 55 - Same as Fig. 35 except the contours are made in the plane $x_3=\frac{1}{4}L$ at $\overline{X}=12$. Here $t=0$, $Q_{min}=-7.8(5)$, $Q_{max}=1.8(5)$, $\Delta Q=6.(4)$.

x_3

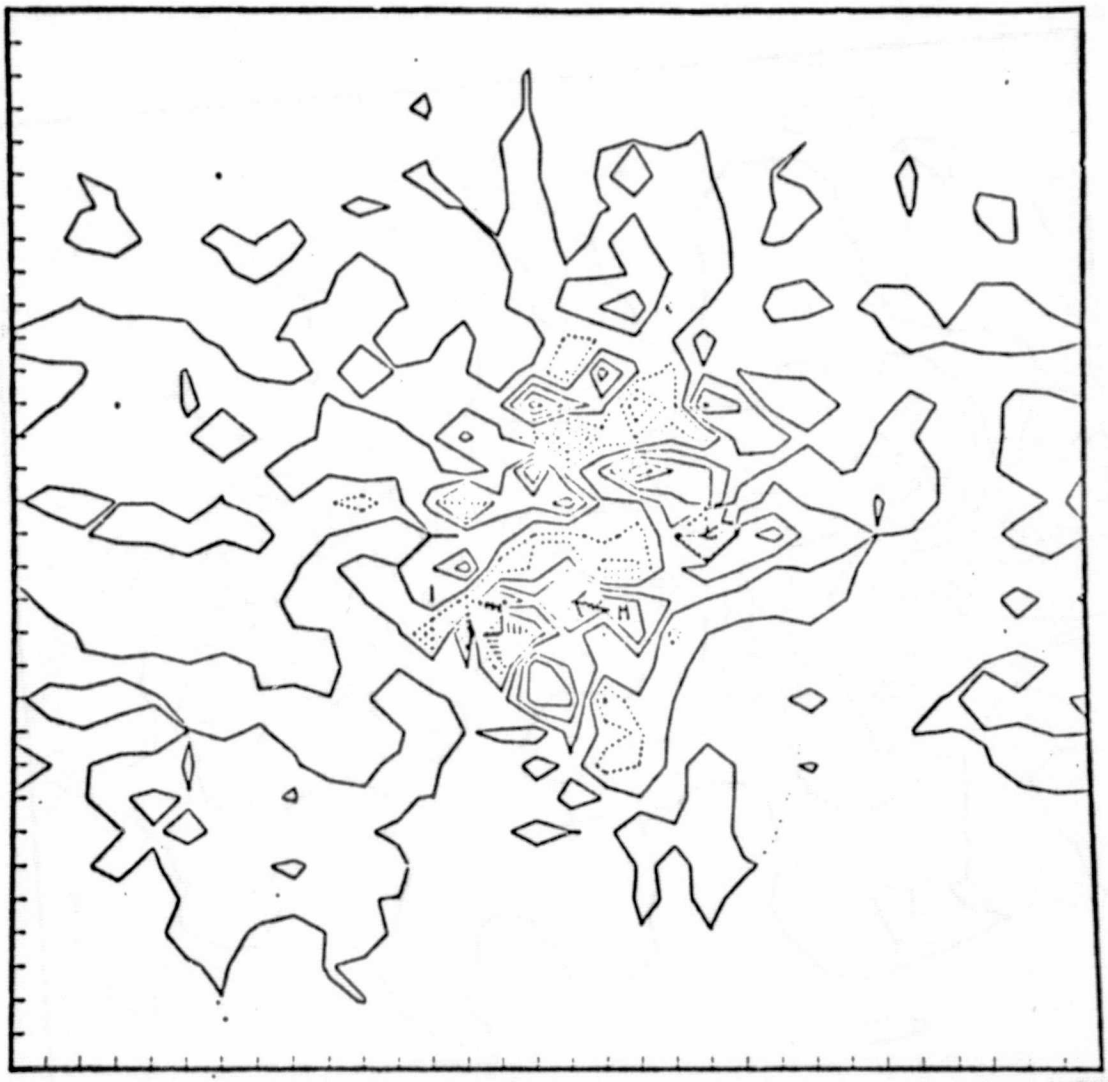

FIG. 56 - Same as Fig. 35 except the contours are made x_2 in the plane $x_1=\frac{1}{2}L$ at $\overline{X}=12$. Here $t=.032$, $Q_{min}=-5.6(5)$, $Q_{max}=4.9(5)$, $\Delta Q=7.(4)$.

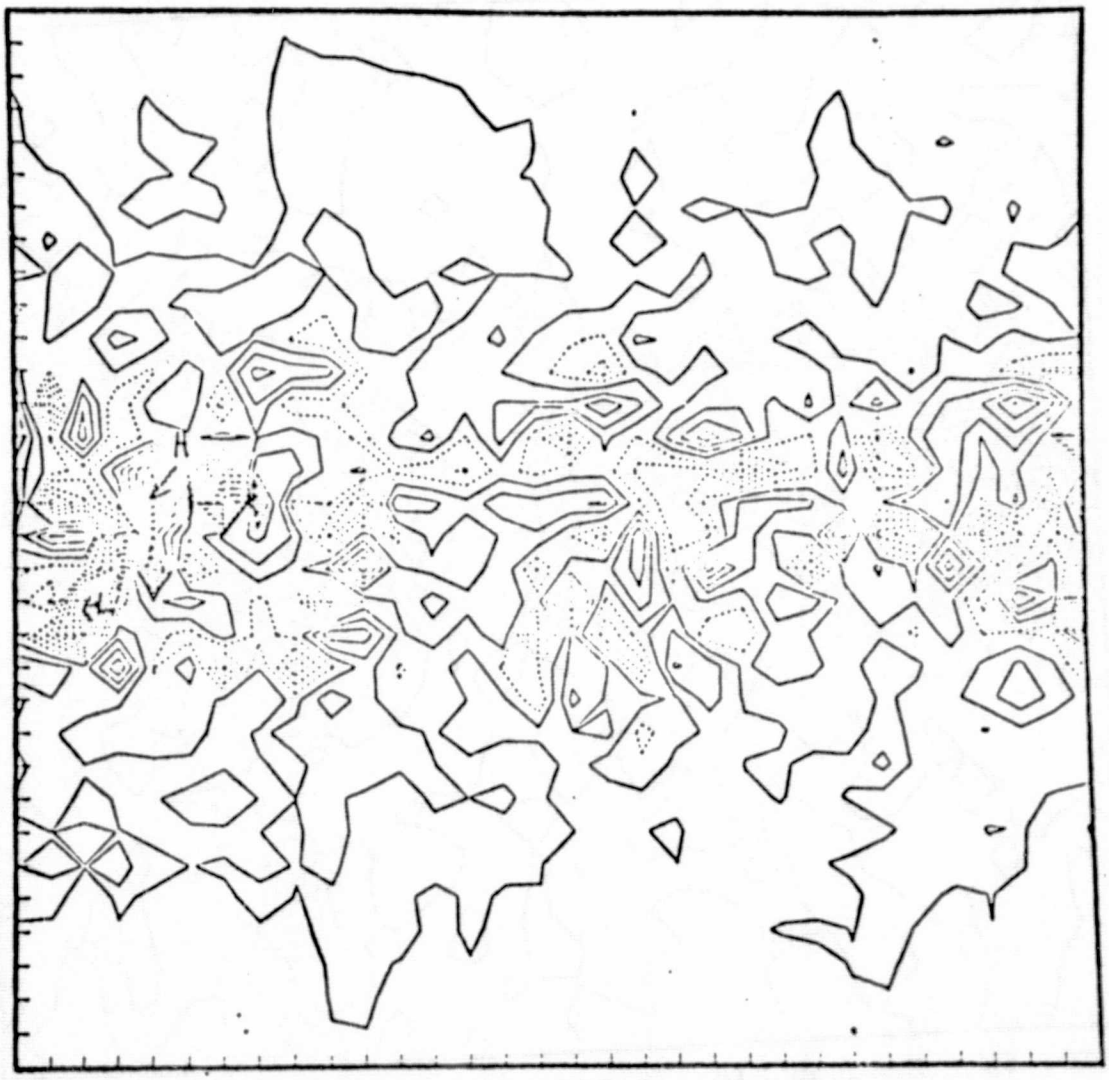

FIG. 57 - Same as Fig. 35 except the contours are made in the plane $x_2=\frac{1}{2}L$ at $\overline{X}=12$. Here $t=.032$, $Q_{min}=-1.(6)$, $Q_{max}=7.(5)$, $\Delta Q=1.(5)$.

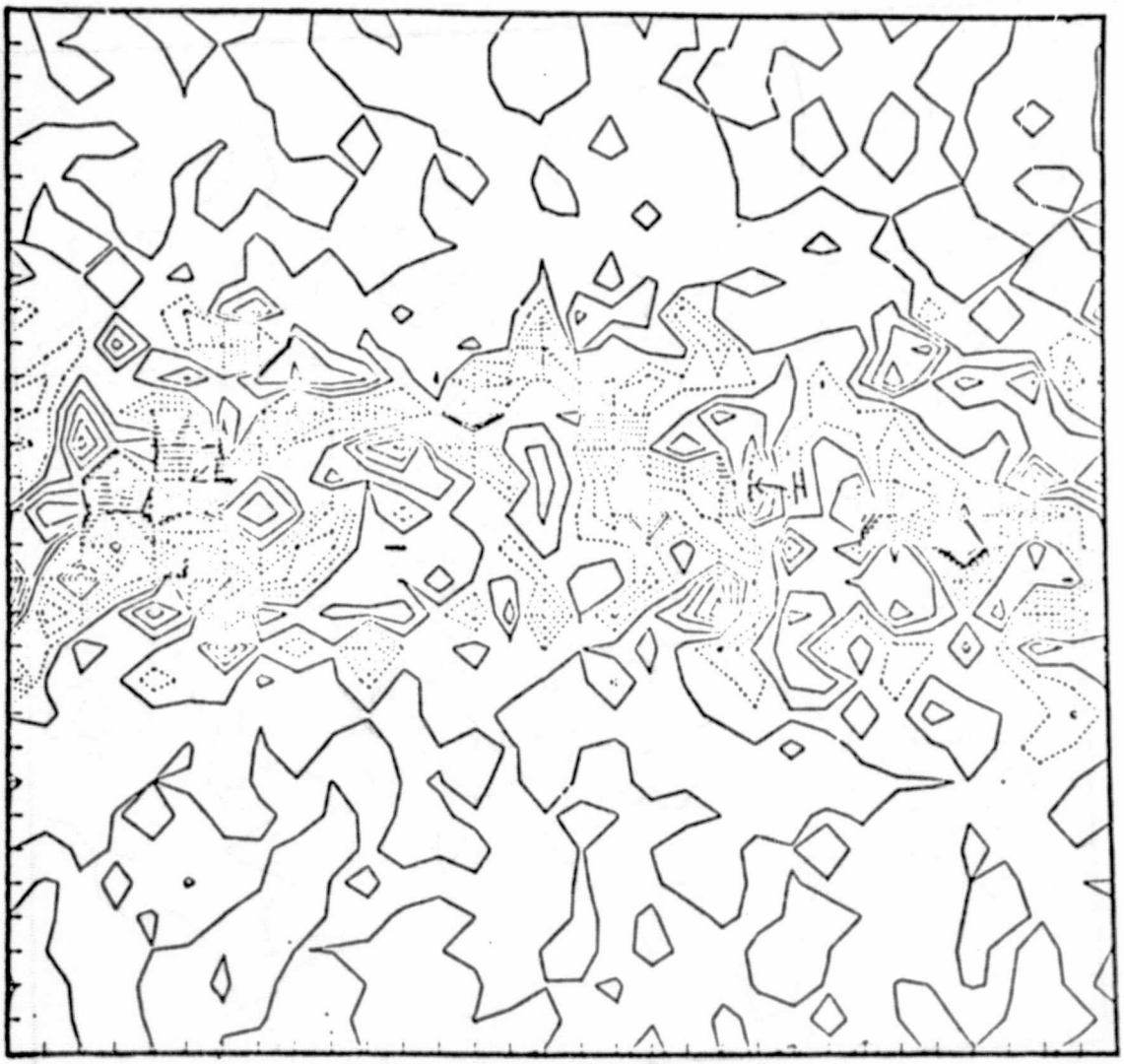

FIG. 58 - Same as Fig. 35 except the contours are made in the plane $x_3=\frac{1}{2}L$ at $\overline{X}=12$. Here t=.032, $Q_{min}=-8.(5)$, $Q_{max}=4.8(5)$, $\Delta Q=8.(4)$.